Positron Impact Ionization *of* Atoms and Molecules

A thesis submitted to University College London for the degree of Doctor of Philosophy

David Andrew Cooke

November 1, 2010

UCL, Gower Street, London, WC1E 6BT

I, David Cooke, confirm that the work presented in this thesis is my own. Where information has been derived from other sources, I confirm that this has been indicated in the thesis.

Signed: ……

To Filiz

Acknowledgements

The following people are gratefully acknowledged: my PhD supervisor, Prof. G. Laricchia, for her advice and support; Dr. D. Murtagh for assistance both scientific and otherwise; John Dumper and Rafid Jawad for their technical expertise; and my friends and family for being so tolerant.

Also of note: the rest of the positron physics group at UCL and EPSRC, for funding the whole venture.

ABSTRACT

In the present work, a beam of monoenergetic positrons has been used to investigate the ionization of atoms and small molecules at energies below 1 keV. The beam was produced from the radioactive decay of a ^{22}Na source combined with W-mesh moderators and a magnetic guidance system. The first measurements of the cross-sections for excited-state positronium formation from Xe and simultaneous ionization–excitation cross-sections for positron impact on CO_2 and N_2 have been performed.

Near-complete characterization of the detection system coupled with the ability to measure several processes simultaneously allowed the collection of data sets which were internally self-consistent. By normalizing the total ionization cross-section, an absolute scale could be applied to all measurements. A number of methods for achieving this were employed, as a check on external consistency.

The cross-section for excited-state positronium formation from Xe completed a study (Murtagh *et al.*, 2009) in Ps formation from the noble gases. The measurement has defined a trend of increasing maximal fraction of Ps formed into the $2P$ state with increasing atomic number.

The measurements of ionization–excitation for molecular targets (Cooke *et al.*, 2010a) reveal that this process is enhanced over the equivalent interaction involving electrons. This enhancement arises mainly (or exclusively, in the case of CO_2) from the effect of positronium formation, over and above the corresponding enhancement in the total ionization cross-section. Based on this observation, and the comparative lack of excited-state Ps detected in these targets, a mechanism for the enhancement involving an accidental resonance between a neutral excited molecular state and an ionic state with Ps formation has been proposed. The cross-sections for ionization–excitation were measured contemporaneously with a full suite of ionization cross-sections.

CONTENTS

LIST OF FIGURES

LIST OF TABLES

1. INTRODUCTION

1.1 *The positron*

1.1.1 *Fundamental properties*

The positron is the antimatter counterpart to the electron and as such is given the symbol e^+. It has identical mass ($m_e = 9.109 \times 10^{-31}$ kg), equal magnitude but opposite sign charge ($+1.602 \times 10^{-19}$ C) and it is a fermion (a spin-½ particle). Being a lepton, it interacts only through the electromagnetic and weak forces (and gravity). Positrons are readily produced by the radioactive decay of certain radioisotopes, though in the presence of normal (electron-containing) matter, the ultimate fate of the positron is to annihilate. In this process, a positron and electron are converted into a number of γ-rays according to the selection rule:

$$(-1)^{n_\gamma} = (-1)^{L+S} \tag{1.1}$$

where S is the spin of, and L the orbital angular momentum of, the pair. Hence, for free positron–electron annihilation, two γ-ray decay is most likely as the cross-section for annihilation is proportional to α^{n_γ}, where α is the fine structure constant ($\sim 1/137$) and n_γ is the number of photons. Figure 1.1 shows the Feynman diagrams for positron–electron annihilation resulting in the production of up to three γ-rays. Note that for single quantum and radiationless decay, the presence of a third body is required to conserve both energy and momentum (in the latter case, the third body being another atomic electron). This requirement for the involvement of an additional particle greatly reduces the probability of single quantum- and radiationless decay, typically by a factor of $\lambda_c{}^3\rho$, where ρ is the local particle density and λ_c the Compton wavelength (as a measure of the physical extent of the additional body). This term is approximately of the order of α^3. Decay into more than two γ-rays is also suppressed with respect to two γ-ray decay—the probability of three-γ-

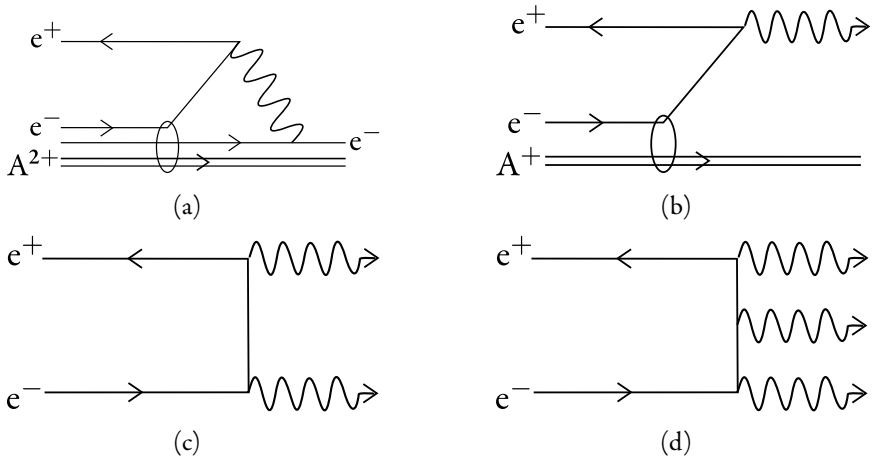

Fig. 1.1: Feynman diagrams for positron–electron annihilation producing 0–3 photons. Note that for less than two photons to be observed, the presence of additional bodies is required.

ray decay is a factor of approximately 1/378 (Ore & Powell, 1949) smaller than for two-γ-ray decay; that for four-γ-ray decay, a factor of 1.5×10^{-6} (Adachi *et al.*, 1994).

1.1.2 Interaction with matter

In general, the behaviour of positrons in normal matter is not simply confined to such 'direct' annihilation events. The positron may undergo any number of scattering events which are summarized in the following reactions (1.2–1.10). Two scattering processes may occur at any energy, namely annihilation itself and elastic scattering.

$$\mathrm{e}^+ + \mathrm{A} \rightarrow \mathrm{A}^+ + n\gamma \tag{1.2}$$

$$\mathrm{e}^+ + \mathrm{A} \rightarrow \mathrm{A} + \mathrm{e}^+ \tag{1.3}$$

Once the positron possesses sufficient energy, other processes become feasible:

$$e^+ + A \rightarrow A^* + e^+ \tag{1.4}$$

$$e^+ + A \rightarrow A^+ + Ps \tag{1.5}$$

$$e^+ + A \rightarrow A^+ + e^+ + e^- \tag{1.6}$$

$$e^+ + A \rightarrow A^{+*} + Ps \tag{1.7}$$

$$e^+ + A \rightarrow A^{+*} + e^+ + e^- \tag{1.8}$$

$$e^+ + A \rightarrow A^{n+} + Ps + (n-1)e^- \tag{1.9}$$

$$e^+ + A \rightarrow A^{n+} + e^+ + ne^- \tag{1.10}$$

where, in reactions 1.9 and 1.10, $1 < n < Z$. These are excitation and ionization processes and are listed in approximately ascending threshold energy order. The symbol Ps refers to the bound state between a positron and an electron known as *positronium*. Other points of terminology which it is convenient to introduce here are the descriptive labels given to the other scattering processes. Generally, the result of reaction 1.6 is referred to as *direct ionization* and may be *single* (as with reaction 1.6) or *multiple* (as with reaction 1.10). Positronium formation (reaction 1.5), when accompanied by the release of additional electrons, is referred to as *transfer ionization* (reaction 1.9). Ionization processes accompanied by target excitation (reactions 1.7 and 1.8) are simply *ionization–excitation* processes, which may be further subdivided into resulting from direct ionization or positronium formation.

Positronium

Prior to mutual annihilation, a positron and electron may form a short-lived bound state. The result, positronium, has a ground state binding energy of 6.8 eV and can exist in two spin states, arising from the possible orientations of the spins of its constituent particles. These may be parallel, leading to the triplet state (ortho-Ps), or antiparallel, leading to the singlet state (para-Ps). The triplet ground state ($^3S_1$) has a lifetime of 142 ns whereas the corresponding singlet state ($^1S_0$) has a lifetime of just 125 ps. The subsequent decay of ground-state Ps proceeds by an odd number of γ-rays for o-Ps or an even number for p-Ps in order to conserve angular momentum. Thus, a unique signal of o-Ps is the coincident detection of three γ-ray photons whose energies must total the sum of twice the rest mass energy of the electron (1.022 MeV) and any kinetic energy possessed by either initial particle. As with 'direct' annihilation decay via higher numbers of photons is considerably less

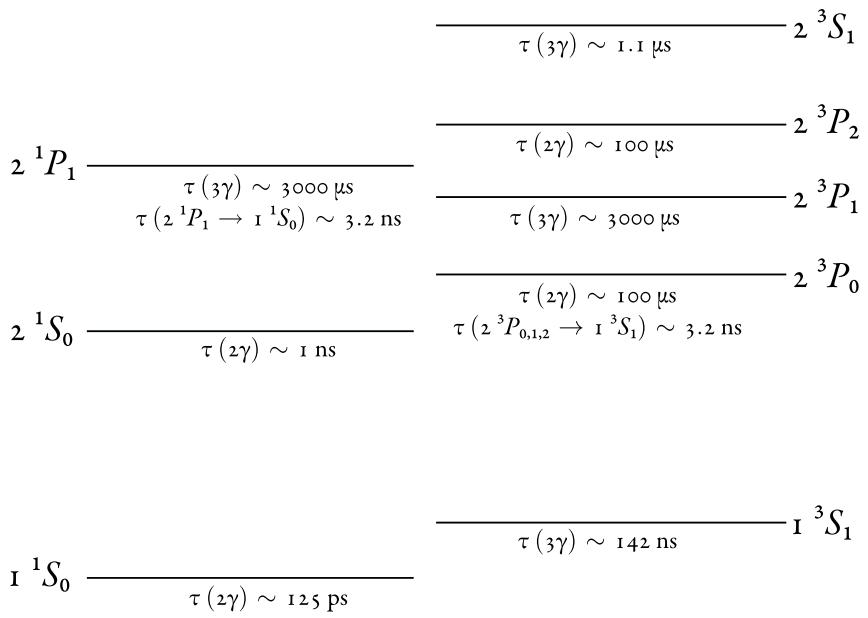

Fig. 1.2: Energy level diagram of Ps showing hyperfine structure of the $n = 1$ and $n = 2$ states. Lifetimes against annihilation and de-excitation are also shown. Diagram adapted from Rich (1981).

probable.

At the coarsest level of description, Ps is structurally similar to atomic hydrogen, with the Bohr energy levels halved as a result of the lower mass of the positron by comparison to the proton. Beyond this similarity, the fine structure is quite different, structure up to $n = 2$ being shown in Figure 1.2 (Rich, 1981). The difference arises from the greater magnetic moment of the positron compared to the proton (larger by a factor of ~ 658), which elevates the hyperfine structure observed in positronium to the order of the fine structure observed in hydrogen (Benedetti & Corben, 1954).

Ionization

As described by equations 1.5–1.10, in addition to the formation of positronium, the positron may ionize a target directly by releasing one (or more) electron(s). Overall, the total ionization cross-section of a target (Q_i^t) is defined by:

$$Q_i^t = Q_i^+ + Q_{\mathrm{Ps}} + Q_{ti} + Q_{\mathrm{ann}} + Q_i^{n+} \tag{1.11}$$

where Q_i^+ represents the cross-section for single direct ionization, Q_{Ps} that for positronium formation, Q_{ti} transfer ionization, Q_{ann} 'direct' annihilation, and Q_i^{n+} multiple direct ionization.* For atomic targets, this is usually abbreviated to

$$Q_i^t = Q_{\mathrm{Ps}} + Q_i^+ + \sum \mathrm{HO} \tag{1.12}$$

or, indeed,

$$Q_i^t \approx Q_{\mathrm{Ps}} + Q_i^+ \tag{1.13}$$

where the cross-sections for the higher-order (HO) processes are usually small enough, relative to Q_i^+ and Q_{Ps}, to be considered negligible (Van Reeth *et al.*, 2005).

1.1.3 *Applications*

The study of the systems described by reactions 1.2–1.10, both in terms of the behaviour of the positron and/or the target, forms part of the wider discipline of atomic physics. By varying the probe particle (i.e. using positrons, electrons, photons, protons, antiprotons or heavier ions), it is possible to discover fundamental properties of either the target or the probe particle itself. However, in the years following the prediction (Dirac, 1930) and subsequent discovery of the positron (Anderson, 1933, see Figure 1.3 and below), the field of positron physics has grown to encompass such diverse disciplines as biology, materials science and astrophysics.

The mutual annihilation of a positron and electron producing γ-rays has allowed the development of positron emission tomography, a functional imaging technique used in medicine whereby γ-rays from a positron emitter attached to a biologically active molecule are used to image processes occurring in the body (Wrenn *et al.*, 1951; Phelps *et al.*, 1975). A typical molecule used is fluorodeoxyglucose, which is structurally identical to D-glucose except with a hydroxyl group substituted by a fluorine atom. Using the radioisotope ^{18}F (a β^+ emitter) as the fluorine group, this molecule can be used to identify areas of abnormally high metabolic activity (for example, tumours).

The same positron annihilation signal has been used by astronomers studying the galactic spectrum. It has been observed that the majority of γ-rays originating from the galactic

* Note: ionization–excitation events need not be explicitly included as they are a subset of the above-identified ionization events.

centre are attributable to electron–positron annihilation, approximately 90% of which arise from *positronium* (Ps) (Harris *et al.*, 1990).

Positrons are used as a probe particle in materials science. The field of positron annihilation spectroscopy examines three properties of the γ-rays arising from positron annihilation in solids, namely: the time from positron emission to their annihilation, the deviation of their energies from 511 keV and the deviation from 180° (for two-γ-ray annihilation) of the angle between them. The lifetime provides evidence of defects in the material, as the electron density in such defects may be lower than in the bulk of the material, and positrons may be trapped at such sites. The other two properties contain information about the electronic structure at the site of annihilation. As the positron will have rapidly thermalized in the material, any additional energy (above the rest mass energy of the two particles) and momentum (detectable via the γ-ray spectrum and emission angle) comes almost entirely from the electron (Siegel, 1980).

This thesis is principally concerned with examining positron–atom and molecule collisions and so the remainder of this chapter will be mainly focussed on the relevant developments of the field up to the present, beginning with a brief historical note.

1.2 A brief history of positron/positronium physics

1.2.1 Discovery

The existence of a positively charged equivalent particle to an electron arose from the combination of special relativity and quantum mechanics in the Dirac equation (Dirac, 1930). A reformulation of the Schrödinger equation incorporating the relativistic relationship between energy, momentum and mass, the Dirac equation produced the surprising result of additional *negative* energy solutions for a free electron. This led to the interpretation that the vacuum comprised an infinite set of negative energy electron states which, if totally filled, by the Pauli Exclusion Principle, prevents the electrons in positive energy states falling into states below zero energy by emission of photons. This filled infinite set became known as the 'Dirac sea'. This description predicted that a photon of sufficient energy could promote an electron from a negative energy state to a positive one, leaving behind an empty negative energy state, or holes, in the Dirac sea. These should behave as positively charged particles, an observation that led Dirac to predict the existence of such particles. Dirac himself initially appeared to lack the confidence to predict the existence of a new

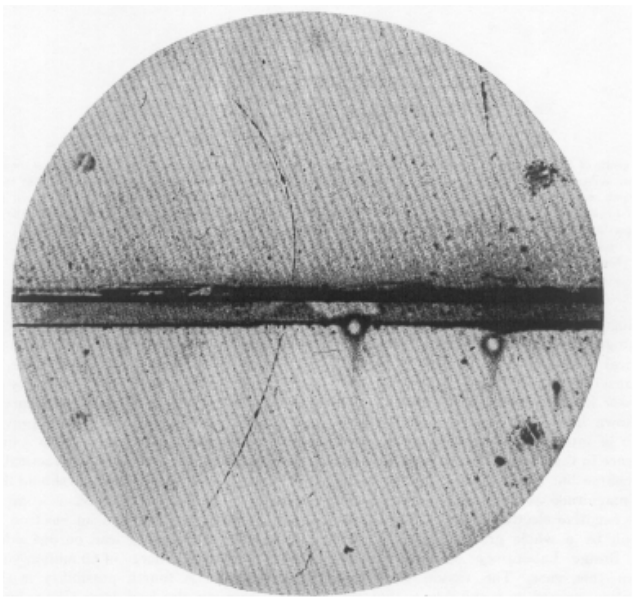

Fig. 1.3: Picture of the first detected positron cloud-chamber track. The particle enters at the bottom, loses energy in the 6 mm lead plate across the middle, and then proceeds along a curved path in a magnetic field. The energy loss and path curvature allow the mass and charge of the particle to be estimated (Anderson, 1933).

particle, and so originally suggested that these holes might correspond to protons, despite the constraint that his equation had on the mass of such a particle. Yet in 1933 this particle was actually observed in the tracks of cosmic rays using a cloud chamber (Anderson, 1933). For this reason, Dirac's prediction is considered one of the great achievements of 20$^{\text{th}}$ century theoretical physics.

The promotion of an electron in a negative energy state to a positive one—effectively creating both an electron and a positron—is the process known as *pair production*, and was subsequently observed by Blackett & Occhialini (1933), providing further confirmation for Dirac's theory. The converse process, mutual annihilation of an electron and positron, was also experimentally confirmed to occur by Blackett & Occhialini (1933).

1.2.2 Bound states

The possibility that, prior to mutual annihilation, an electron and positron could form a bound state was first mooted by Mohorovičić (1934). The existence of positronium (see Section 1.1.2) was experimentally confirmed by Deutsch (1951) by studying positron annihilation rates in gases. Larger bound states, such as Ps^-, Ps_2 etc. were predicted to exist

as well (Wheeler, 1946), being described as 'polyelectrons' or 'polyleptons'. Experimental evidence for such states was less forthcoming than for positronium: the negative ion Ps^- was observed (Mills, 1981) by bombardment of thin carbon films by positrons and the molecule dipositronium (Ps_2) recently observed (Cassidy & Mills, 2007) in porous silicon.

Experimental evidence for bound states comprising positrons and atoms (or molecules) is considerably thinner on the ground. Some exists for PsH, with a binding energy of 1.1 ± 0.2 eV, based on a study of positron collisions with CH_4 (Schrader *et al.*, 1992). The unique signal used to identify PsH was the formation of CH_3^+ ions below the direct threshold for their formation. This measurement followed several calculations of the binding energy, beginning in 1951 with the demonstration that the system was bound (Ore, 1951). A number of bound states between positrons and more complex atoms have been theoretically identified (see Mitroy *et al.*, 2002, and references therein), and a number conclusively proven impossible, e.g. e^+H and e^+He (Armour, 1982).

1.2.3 Moderation

For the field of *low-energy* positron physics, one of the most important achievements was the development of the moderator, which allowed the high energy β^+ emissions from radioisotopes such as ^{22}Na, ^{58}Co and ^{64}Cu, to be slowed to the eV energy range. As an alternative to the use of radioisotopes, positrons may be created using high-energy photons (such as those created by bremsstrahlung in a linac or synchrotron) and pair production (see e.g. Ley, 1997). Both these methods, however, lead to the production of positrons possessing energies of order 0.1–1 MeV, and isotropic distributions. Hence, for atomic scattering investigations these positrons require moderation. The work of Canter *et al.* (1972), in producing a MgO moderator with an efficiency of approximately 3×10^{-5}, is therefore considered a significant milestone in the field.[†] The process of moderation relies on the near-thermalization of positrons in the bulk of a material, followed by their ejection from the surface. The mechanism behind moderation is pictorially described in Figure 1.4. The ejection is either the result of the material having a negative work function for positrons (as in the case of tungsten), or the positrons being unable to thermalize completely and leaving the surface with epithermal energies (as with solid rare gases).

[†] It followed the observation of slow positrons from a Cr surface irradiated using a ^{64}Cu source (Cherry, 1958).

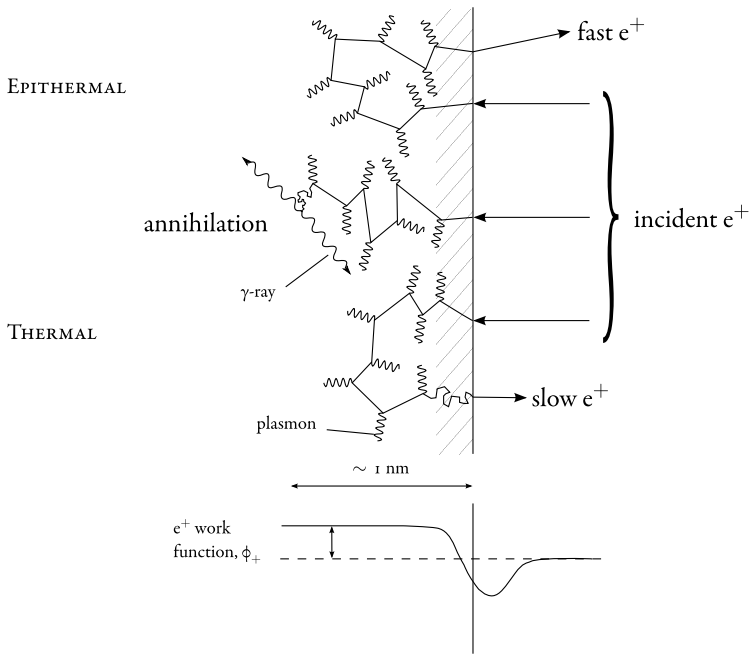

Fig. 1.4: Three outcomes of a positron impinging on a surface. Top to bottom: fast positrons emerging before thermalization; positrons annihilating in the bulk; and positrons being ejected after they have achieved thermal velocities. Note that the local potential minimum at the surface can result in moderated positrons being trapped. Figure adapted from (Charlton & Humberston, 2001).

The remainder of this chapter will be focused on positron-impact ionization of targets in the gas phase. By the mid-1980s, several groups had constructed positron beamlines using combined positron sources (either radioactivity-derived or accelerator-derived) and moderators to study such processes and experiments had begun on solid rare gas moderators, the solid Ne moderator first produced by Mills &Gullikson (1986) being the most efficient yet discovered. By this time, measurements of total and various other ionization and excitation cross-sections had been reported for several target gases.

In addition to experimental determinations, there was a simultaneous drive to theoretically describe positron interactions with matter. Ionization by positron impact provides a more challenging scenario to model by comparison to electron impact, mainly as a result of the capture process, but also (to a lesser degree) because of annihilation. Atomic hydrogen and helium have been well studied and are now described with a good level of agreement by both theory and experiment.

A review of ionization cross-sections, including, but not limited to Ps formation, is presented in Sections 1.3–1.4, together with a discussion about the various experimental techniques employed to measure such cross-sections. Where available, theoretical results are presented along with the measurements discussed in the following sections.

1.3 Ionization of atoms

The atomic targets examined in this section are three noble gases: He, Ar and Xe. They have been chosen both to demonstrate some of the salient features of positron–atom collision cross-sections and to allow the introduction of some experimental and theoretical techniques employed for determining such cross-sections. Figures 1.5–1.9 show a summary of existing experimental and theoretical determinations of e^+ impact cross-sections for He and the noble gases. The following discussion will compare experimental results both to each other and to theoretical calculations and focus on the various experimental techniques employed. A comprehensive review of these cross-sections can be found in Laricchia *et al.* (2008).

1.3.1 He

There are a number of independent experimental results for this target, owing to the simplicity of the atom and its availability directly from a gas bottle (unlike H). Figures 1.5–1.8 shows experimental determinations of Q_i^t, Q_i^+ and Q_{Ps} for this target. For Q_i^t, good agree-

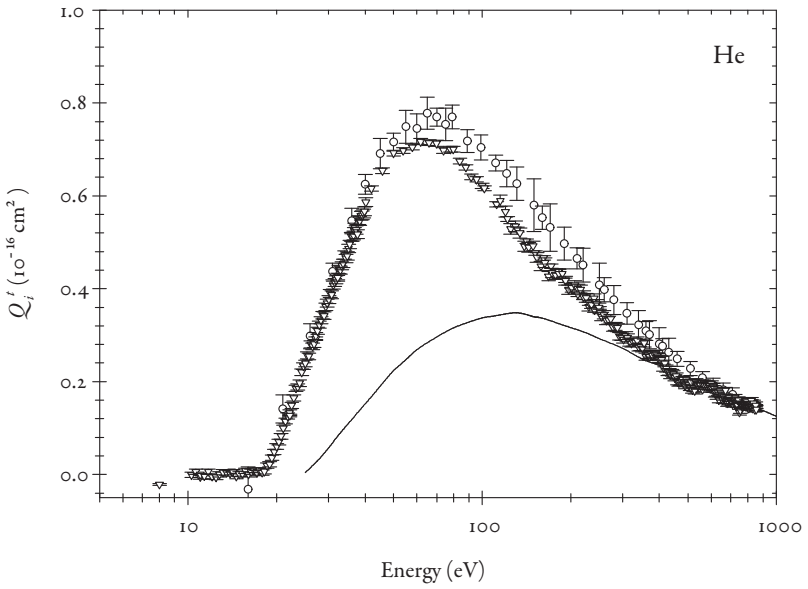

Fig. 1.5: Experimental determinations of Q_i^t for He. ▿—(Murtagh *et al.*, 2005), ○—(Fromme *et al.*, 1986), solid line—electron data of Rejoub *et al.* (2002).

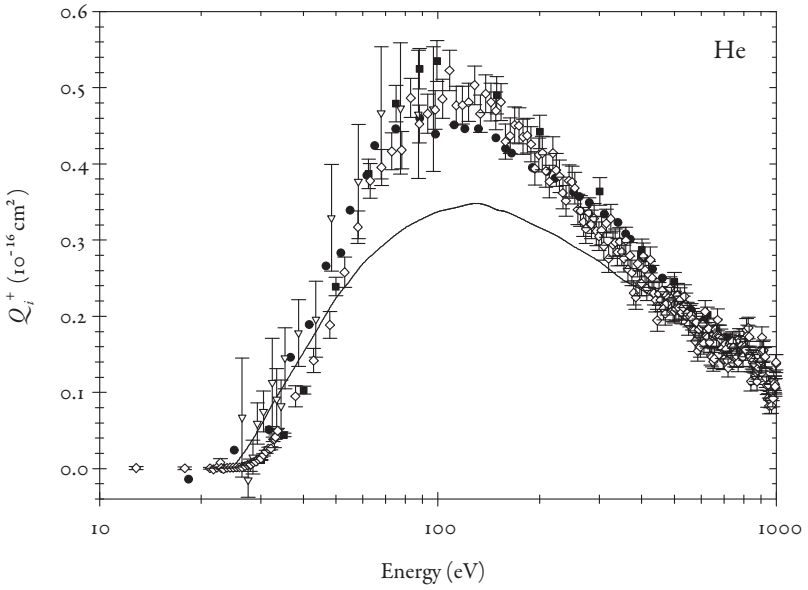

Fig. 1.6: Experimental determinations of Q_i^+ for He. ◇—(Moxom *et al.*, 1996), ■—(Jacobsen *et al.*, 1995), ▿—(Mori &Sueoka, 1994), ●—(Fromme *et al.*, 1986), solid line—electron data of Rejoub *et al.* (2002).

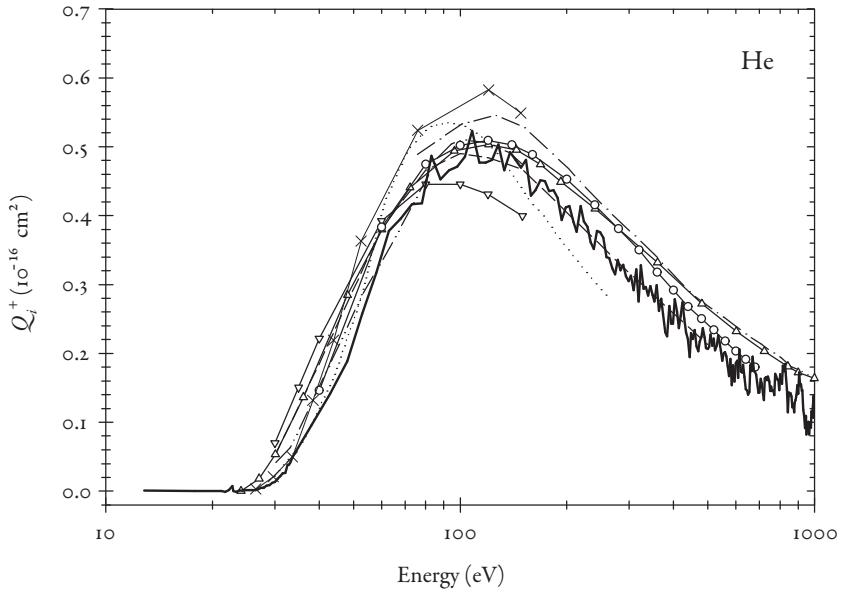

Fig. 1.7: Calculations of Q_i^+ for He. Solid line with ×—(Utamuratov *et al.*, 2010), solid line with ▵—(Moores, 2001), double chain curve—(Campbell *et al.*, 1998), dashed curve—(Campeanu *et al.*, 1996), chain curve—(Chen &Msezane, 1994), solid line with ○—(Ratnavelu, 1991), dotted curve—(Schultz &Olson, 1988), solid line with ▿—(Basu *et al.*, 1985), thick solid line—experimental results of Murtagh *et al.* (2005).

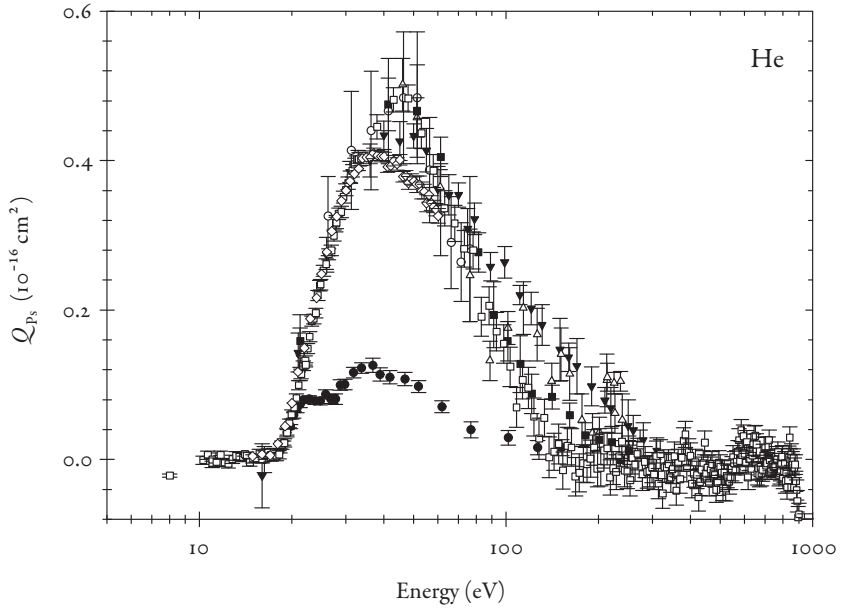

Fig. 1.8: Experimental determinations of Q_{Ps} for He. ◇—(Caradonna *et al.*, 2009), ▫—(Murtagh *et al.*, 2005), ▪—(Overton *et al.*, 1993), ▵—(Diana *et al.*, 1986), ▾—(Fromme *et al.*, 1986), ○—(Fornari *et al.*, 1983), ●—(Charlton *et al.*, 1983).

ment exists between the two experimental determinations—Murtagh *et al.* (2005) and Fromme *et al.* (1986). These groups also measured Q_{Ps}, both based on the assumption that equation 1.13 holds true, that is, that the higher-order ionization processes are negligible. Murtagh *et al.* (2005) used the measurement of Q_i^+ of Moxom *et al.* (1996) in combination with Q_i^t to determine Q_{Ps}, whereas Fromme *et al.* (1986) measured both Q_i^t and Q_i^+ to the same end. However, these determinations essentially used the same technique to determine the cross-sections: collection of the ions produced (in combination with coincidence measurements between a positron and an ion). Note that this technique requires that the ions are detected with a known (ideally, energy independent) efficiency. This may not be achieved if the ions are produced with significant kinetic energy.[‡]

In addition to these two groups, several others have reported measurements of Q_i^+ and Q_{Ps} and presently good accord among most determinations exists, with the possible exception of the very recent measurement of Caradonna *et al.* (2009), which disagrees on the position (and magnitude) of the peak. The earliest such measurements (Charlton *et al.*

[‡] This is more of a problem for ionization of molecules, where dissociation events can produce daughter ions with several eV of kinetic energy.

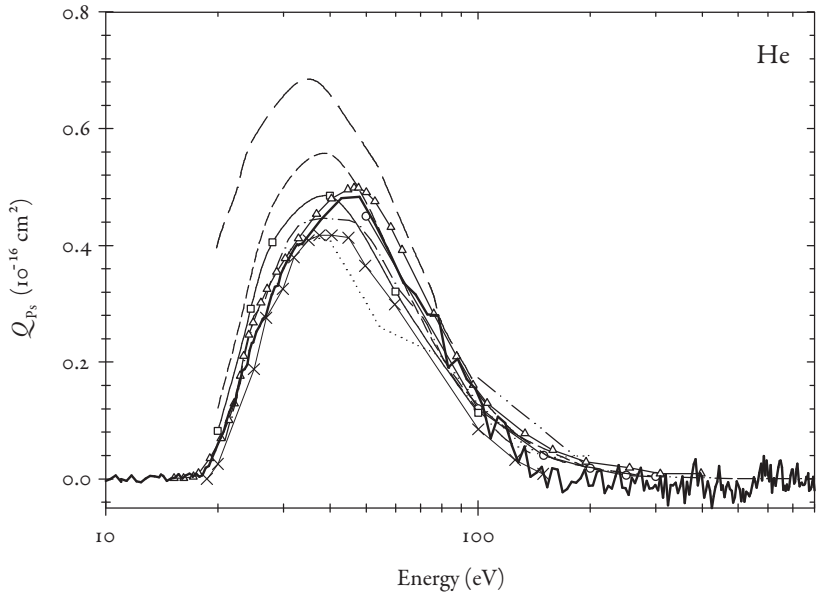

Fig. 1.9: Calculations of Q_{Ps} for He. Solid line with ×—(Utamuratov *et al.*, 2010), solid line with ▵—(Cheng & Zhou, 2007), dotted curve—(Hewitt *et al.*, 1992), solid line with ○—(Igarashi & Toshima, 1992), double chain curve—(Sarkar *et al.*, 1992), long dashed curve—(Schultz & Olson, 1988), short dashed curve—(Mandal *et al.*, 1980), solid line with ▫—(Mandal *et al.*, 1979), thick solid line—experimental results of Murtagh *et al.* (2005).

(1983) and Fornari *et al.* (1983)) comprise the two basic complementary techniques which subsequent groups employed. One approach is to attempt to detect the γ-rays from Ps annihilation, which was used by Charlton *et al.* (1983). This study used a three γ-ray coincidence which provides a unique signal of ortho-Ps formation. The results differ significantly from all other measurements of Q_{Ps} owing mainly to the quenching of ortho-Ps to para-Ps through collisions with the walls of the apparatus (Charlton &Laricchia, 1990). The approach of Fornari *et al.* (1983) was the complete opposite. Rather than attempt to detect Ps directly, its presence was inferred through the absence of a positron in the final state. This involves using a magnetic field to ensure confinement of all scattered positrons in order that the 'missing' positrons may be attributed to Ps formation.

Displayed on Figures 1.7 and 1.9 are various theoretical results for these same cross-sections. As can be seen, there exists at the present time quite a large number of calculations of Q_i^+ and Q_{Ps} for He. For clarity, only the experimental results of Murtagh *et al.* (2005) have been included for comparison. For direct ionization, good agreement can be found between most calculations, though some exhibit an excess at energies above the peak of the cross-section. An exception to this is the distorted-wave Born approximation of Campeanu *et al.* (1996) which displays excellent agreement with experimental results at all energies. For Ps formation, there is again broad agreement between many calculations; the results of Cheng &Zhou (2007) are those of a momentum space coupled-channel calculation, and are notable as the only model of Ps formation in which the energy of the peak of the cross-section is in agreement with the vast majority of experimental determinations. The recent calculations of Utamuratov *et al.* (2010) are in very good agreement with the similarly recent measurements of Caradonna *et al.* (2009), though these have a smaller peak magnitude than any other measurements of Q_{Ps} in He.

1.3.2 Noble gases

Figures 1.10–1.15 show examples of results for the noble gases. Where available, both experimental and theoretical results are shown. Ar and Xe have been chosen to highlight the salient points concerning these measurements.

In the case of Q_i^+ for Ar, fair agreement exists between three determinations. It is instructive at this point to mention the experimental techniques employed by these groups. Marler *et al.* (2005) (and also Jones *et al.* (2009) and Caradonna *et al.* (2009)) used a newly developed positron beam generation technique (Gilbert *et al.*, 1997). The simple radioactive source+moderator arrangement is coupled to a modified Penning–Malmberg

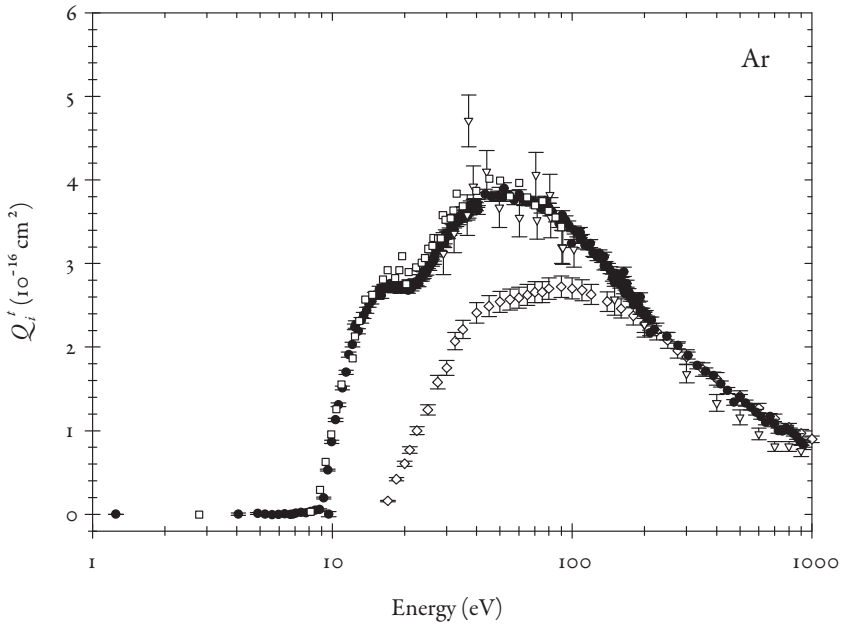

Fig. 1.10: Experimental determinations of Q_i^t for Ar. ▫—(Marler *et al.*, 2005), •—(Laricchia *et al.*, 2002), ▽—(Bluhme *et al.*, 1999b), ◇—electron data of Rejoub *et al.* (2002).

trap (Surko *et al.*, 1989), which uses electric and magnetic fields to confine the positrons. The trap contains a buffer gas (a mixture of N_2 and CF_4) to cool the positrons to around 25 meV before they are ejected by removing one confining electric field. Direct ionization cross-sections were measured using retarding field analysis to determine the energy of the positron in the final state, and thus establish if it had been involved in an ionization event.[§] A moderate magnetic field was employed to ensure complete collection of scattered particles. By contrast, both Laricchia *et al.* (2002) and Bluhme *et al.* (1999b) used detection of the ion, and both used a pulsed positron beam to allow large electric fields to be applied for ion extraction.[¶] Q_{Ps} of Laricchia *et al.* (2002) was extracted from their measurements of Q_i^t and the measurement of Q_i^+ by Moxom *et al.* (1996), assuming that relation 1.13 holds, while Q_{Ps} from Marler *et al.* (2005) was deduced from the loss of a positron from the beam (the technique originally used by Fornari *et al.* (1983)) and Q_i^t from equation 1.13. The

[§] Note that this means these measurements of direct ionization are more accurately described as $\sum_n Q_i^{n+}$ as they include all multiple ionization events.

[¶] The two groups used different pulsing methods, Bluhme *et al.* used a regularly pulsed positron beam whereas Laricchia *et al.* used detection of a positron to trigger biasing off of the beam. Both techniques allow large ion extraction potentials to be used without distorting the positron beam.

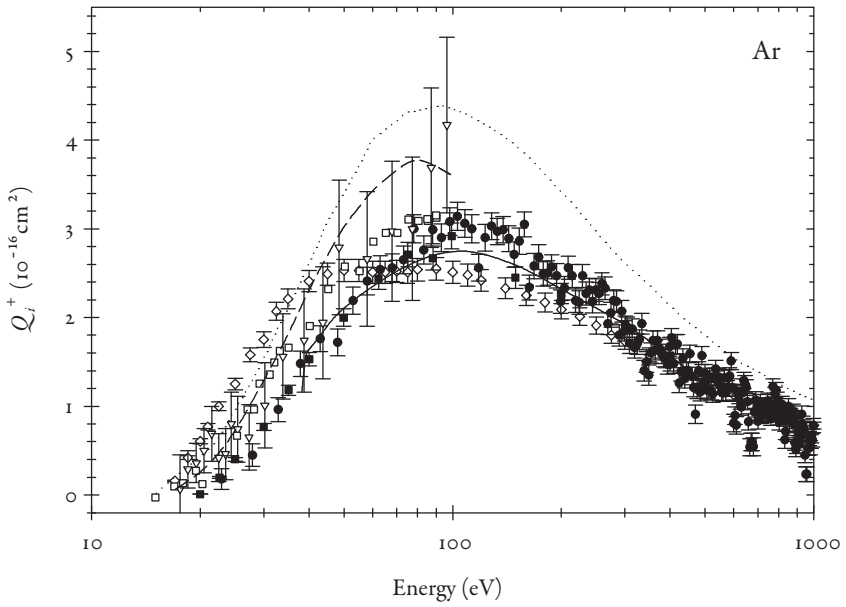

Fig. 1.11: Experimental and theoretical determinations of Q_i^+ for Ar. ▫—(Marler *et al.*, 2005), •—(Moxom *et al.*, 1996), ▪—(Jacobsen *et al.*, 1995), ▿—(Mori & Sueoka, 1994), ◇—electron data of Rejoub *et al.* (2002). Also shown are calculations: dashed line—(Bartschat, 2005), solid line—(Campeanu *et al.*, 2002), dotted line—(Moores, 1998).

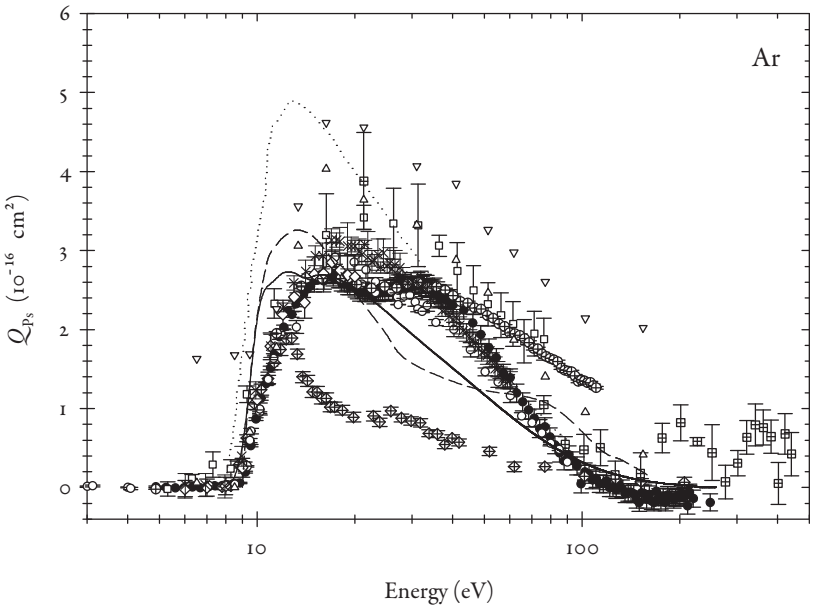

Fig. 1.12: Experimental and theoretical determinations of Q_{Ps} for Ar. ×—(Jones *et al.*, 2009), ○—(Marler *et al.*, 2005), ⊕—(Szłuińska &Laricchia, 2004a), ●—(Laricchia *et al.*, 2002), ▵ and ▿—lower and upper limits of Stein *et al.* (1998), ◇—(Jin *et al.*, 1994), ⊞—(Diana *et al.*, 1986), ⊕—(Charlton *et al.*, 1983), ▫—(Fornari *et al.*, 1983). Also shown are calculations: dotted line—(Dunlop &Gribakin, 2006), solid line—(Gilmore *et al.*, 2004), dashed line—(McAlinden &Walters, 1992).

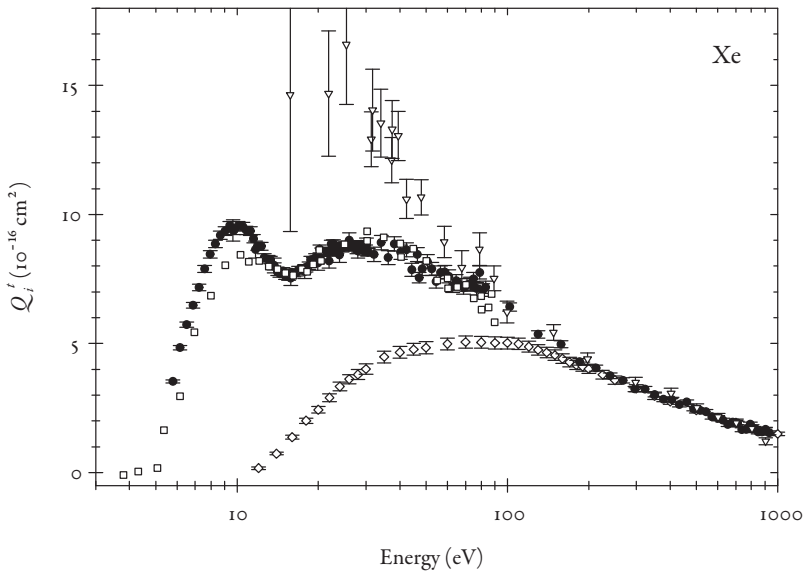

Fig. 1.13: Experimental determinations of Q_i^t for Xe. Legend as Figure 1.10.

limit estimates of Stein *et al.* (1998) were made in the following way: the lower limit (LL) was derived from detection of two γ-rays in coincidence, corresponding to either para-Ps or quenched ortho-Ps, and the upper limit (UL) was a positron loss measurement with intentionally small angular acceptance, encompassing both Ps formation and large-angle scattering loss mechanisms.

There are still some significant differences among measurements of Q_{Ps}. While those of Charlton *et al.* (1983) are widely acknowledged to have suffered from the quenching effect described earlier for He, there is still some dispute over the existence of the second peak, observed by Laricchia *et al.* (2002) but not by Marler *et al.* (2005) or Jones *et al.* (2009). Its presence has been attributed to both excited-state Ps (Laricchia *et al.*, 2002; Gilmore *et al.*, 2004, see also Chapter 3) and Ps formation from inner-shell electrons (Stein *et al.*, 1998; Dunlop &Gribakin, 2006), while its existence was corroborated by γ-ray–ion coincidence measurement (Szłuińska &Laricchia, 2004a), even though the authors found that these were affected by poor confinement of scattered positrons with increasing energy.

In the case of Xe (Figures 1.13–1.15), there is good agreement in Q_i^t between Marler *et al.* (2005) and Laricchia *et al.* (2002) but the measurement of Bluhme *et al.* (1999b) disagrees in magnitude below 100 eV. As with Ar, there is significant accord among mea-

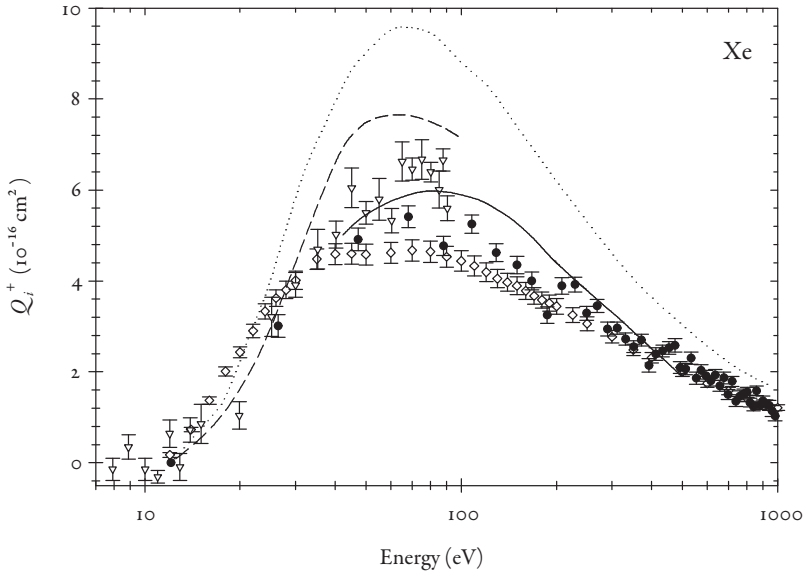

Fig. 1.14: Experimental and theoretical determinations of Q_i^+ for Xe. ▽—(Marler *et al.*, 2005), •—(Kara *et al.*, 1997), ◇—electron data of Rejoub *et al.* (2002). Also shown are calculations (legend as Figure 1.11).

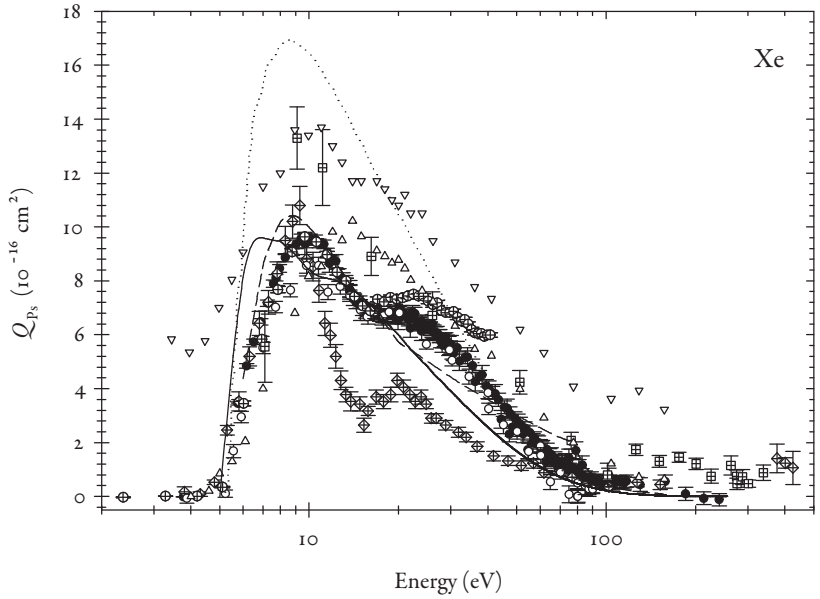

Fig. 1.15: Experimental and theoretical determinations of Q_{Ps} for Xe. Legend as figure 1.12, though lacking data from Jin *et al.* (1994) and Fornari *et al.* (1983).

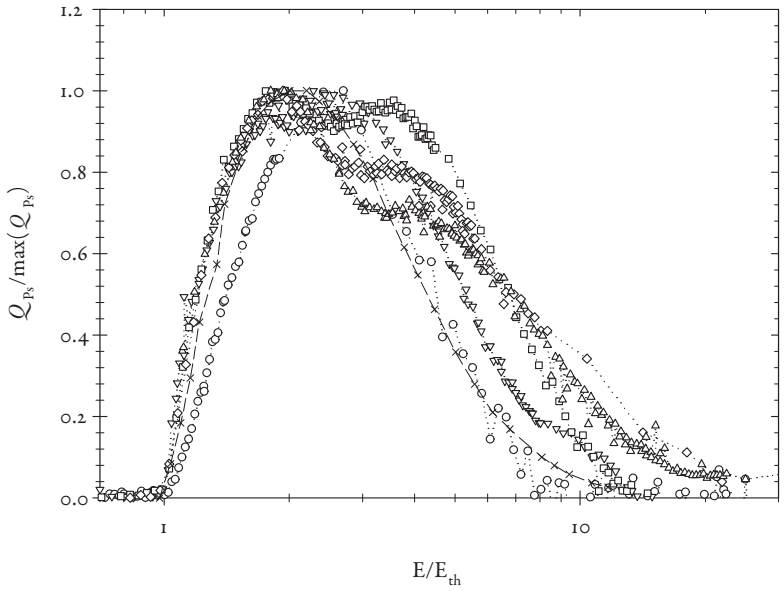

Fig. 1.16: Demonstration of the empirical scaling law (equation 1.14) for H, He and the noble gases. Dashed line with ×—H (Kernoghan *et al.*, 1996), ○—He (Murtagh *et al.*, 2005), ▽—Ne, □—Ar, ◇—Kr and △—Xe (Ne–Xe from Laricchia *et al.*, 2002).

surements of Q_i^+, and only small differences among recent measurement of Q_{Ps}. There is again a second peak, though less pronounced than that of Ar—more a saddle point than a full peak—which has again been attributed to either excited-state Ps or inner-shell ionization.

For the heavier noble gas targets (in contrast to He), agreement between theory and experiment is significantly worse, and calculations are sparser (these are shown on the appropriate figures). For Ar and Xe Q_i^+, the best agreement with experiment is again with the results of Campeanu *et al.* (2002), using a similar method as for He, with other theories overestimating the magnitude (though largely agreeing on energy dependence). For positronium formation, shape agreement is reasonable at best, with all theoretical determinations peaking ~ 5 eV earlier than experimental results, and only a hint of the double-peaked structure visible.

1.3.3 Excited-state Ps formation

As mentioned in the previous section, the origin of the double peak structure evident in some (e.g. Laricchia *et al.*, 2002) measurements of Q_{Ps} for the noble gases has been attributed (Laricchia *et al.*, 2002) to the formation of Ps in an excited state. This hypothesis led the authors to construct estimates of the upper and lower limits on the cross-section for its formation from noble gas target, via the following arguments.

An analysis in 2002 (Laricchia *et al.*) of Q_{Ps} for H, He and the noble gases revealed that by normalizing the energy scale by the threshold and the magnitude scale by the peak height, a broadly common curve could be attained for all these targets in the low energy range, before additional ionization channels become competitive (see Figure 1.16). For H and He, the empirically scaled curve is similar across the entire range of the measurements; for the other gases, deviation occurs after the first peak. Laricchia *et al.* (2002) used a scaling of the form:

$$\frac{Q_x^A\left(\frac{E}{E_{th}}\right)}{Q_x^A\big|_{\max}} = \frac{Q_x^B\left(\frac{E}{E_{th}}\right)}{Q_x^B\big|_{\max}}, \tag{1.14}$$

where Q_x^A refers to the cross-section for a process x in a target gas A with a threshold energy of E_{th}, to fit the ground state Ps formation cross-section in He of Campbell *et al.* (1998) to the first peak of Q_{Ps} in the noble gases. Noting that the first peak occurred at twice the threshold energy for ground-state Ps formation, and the second peak at twice that for $n = 2$ Ps formation, the difference between the two curves was attributed to excited-state Ps. This produced an estimate of the upper limit of Q_{Ps}^*, albeit one which is an underestimate at low energies.

An estimate of the lower limit on Q_{Ps}^* was produced by fitting an exponential decay onto the first peak of each of the noble gases Q_{Ps} (with the exception of Ne, which does not exhibit the double peak structure). The difference between the curves provides the estimate, which is again an underestimate at low energies, for the same reason as above.

1.4 Ionization and excitation of molecules

This section will discuss ionization and excitation processes for small molecules. In addition to the those described by reactions 1.3–1.10 (all of which are perfectly valid for atoms or molecules), a number of additional outcomes exist for positron–molecule interactions.

These are all dissociative, and are summarized by the following reactions (1.15–1.24):

$$e^+ + AB \rightarrow A + B + e^+ \tag{1.15}$$

$$e^+ + AB \rightarrow A + B^* + e^+ \tag{1.16}$$

$$e^+ + AB \rightarrow A^+ + B + Ps \tag{1.17}$$

$$e^+ + AB \rightarrow A^+ + B + e^+ + e^- \tag{1.18}$$

$$e^+ + AB \rightarrow A^+ + B^* + Ps \tag{1.19}$$

$$e^+ + AB \rightarrow A^+ + B^* + e^+ + e^- \tag{1.20}$$

$$e^+ + AB \rightarrow A^{+*} + B + Ps \tag{1.21}$$

$$e^+ + AB \rightarrow A^{+*} + B + e^+ + e^- \tag{1.22}$$

$$e^+ + AB \rightarrow A^+ + B^+ + Ps + e^-. \tag{1.23}$$

$$e^+ + AB \rightarrow A^+ + B^+ + e^+ + 2e^-. \tag{1.24}$$

Ionization and excitation processes in molecules are more complex than those for atoms, reflecting the increased complexity of the electronic structure and additional degrees of freedom. For the small molecules dealt with in this thesis, it is instructive to consider the potential energy curve when discussing ionization and dissociation. This shows the variation of the electronic energy in a molecule with internuclear distance for various bound states. A generic potential energy curve is shown in Figure 1.17, highlighting the significant features which lead to the different outcomes following excitation compared to atoms.

It should first be noted that the timescales involved in positron (and electron) impacts do not allow for significant molecular rearrangement. The projectile energies used in this thesis allow for a typical collision timescale of approximately 0.01–0.1 times that for nuclear rearrangement. Transitions between molecular states caused by these collision can therefore initially be considered optical, that is, vertical in terms of internuclear separation. This is a statement of the Franck–Condon principle (Franck &Dymond, 1926; Condon, 1926), which can be used to predict the vibrational levels capable of being occupied following an excitation. The shaded areas on Figure 1.17 show the limits of the internuclear separation in the lowest vibrational state of the state X; the Franck–Condon principle states that after an excitation the separation will still be within those limits. Hence, from this it is possible to predict the outcome of the various excitations shown. The state B is fully dissociative, so excitation of this state will result in fragmentation of the molecule. A is also a dissociative state as: although it has a minimum in potential energy, a verti-

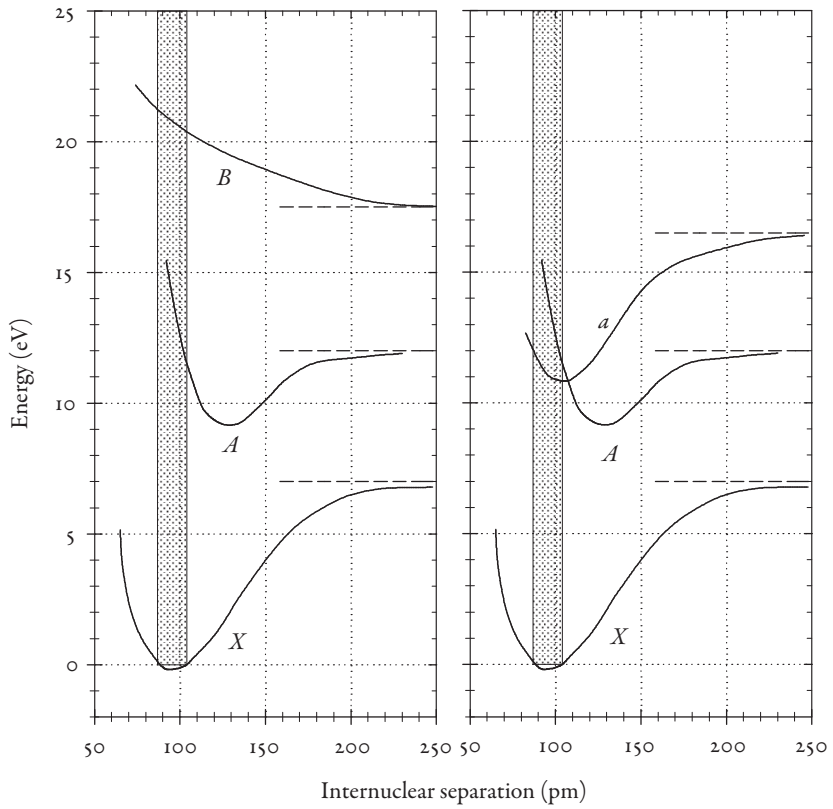

Fig. 1.17: Generic potential energy curve showing the ground state X and three excited states (A, B and a). The shaded area shows vertical transitions according to the Franck–Condon principle. State B is fully dissociative, A partially so and a not directly, though has some overlap with A, and so is predissociative. Dashed lines show the local dissociation limits.

cal transition from X leads to higher vibrational levels, most of which are above the local dissociation limit. When considered alone, a is a simple non-dissociative state, of note because the Franck–Condon principle predicts that the most populated vibrational level following excitation from X will not be $v' = 0$. However, when considered in conjunction with A, the a state becomes partially *predissociative*, that is, it can undergo a radiationless transition to A which will then leave the molecule either in an excited state or above the local dissociation limit. It can be seen from this that dissociation and excitation are closely

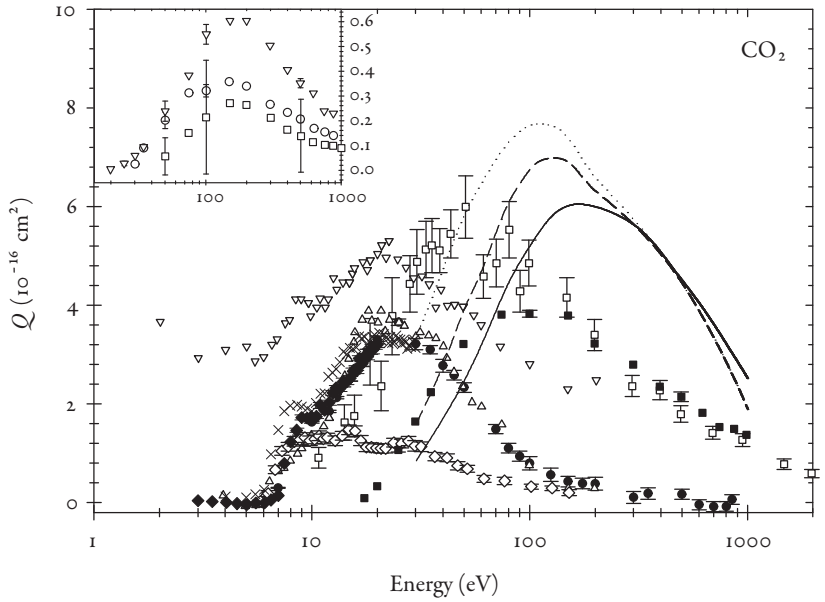

Fig. 1.18: Positron–CO_2 ionization (and excitation) cross-sections. ×—Q_{Ps} (Kauppila *et al.*, 2004a), ▫—Q_i^t (Bluhme *et al.*, 1999a), ▪—Q_i^+ (Bluhme *et al.*, 1999a), •—Q_{Ps} (Murtagh *et al.*, 2006), ▵ and ▿—lower and upper limits (respectively) of Q_{Ps} (Kwan *et al.*, 1998), ◆—(Laricchia &Moxom, 1993), ◇—Q_{Ps} (Griffith, 1984). Theory: solid line—CPE, dotted line—ES, and dashed line—TS: DWBA calculations of Tóth *et al.* (2006). Inset shows direct dissociative ionization cross-sections of Bluhme *et al.* (1999a). ○—CO^+, ▿—O^+, ▫—C^+, for clarity the corresponding total dissociative cross-sections have been omitted.

linked processes.[‖]

Figure 1.18 and 1.19 are a compilation of the available ionization cross-sections for CO_2 and N_2 prior to this work. These targets are typical small molecules, one is a diatomic, the other a linear triatomic, and are the subject of Chapter 4. Theoretically modelling collisions with such complex targets is challenging, so calculations of these cross-sections

[‖] The assignment of letters to molecular states is usually in order of ascending energy, with the ground state always labelled *X*. However, as the identification of molecular states has occurred over a period of several decades, there is a certain historical element to the ordering as well, those identified earlier often having lower letters than later ones, regardless of energy. The case of the letters usually follows the multiplicity of the state where upper case has the same multiplicity as the ground state. A notable exception to this rule is N_2, where triplets are represented by upper case, and singlets by lower case.

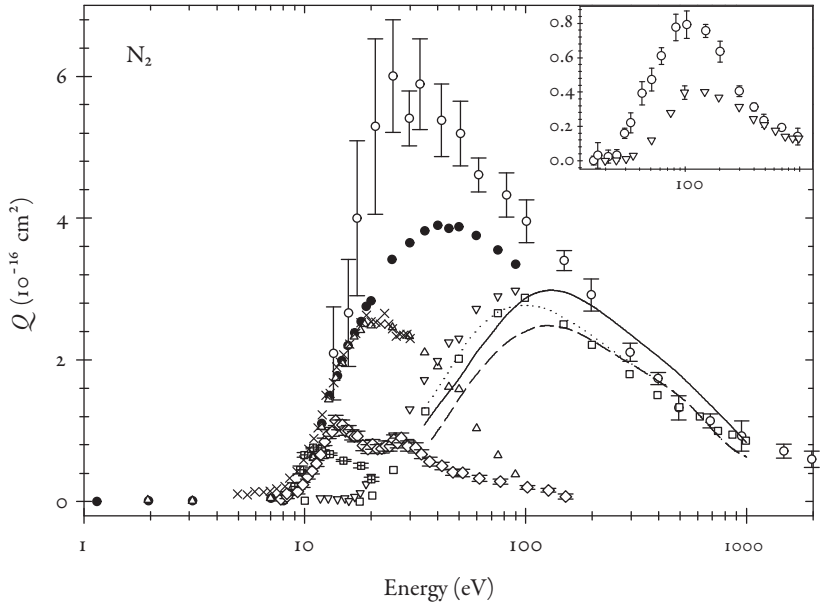

Fig. 1.19: Positron–N_2 ionization (and excitation) cross-sections. •—Q_i^t (Marler &Surko, 2005), ○—Q_i^t (Bluhme *et al.*, 1998), ▽—Q_i^+ (Marler &Surko, 2005), □—Q_i^+ (Bluhme *et al.*, 1998), △—Q_{Ps} (Marler &Surko, 2005), ◇—Q_{Ps} (Griffith, 1984), ⊞—cross-section for excitation to $a\ ^1\Pi$ state (Marler &Surko, 2005). Legend for theory as Figure 1.18. Inset shows cross-sections for formation of N^+ (Bluhme *et al.*, 1998): ○—Q_i^t, ▽—Q_i^+.

are severely lacking. As such, the experimental and theoretical results will be discussed together.

The experimental methods employed have been largely discussed in the previous sections. An additional piece of information concerning the measurements of Bluhme *et al.* is that for identifying different fragments of molecules, time-of-flight (TOF) mass spectroscopy was used. This is based on the fact that lighter fragments will be accelerated by an electric field to the same velocity more swiftly than heavier ones with the same charge, so the time of flight between the creation of the ion and its subsequent detection is shorter for lighter ions. Note that this is only capable of identifying ions with different mass-to-charge ratios, so, for example, the signal for N^+ is indistinguishable from that for N_2^{2+}. Also of note is the excitation cross-section of Marler &Surko (2005) the first measurement of its kind. The trap-based beam system has a small enough energy spread ($\sim$ 50 meV) that different vibrational states of the $a\ ^1\Pi$ state could be resolved using retarding

field analysis.

The only theoretical consideration of these molecules is that of Tóth *et al.* (2006), which is a distorted-wave Born approximation (DWBA) calculation with three different ways of treating the incoming and outgoing particles. The simplest of these is the CPE calculation, which uses plane waves to model the incoming projectile, while the scattered particles are described by Coulomb waves. There are two variations on this which improve on the relatively simple CPE calculation by adjusting the potential experienced by either the outgoing electrons (ES) or both outgoing and incoming particles (TS). The initial state of the molecule is always described by a multicentred Gaussian, however, the ES model uses a field comprising the ionic field screened by the remaining electrons when dealing with the scattered electrons, with or without a contribution from the scattered positron depending on the relative velocities of the two particles (the positrons move in the same fields as in the CPE model). The TS model uses modified fields for both electrons and positrons. The use of a single centred potential in describing the outgoing wavefunctions has been identified as the reason for the relatively poor performance of the theory in modelling the CO_2 cross-sections (Tóth *et al.*, 2006).

Similar to the case for noble gases (see Section 1.3.3), it had been hypothesized (Kwan *et al.*, 1998) that structure visible in Q_i^t for CO_2 may arise from the formation of excited-state Ps formation. However, upon investigation of this hypothesis using photon–γ-ray coincidences (Laricchia *et al.*, 1988), a large signal was observed which could not be attributed to excited-state Ps. The detection of photon–γ-ray coincidences in which the γ-ray preceded the photon implied that significant amounts of Ps was being formed leaving the resultant ion in an excited state.

1.5 Comparison of projectiles

One of the fundamental reasons for studying positron interactions with matter is as a probe for matter/antimatter disparities. This section will briefly discuss the observed differences between using matter and antimatter projectiles. Additionally, this will afford the opportunity to examine the effect of projectile mass on cross-sections by including data for proton and antiproton impact in the discussion.

A comparison of matter and antimatter projectiles is shown in Figures 1.20 and 1.21. The data are plotted against velocity rather than energy to map measurements using particles of differing masses onto a common scale. They include only direct ionization—suffice

to say that in comparison of total ionization cross-sections, positive projectiles have larger ionizing capabilities at low velocities than their negative counterparts as a result of the capture process. Hence it is more instructive to compare direct ionization. These plots demonstrate that charge independence of ionization occurs at high impact velocities. Note that as the data have been transformed on to a common scale, the location of the ionization threshold depends on projectile mass (and hence the heavier projectile possess much larger cross-sections at low velocities than do light ones).

In the case of He, it is apparent that around its peak energy ionization by positive projectiles is enhanced over that by negative projectiles, even disregarding the effects of capture. This is a common observation for atoms (see, for example, the review by Knudsen &Reading, 1992), attributable to polarization of the target.** Another common feature is the reversal of this situation at the lowest impact energies, the cross-sections for ionization by positive projectiles fall below those for their negative counterparts. This is attributed to a combination of factors. At low velocities a heavy negative projectile passing though the electron cloud will decrease the binding of target electrons, whereas a heavy positive projectile will increase it. The lighter particles will be deflected by the field of the target nucleus, leading to an increase in collisions for negative projectiles and a corresponding decrease for positive projectiles (the so called 'trajectory effect': Paludan *et al.*, 1997). In addition, flux for positive projectiles must be shared between direct ionization and capture processes, unlike for negative ones. At higher impact velocities, this last effect becomes increasingly unimportant as capture cross-sections fall to zero.

For N_2, the features described for He are less clearly defined, though may still be present. It is still evident that the cross-sections for ionization by all four projectiles merge at sufficiently high impact velocities. However, it is less convincing that positive projectiles necessarily produce larger cross-sections, and insufficient data exist to conclusively demonstrate the cross-over of cross-sections at low velocity.

1.6 Motivation for present work and future work

The present study has measured cross-sections for processes which have not previously been examined using positrons as a projectile. For atomic targets, this includes the formation of Ps in an excited state, in an effort to gain deeper insight into the structure visible

** This feature becomes less significant with increasing Z, owing to the larger static interaction of higher Z targets.

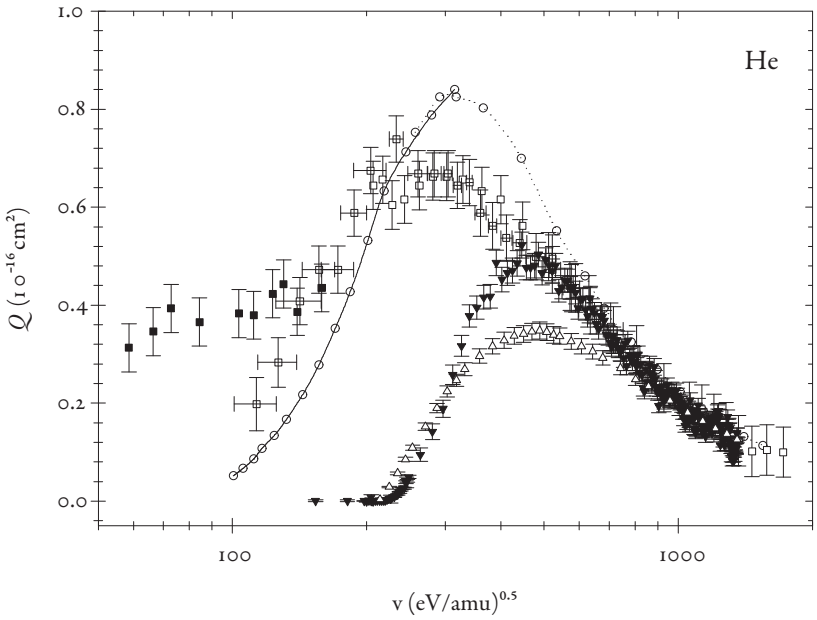

Fig. 1.20: Comparison of direct positron- (▾), electron- (▵), proton- (curves with ○) and antiproton-impact (■, ▫, ⊞) ionization cross-sections for He. Positron data is from Moxom *et al.* (1996); electron data from Rejoub *et al.* (2002); proton data from Shah &Gilbody (1985); Shah *et al.* (1989); antiproton data is from Knudsen *et al.* (2008) (■), Andersen *et al.* (1990) (▫) and Hvelplund *et al.* (1994) (⊞).

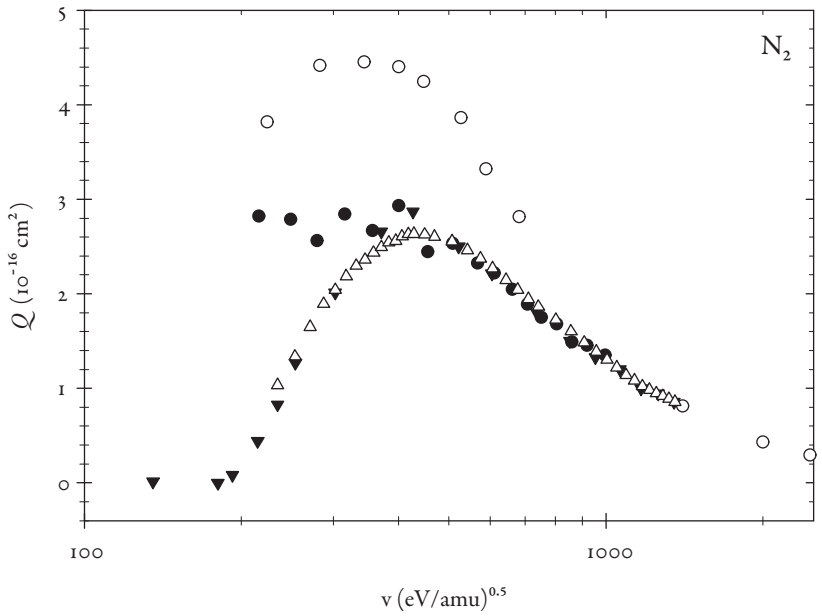

Fig. 1.21: Comparison of current positron (▾), electron (▵), proton (○) and antiproton (●) total ionization cross-sections for N_2. Data for protons and antiprotons from Knudsen *et al.* (1995), electrons from Straub *et al.* (1996b) and positrons from Bluhme *et al.* (1998).

in Q_{Ps} for Xe (and the other noble gases). The approach used, namely photon–ion coincidences, allows more rapid data collection than the use of γ-ray–photon measurements used in earlier studies of excited-state Ps.

This work provides a test of the estimates of Laricchia *et al.* (2002) of the lower and upper limits for the formation cross-section of excited-state Ps from the noble gases as discussed in Section 1.3.3. These limit estimates predicted an increase of the significance of excited-state Ps production to Q_{Ps} with increasing Z of the target. This work provides some supporting evidence for this hypothesis.

For molecular targets, the ionization–excitation processes were studied fundamentally to examine matter/antimatter disparities. Following the work of Laricchia *et al.* (1988), who observed significant signal in γ-ray–photon coincidence measurements in CO_2 which could not be attributed to excited-state Ps, this work has determined absolute cross-sections for these processes in CO_2 and N_2. The results reveal an enhancement in ionization–excitation by positron impact over that for electron impact, above that which would be expected from a comparison of total ionization cross-sections.

At this point, the two branches of study become convergent; while a direct determination of the cross-section for excited-state Ps in CO_2 was not possible, an estimate could be made for N_2.

2. EXPERIMENTAL METHOD: APPARATUS AND TECHNIQUES

The general experimental apparatus and analysis techniques employed during this research are described in this chapter. Where modifications specific to a particular measurement have been made, these are described in the relevant chapter. The first part of this chapter is devoted to describing the apparatus in detail. A diagram representing the main features of the beamline is shown in Figure 2.1. This can be roughly divided into 3 sections: the source chamber, the transport system and the interaction region. These are discussed in detail in sections 2.1.1–2.1.3. The second part of the chapter deals with the problem of establishing an absolute scale for the measurements—the process known as *normalization*. The third and final part of the chapter deals with other experimental considerations which do not necessarily fall into either category.

2.1 Apparatus

The system itself comprises an approximately 3 m long vacuum system constructed largely from brass chambers with rubber seals, evacuated with 4 diffusion pumps containing Santovac® 5 oil (three at 600 ls^{-1}, a fourth at 150 ls^{-1}) and backed by 3 rotary pumps. This provides a basic pumpdown time of the order of 1 hr, achieving a pressure of $\sim 1 \times 10^{-2}$ torr, with conditions appropriate for experimentation ($\sim 1 \times 10^{-6}$ torr) reached after approximately 12 hours. The main principle of beam operation is as follows. Fast positive β-particles from a ^{22}Na source are moderated using annealed tungsten meshes, from which they are ejected with an energy of approximately 2.4 eV.* These are then accelerated to energies up to 850 eV by a positive potential applied to the moderator, and confined radially by the magnetic field generated by 12 Helmholtz coils (labelled 1–12) and a solenoid, as indicated in Figure 2.1. The beam passes through the interaction region—a hemispherical gas-cell constructed from polished aluminium—and is finally detected by a channel elec-

* As determined by Kara (1999) and Szłuińska &Laricchia (2004b) using time-of-flight measurements.

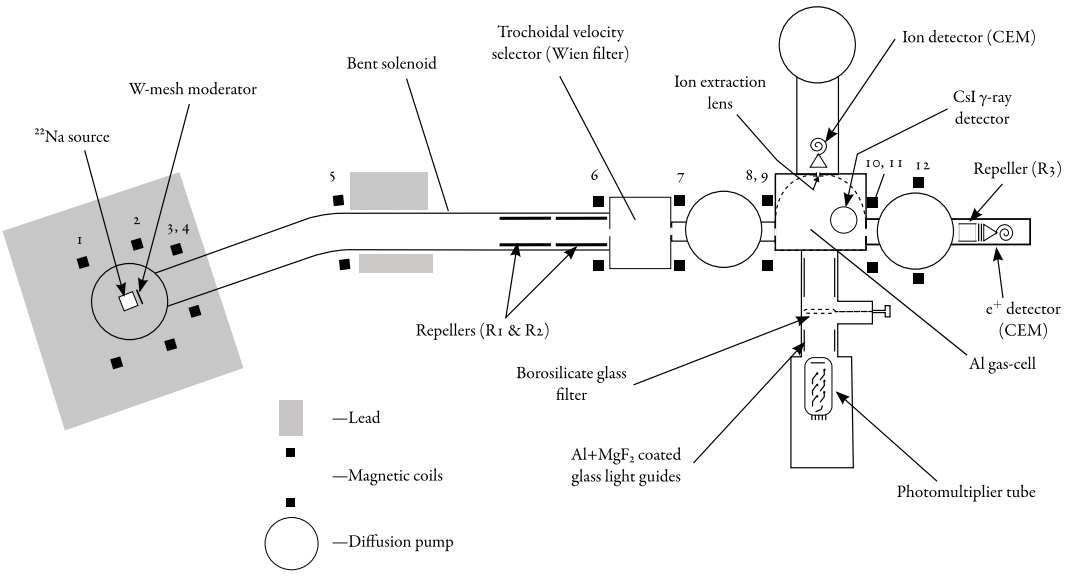

Fig. 2.1: Schematic of the experimental set-up.

tron multiplier (CEM) at the end of the beamline. Surrounding the interaction region are 3 additional detectors for ions or photons (both low and high energy).

The signal from the detectors can be counted on two multichannel scalers (MCS), or in coincidence with each other on three multichannel analysers (MCA). This allows a wide variety of measurements to be taken simultaneously, ensuring that the conditions under which the measurements are taken are identical. It also allows normalization of measurements to proceed in a self-consistent way (as discussed in detail in Section 2.2.2). A typical set-up is shown in Figure 2.2, with 3 coincidence measurements and one scaler measurement recorded simultaneously.

2.1.1 Source region

The ^{22}Na source (as supplied by iThemba LABS) takes the form of a spot of NaCl deposited in a metal capsule. ^{22}Na decays via positive β (positron) emission (90%) or K-electron capture (10%) (Endt &Kluyver, 1954) to an excited state of ^{22}Ne which then decays with a lifetime of 10 ps by emitting a 1.274 MeV γ-ray, according to the following reactions:

$$^{22}\mathrm{Na} \rightarrow {}^{22}\mathrm{Ne}^{*} + \mathrm{e}^{+} + \nu \tag{2.1}$$

$$^{22}\mathrm{Ne}^{*} \rightarrow {}^{22}\mathrm{Ne} + \gamma. \tag{2.2}$$

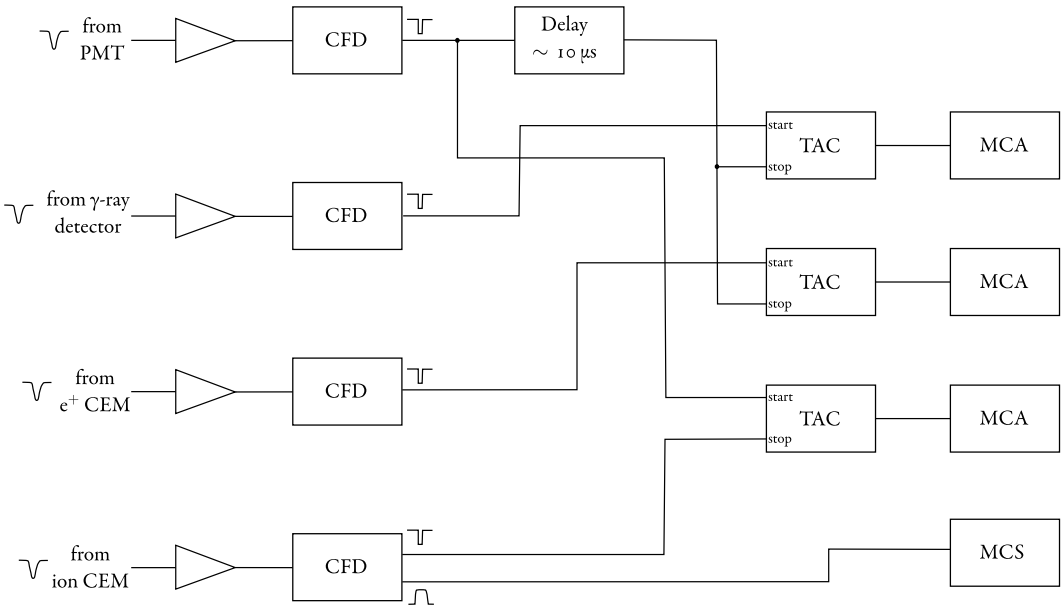

Fig. 2.2: Typical three-coincidence set-up. Here the measurements being taken would be γ-ray–photon, e^+–photon, photon–ion, and the total ion yield.

A positron is generally emitted with an energy up to 546 keV[†] which must be reduced (moderated) before it is useful for low-energy positron impact studies. In this experiment, this reduction is achieved using a number of overlapping tungsten meshes placed in close proximity to the front of the source capsule. These meshes were either used at normal thickness (approximately 25 μm), or were etched by immersion in heated NaClO solution for up to 30 minutes, until the mass of the mesh had been reduced by 80% (Williams, 2009). The meshes were then annealed at 2000 °C for ~ 20 minutes in order to remove impurities and defects in the crystal lattice (Wilson &Mills, 1983). As described in Section 1.2.3, the mechanism for moderation in tungsten may be summarized thus: energetic positrons impinge on the surface of the meshes and enter the bulk of the metal, where they lose energy through interaction with the lattice. They achieve approximately thermal energies before being ejected from the surface with an energy equal to the magnitude of the work function of the metal ($|\phi|$). The moderator assembly can be held at any potential between 0 and ~ 1000 V which allows the energy of an ejected positron to be defined as

$$E_p = eV_m + |\phi| \,. \tag{2.3}$$

[†] Up to 1.83 MeV is possible, via decay directly to the ground state of ^{22}Ne, though this is rare.

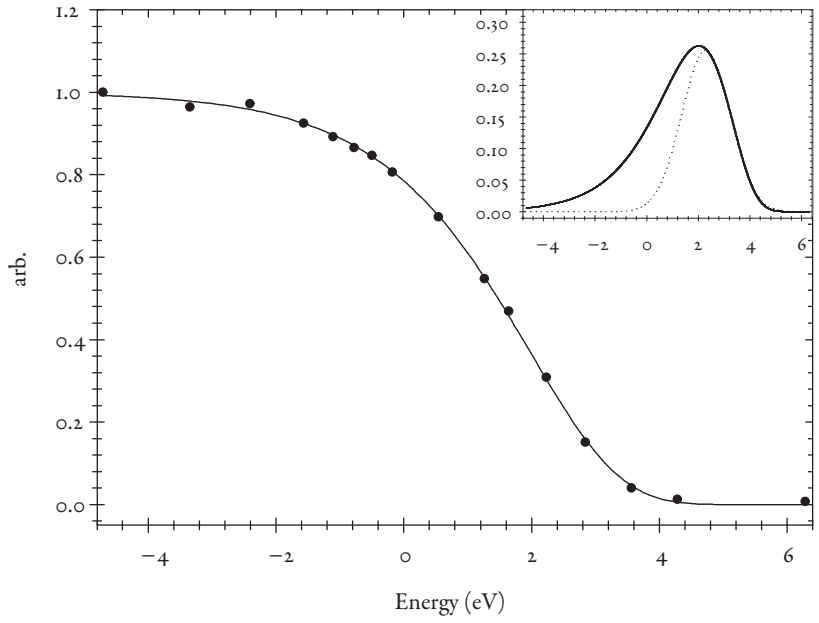

Fig. 2.3: Variation of intensity of positron beam with excess energy (measured—•, Gompertz fit—continuous curve). Applied retarding voltage V_r has been transformed into an energy scale (in eV) by $E = V_r - V_m$. Inset shows the negative derivative of this curve (continuous curve) giving the energy distribution and a Gaussian fit to the high energy half (dotted curve).

The ejection energy of the positrons will have a distribution as a result of inelastic scattering from surface impurities on the moderator. A typical *beam* energy distribution is shown in Figure 2.3, measured using a biasing potential applied to a grid (G2 in Figure 2.5—a double grid is used in order to reduce field penetration from the CEM cone) positioned immediately in front of the positron detector. This plot reveals several aspects of the beam energy distribution. First, it is asymmetric, in part as a result of the magnetic field in the detection region. Positrons with high-pitch-angle flight paths, while having the same kinetic energy as those with lower pitch angles, have a larger component of their momentum perpendicular to the direction of the beam. When approaching an electric field which is parallel to the magnetic field, these positrons will be registered as having a lower effective kinetic energy as only the parallel component of their velocity is analysed—hence the longer tail at lower energies. A Gaussian fit to the higher energy half of the distribution is shown in the inset of Figure 2.3 to emphasize this asymmetry. Secondly, the cut-off energy corresponds to $|\phi|$ for the moderator, which is significantly larger in non-UHV conditions than that for clean tungsten metal (−2.95 eV, Wilson &Mills, 1983). In addition, it can be seen that the modal energy is approximately 2 eV above the moderator voltage. This is used to represent the average beam energy (as distinct from the energy of the ejected positrons) thus:

$$E_b \approx eV_m + 2.0. \tag{2.4}$$

Two pairs of Helmholtz coils (labelled 1–4 on Figure 2.1) and a Pb collimator confine and define the beam emerging from this region.

2.1.2 Transport region

Between the ^{22}Na source and the gas-cell there are a number of features designed to 'clean up' the flux of particles emerging for the source region. In order of appearance (left to right on Figure 2.1), these are:

1. the solenoid, which has a 15° bend around which the beam turns with the assistance of coil 5;

2. a cylindrical electrode (R1) normally grounded, but which may be biased at V_m + 9 V;

3. another cylindrical electrode held at −500 V (R2); and

4. a Wien filter.

The purpose of 1, 3 and 4 is to remove unwanted components from the beam. These are principally un-moderated positrons, γ-rays and secondary electrons.

Fast positrons are poorly confined by the magnetic field from the solenoid, so will fail to make it round the corner, instead annihilating on the chamber wall (to lower the background γ-ray count, lead shielding is also placed around this corner). This also serves to remove direct line-of-sight between the ^{22}Na source and the interaction region, further lowering the background γ-ray count.

The Wien filter (see Figure 2.4), named after its inventor Wilhelm Wien, also serves to remove fast positrons from the beamline. It comprises perpendicular electric and magnetic fields produced by curved parallel plates and Helmholtz coils, respectively. This arrangement of fields transmits only a small range of velocities between fixed points for a given electric field **E** and so behaves as a monochromator. The curvature of the plates and outward flared of the plates at both ends serve to reduce distortion of the beam spot (Hutchins *et al.*, 1986). Charged particles will follow a trochoidal path through this system, hence the alternative name for this device—trochoidal velocity selector. The **E** field is varied by adjusting the voltage on the plates according to:

$$V = \pm A\left(\sqrt{V_m} + k\right) \tag{2.5}$$

where A is a proportionality constant, and k reflects the difference between beam energy and moderator voltage (see equation 2.4). This may be understood by considering the equation of motion of a charged particle in perpendicular electric and magnetic fields, which may be formed from the velocity **v**:

$$\mathbf{v} = v_x\mathbf{i} + v_y\mathbf{j} + v_z\mathbf{k} \tag{2.6}$$

and the force **F**:

$$\mathbf{F} = q\left(\mathbf{E} + \mathbf{v} \times \mathbf{B}\right). \tag{2.7}$$

For simplicity, it is assumed $\mathbf{B} = B_z\mathbf{k}$ and $\mathbf{E} = E_y\mathbf{j}$, which allows the equation of motion for the x-component of the velocity to be written as:

$$\frac{d^2v_x}{dt^2} = \left(\frac{q}{m_e}\right)^2 \left(E_yB_z - B_z^2v_x\right) \tag{2.8}$$

which has a general solution of simple harmonic motion and a particular solution of:

$$v_x = \frac{E_y}{B_z}. \tag{2.9}$$

This has no dependence on the velocity parallel to $\mathbf{B}$ (v_z), so in order for the vertical displacement l of the beam to be equal at all energies, the following condition must be satisfied:

$$E_y = \frac{lv_zB_z}{L} \tag{2.10}$$

where L is the length of the filter. Expressing v_z in terms of energy, and substituting in equation 2.4 for the beam energy yield equation 2.11:

$$E_y = \frac{lB_z}{L}\sqrt{\frac{2\left(V_m + 2\right)}{m_e}} \tag{2.11}$$

which is of the form of equation 2.5. It is most sensibly expressed arranged this way as the $\mathbf{B}$ field is fixed, so it can be seen that the $\mathbf{E}$ field can be modified simultaneously with the moderator voltage V_m by the use of a square-rooter, an electronic circuit whose output is proportional to the square root of its input, V_m in this case.

Electrons may be produced by the impact of a positron on a surface virtually anywhere in the beamline, though the largest sources are the moderators, their holders and the ^{22}Na source itself. Secondary electrons produced by unmoderated positrons may have large energies, and are effectively removed by the same mechanisms which remove fast positrons. Those produced by moderated positrons will be guided by the magnetic field just as easily, though will have a large energy distribution, so to reduce their transmission, the repeller R2 is held at −500 V. Reversing the moderator potentials and grounding the repellers allows the beam to function additionally as an electron beam.

For all measurements, it is important not only to minimize the contribution that these unwanted components of the beam may give to the signal but also to measure and subtract

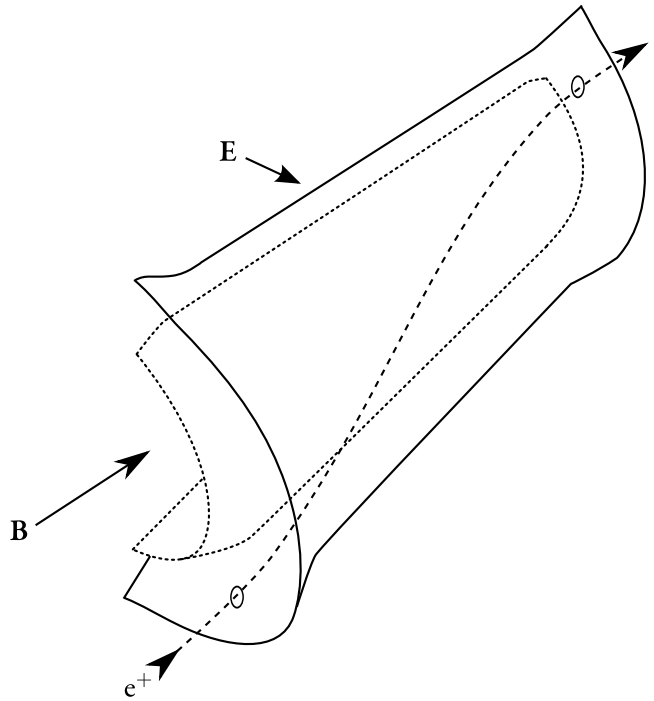

Fig. 2.4: A Wien filter, with curved field plates and flared ends. The path a positron takes through the system is shown as a dashed line (circles mark the entry and exit points).

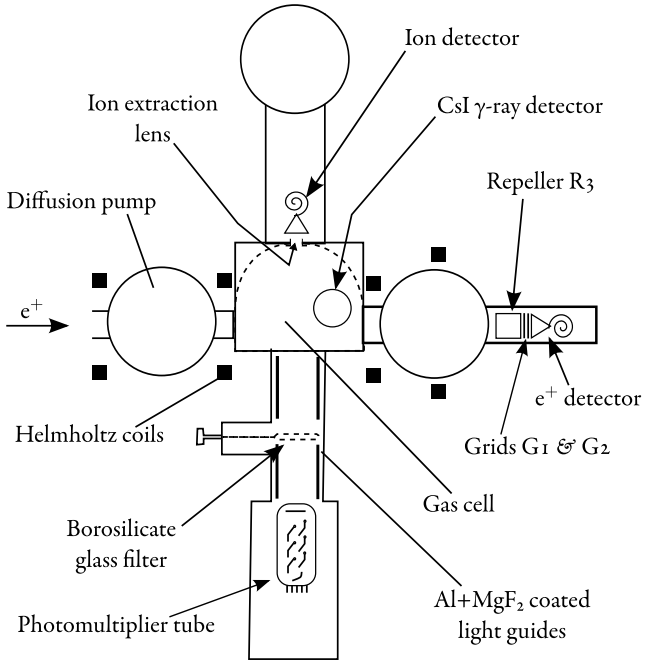

Fig. 2.5: Detailed view of the gas-cell. The inner surface (dotted line) is polished aluminium.

it. R1 allows the slow portion (with $E < eV_m + 9$ eV) of the beam to be biased off to perform a measurement of the 'fast particle background'.

2.1.3 Interaction region

A more detailed view of the interaction region is shown in Figure 2.5. The gas is introduced into the cell, and its pressure controlled, by a Pfieffer valve, itself controlled by a LabVIEW analogue output. The pressure is monitored by a capacitance manometer (MKS Baratron model 127AA-00001A) with a 10 torr range. A positron passing through the gas in the cell may produce any or all of the following: a photon, an ion or a γ-ray, any of which, with the exception of the γ-ray, may be accompanied by the transmission of the positron itself. Hence, the interaction region is viewed by a photomultiplier tube (PMT) with a wavelength sensitivity range of 200–600 nm, a CEM for detecting ions and an externally mounted CsI scintillation crystal coupled to an avalanche photodiode for detecting γ-ray photons. Once the beam has passed through the gas-cell, it is detected using a second CEM. Note that this CEM has four grids placed in front of it, each of transmission 85%.

The ion detector is located behind a small cylindrical (internal diameter 0.5 mm, length 3 mm) electrostatic lens held at −500 V, with its axis positioned perpendicularly to the

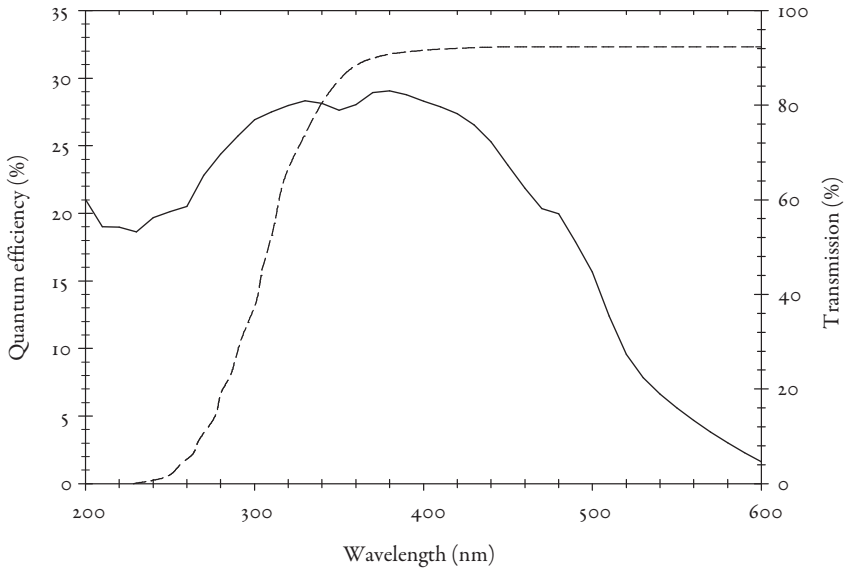

Fig. 2.6: Wavelength dependence of PMT quantum efficiency (continuous curve) as supplied by the manufacturer (ET Enterprises Ltd.) and borosilicate glass transmission (dashed curve—scale on right-hand axis), supplied by Advanced Telescope Supplies: `http://www.atscope.com.au/photometry.html`.

direction of the beam. It creates an electric field which allows the extraction of positive ions from ~ 43.0 ± 0.2%[‡] of the cell, discriminating against those produced near the walls and apertures. This provides a base extraction efficiency which must be modified to account for the initial kinetic energy of the ion. Generally, ions produced from non-dissociative events possess only thermal velocities (which requisites no modification of the extraction efficiency) whereas those produced by dissociative events may possess energies of up to ~ 10 eV. The effect of initial kinetic energy on ion extraction efficiency is displayed in Figure 2.9.

The PMT allows the detection of de-excitation photons from atomic or molecular processes. Figure 2.6 shows the variation of photocathode quantum efficiency ε_{PMT} with wavelength. This may be adjusted by inserting a 3 mm thick borosilicate glass disk (mounted on an extension arm) in front of the PMT. This reduces the sensitivity range to approximately 280–600 nm (the variation of transmission of the disk is also shown in Figure 2.6). Doing so enables a background to be removed regardless of which range (200–280 nm or 280–600 nm) the photon of interest lies in. The transmission of borosilicate is not a step function at 280 nm however, so the process of separating signal from background can be more involved (see Section 4.2.1).

2.2 Normalization techniques

2.2.1 Determination of efficiencies

In order to set an absolute scale on measurements taken, various characteristics of the system must be quantified. Table 2.1 summarizes the various efficiencies and premultipliers determined; where appropriate, the target gas used is mentioned. The following text discusses how these quantities were measured.

i. ε_+. The absolute positron detection efficiency was established using a γ-ray–e^+ coincidence measurement simultaneously to the recording of the γ-ray counts. In order for the γ-ray and e^+ pulses to be as closely correlated as possible, the CsI γ-ray detector was placed directly above the CEM cone, as shown in Figure 2.10. This allows the detection efficiency

[‡] This has a slight ion mass dependence, lighter ions being less efficiently extracted. This mainly arises as a result of the magnetic field which affects the trajectories of light ions. This effect is negligible above a mass-to-charge ratio of ~ 10 amu q_e^{-1}.

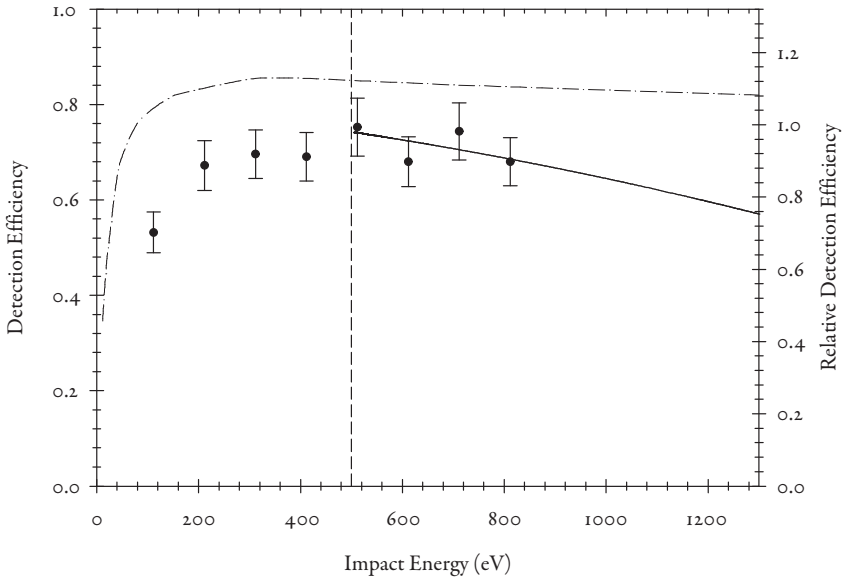

Fig. 2.7: Detection efficiency of the positron detector. Shown are absolute measurements (•) taken using γ-ray–e^+ coincidences; relative measurements taken by varying V_m and cone voltage (continuous curve); the detection efficiency for electrons (chain curve) as supplied by the manufacturers (Dr. Sjuts Optotechnik GmbH); and the impact energy corresponding to V_m = 0 V (dashed vertical line).

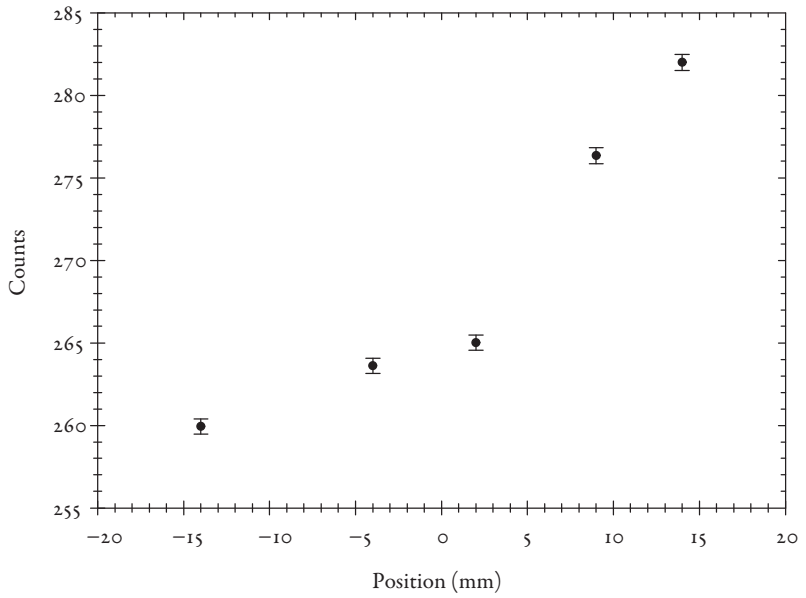

Fig. 2.8: Variation of γ-ray counts with position of annihilation plate relative to gas-cell center.

Fig. 2.9: SIMION simulations of N_2^+ ion extraction from the gas-cell. Left: initial kinetic energy approximately thermal (~0.04 eV); right: initial kinetic energy of 2 eV.

Tab. 2.1: Summary of all the efficiencies used for normalization.

Quantity	Value	±Error	Notes
ε_+	0.7	10%	Positron detection efficiency. Energy dependent—see Figure 2.7.
t_g	0.8	—	Transmission coefficient of each tungsten grid between the gas-cell and the CEM (Williams, 2009).
ε_{ext}	0.43	5%	Thermal ion extraction efficiency (for Ar^+). Error based on simulation of 1000 ions.
ε^F_{ext}	0.6	5%	Correction for extraction efficiency when ionic fragments have non-thermal energy distribution (typical value shown).
ε_{det}	0.56	—	Ar^+ ion detection efficiency (Krems *et al.*, 2005).
ε_{CsI}	0.0077	0.0012	Combined CsI solid angle and detection efficiency.
ε_{PMT}	0.27	10%	Quantum efficiency of the photocathode in the PMT. This is the mean value for the wavelength range of $A\,^2\Pi_u \rightarrow X\,^2\Pi_g$ transition in CO_2 (293–450 nm) (supplied by ET Enterprises Ltd.).
$\Delta\Omega$	0.0160	0.0009	PMT solid angle.
C_r	9.15	0.13	Reflectivity correction (enhancement of $\Delta\Omega$ of PMT by contribution from reflective surfaces). Note: this changes with wavelength—this value is for ~350 nm photons.
ε_c	1.0–0.2	—	Coincidence system efficiency—proportion of input pulses that hit live window in TAC.

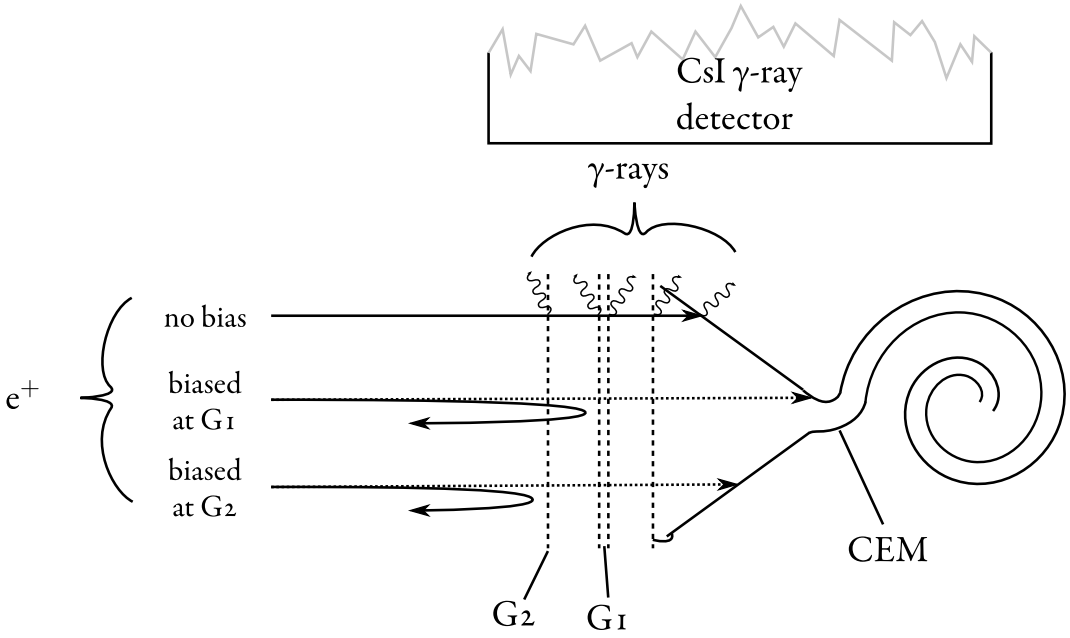

Fig. 2.10: Detector arrangement for measuring ε_+. Solid arrows represent slow positrons, dotted ones fast. Each grid is a potential source of γ-rays from both slow and fast positrons, so more than one biasing position must be considered.

to be calculated thus:

$$\varepsilon_+ = \frac{Y_c}{Y_\gamma} \tag{2.12}$$

where Y refers to counts arising from slow positrons per unit time measured singly (Y_γ) or in coincidence (Y_c). Care was taken to ensure the contribution of γ-rays from sources other than the cone was measured and removed correctly. The assumption is made that the grids are identical, so, as can be seen in Figure 2.10, biasing at G1 allows the contribution from two grids (for slow positrons) and from all grids, and the cone (for fast positrons) to be measured. Biasing at G2 allows only those contributions from fast positrons to be measured.[§] Hence, the yield of γ-rays from slow positrons impacting on the CEM cone may be written as:

$$Y_\gamma = Y_{\gamma,on} + Y_{\gamma,off(2)} - 2Y_{\gamma,off(1)}. \tag{2.13}$$

[§] Actually, each grid contributes less than the one before it by a factor of t_g, the grid transmission. This means the method over-subtracts the slow positron background by approximately 16.5%.

The same argument applies to the coincidence yield, therefore

$$Y_c = Y_{c,on} + Y_{c,off(2)} - 2Y_{c,off(1)}. \tag{2.14}$$

In each case, subscripts *on* and *off* refer to the biasing of the beam and (1) and (2) to the grid at which the beam was biased (see Figure 2.5). This procedure was performed at various *impact* energies of the positron, that is, by maintaining the beam energy at a fixed value and varying the cone voltage. It was found that over the energy range normally considered in the studies, the detection efficiency is substantially invariant, decreasing only at the highest impact energies (see Figure 2.7).

ii. ε_{ext}, ε_{ext}^{F} & ε_{det} (ε_i). Ion extraction efficiencies for thermal and non-thermal ions were calculated using SIMION 8.0 simulations of ions moving in the gas-cell. Two typical extraction patterns are shown in Figure 2.9 for thermal (0.04 eV) and non-thermal (here at 2 eV) energies. As can be seen, with such a low extraction field present where the ions are created (approximately 2 V cm^{-1}), even a small initial kinetic energy has a distinct effect on the extraction trajectories, and consequently, the extraction efficiency. The energy distribution of the ionic fragments of CO_2 as measured by Velotta *et al.* (1994) and N_2 by Van Brunt &Kieffer (1975) for electron impact were used to adjust the value of the extraction efficiency (which is mass independent in this mass range) for application to the more energetic products of dissociation. Detection efficiencies for various mass/velocity combinations were obtained from Krems *et al.* (2005). Where the exact atom/molecule has not been used, a reasonable substitution has been made (e.g. Ar for CO_2) based on similarity of mass. Mass similarity is important not only to ensure similar extraction efficiency (which can be corrected for) but also so that gas densities may be as close as possible directly comparable (or even pressures—pumping speeds of gases are dependent on atomic/molecular mass). The combination of extraction and detection efficiencies is referred to as ε_i hereafter.

iii. ε_{CsI}. The combined detection efficiency of and solid angle subtended by the CsI detector was measured using an annihilation plate mounted on a manipulator arm. This was positioned in the centre of the cell, in the path of the beam, so that annihilation quanta were produced in the same position as those from a target gas. The plate could be moved over the extent of the cell from which most ions are extracted. For a known positron flux,

the γ-ray counts were recorded at various positions in the cell (Figure 2.8) and then a mean value of γ-rays per positron was calculated. The positron count in this case had to be corrected for the transmission of any grids between the gas-cell and CEM (of which there are 4 at 80% transmission each) and for the detection efficiency ε_+.

iv. $\Delta\Omega$. For measurements involving the detection of photons, the properties of the photomultiplier must be considered. The solid angle of the detector was calculated according to the small angle approximation:

$$\Delta\Omega \approx \pi \left(\frac{d}{2D} \right)^2 \tag{2.15}$$

by considering the active area of the photocathode (of diameter d) and the distance from the interaction region to the photocathode (D).

v. C_r. An enhancement (denoted C_r) to the collection efficiency is provided by the polished aluminium from which the gas cell is constructed, and by the Al+MgF_2 coated glass light guides which line the PMT extension arm. This enhancement was measured by recording photon–ion coincidences at a fixed energy (80 eV) in CO_2, then repeating the measurement with the light guides removed and all internal surfaces (i.e. the gas-cell interior and the PMT extension arm) painted black with graphite. The ratio of the corresponding yields provides the enhancement factor caused by these reflective surfaces.

vi. ε_{PMT}. The absolute quantum efficiency of the photocathode was made available by the manufacturer, ET Enterprises Ltd (see Figure 2.6).

vii. ε_c. For coincidence measurements, the live time of the time-to-amplitude converter (TAC) may sometimes have to be considered as an additional efficiency. The system operates by receiving a start pulse and then waiting a period of time, up to a maximum equal to the range of the TAC, for a stop pulse. Irrespective of the receipt of a stop signal, there is then a reset cycle of fixed length. During this whole period, the system is 'dead' to additional start pulses, so any that arrive will be ignored. On high start rate measurements with long TAC time ranges, for example e^+–ion coincidences, this dead time can significantly affect the duty cycle. Only the combination of high start rate and long time range leads to a significant effect however. The MCA itself has a dead time per event of ~ 15 μs, but the

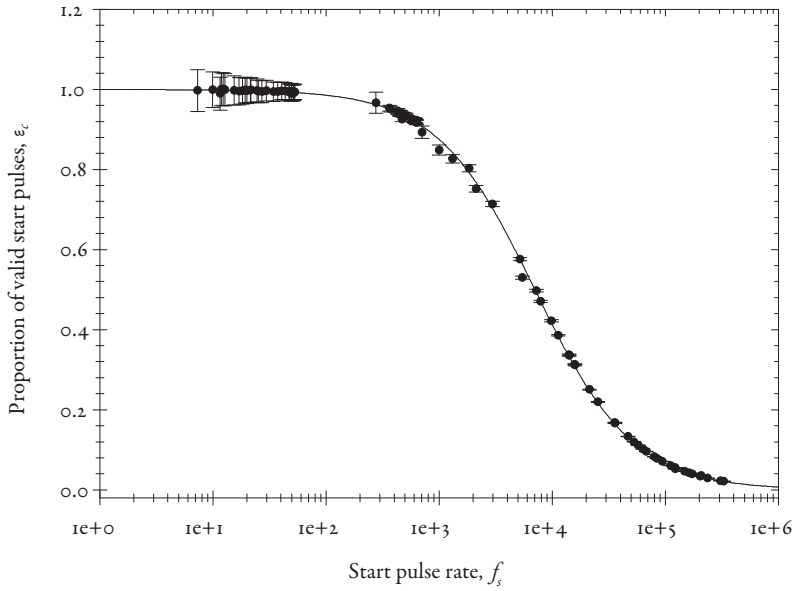

Fig. 2.11: Measured coincidence efficiency ε_c for TAC range $T_{\text{TAC}} = 100$ μs as a function of start count rate (•) with a hyperbolic decay curve fit (continuous curve).

input rate of the MCA depends on the conversion rate of the TAC, so this dead time will almost always be insignificant.¶

The coincidence system efficiency ε_c was determined empirically for a 100 μs TAC range (see Figure 2.11) and, defined as the ratio of true start rate (f_{ts}) to applied start rate (f_s), can be described in terms of the start pulse rate by equation 2.16.

$$\varepsilon_c = \frac{7024.9}{7028.4 + f_s} \tag{2.16}$$

It can be shown to be of this form by considering the fractional dead time of the system, F_{dt}, in terms of the waiting time of the TAC T_{TAC} (the sum of the ramping time and reset period), f_{ts} and f_s:

$$F_{dt} = f_{ts} T_{\text{TAC}} \tag{2.17}$$

¶ The reset cycle of the TAC depends on the time range; for 100 μs, which most measurements employ, this time period is longer than the MCA rest cycle.

The quantity f_{ts} is itself dependent on the time available for starting the TAC, i.e.,

$$f_{ts} = (1 - F_{dt}) f_s. \tag{2.18}$$

When equation 2.17 is substituted in 2.18, it can easily be shown that:

$$\frac{f_{ts}}{f_s} = \frac{(T_{\text{TAC}})^{-1}}{(T_{\text{TAC}})^{-1} + f_s} \tag{2.19}$$

This is the definition of ε_c, and is of the form of equation 2.16. Note that the empirically determined values for T_{TAC} using the quantities from either the numerator or denominator imply $T_{\text{TAC}} = 142.3 \pm 0.05$ μs. This is consistent with the measurement of this quantity using an oscilloscope (though in slight disagreement with figures quoted in the manual for this device—150 μs).

In addition to the various efficiencies, characteristics of the gas cell are required. These can be expressed as the product $n\ell_{eff}$, which is the areal number density in the cell (n being the gas number density and ℓ_{eff} the path length of a e^+). In practice, these are never determined explicitly but are indirectly included in the normalization method. This is the subject of the following section.

2.2.2 General normalization method

Each measurement consists of recording the number of one or more final state product(s) (e.g. ions) and coincidences among them. This is done at a given pressure and for a fixed time period for a number of different beam energies. At each energy the counts are recorded with both the beam on and with the slow portion of the beam biased off, in order that a background contribution be determined. The intensity of the e^+ beam is measured in vacuum, allowing a yield per incident positron to be calculated. Thus, for example, the ion yield per positron (Y_i) may be written as:

$$Y_i = \frac{y_{i,on} - y_{i,off}}{y_{e,on} - y_{e,off}} \tag{2.20}$$

where y refers to the number of counts per second of ions (i) or positrons (e) and *on* and *off* to the state of the beam. This quantity is proportional to the total ionization cross-section,

Q_i^t, according to:

$$Q_i^t = \frac{1}{n\ell_{eff}} \frac{t_g^4 \varepsilon_+}{\varepsilon_i} Y_i \tag{2.21a}$$

$$= kY_i \tag{2.21b}$$

where the symbols are defined as in Table 2.1 (ε_i being the product $\varepsilon_{det} \times \varepsilon_{ext}$). Note that the beam intensity measured at the CEM is reduced by a factor of t_g^4 by transmission through the grids G1, G2 and that over the CEM cone.

For coincidence measurements, the normalization process is substantially identical, with Y_i in equation 2.21a replaced by a coincidence yield Y_c specific to each final state and each detector contributing its own additional efficiency (and other relevant quantities e.g. solid angle). For high start-rate measurements, the inclusion of the coincidence efficiency ε_c is necessary; this approaches unity for low start-rates (see Figure 2.11). Special consideration must be given to coincidence measurements which derive their start pulse from the positron CEM. For such measurements, the beam detection efficiency is cancelled from the equation, meaning that only the multiplier arising from detection of the other product remains.

A general expression for normalization of a yield to a cross-section Q_c may be written as follows:

$$Q_c = \frac{1}{n\ell_{eff}} t_g^4 \varepsilon_+ \prod_x \frac{1}{\varepsilon_x} Y_c \tag{2.22}$$

2.2.3 Practical normalization

In reality, this full explicit normalization is rarely performed. There are a number of methods which allow the normalization constant (hereafter k, as in equation 2.21a, for brevity) to be determined with varying degrees of implicitness; these may be summarised as follows:

1. Normalizing to known electron cross-sections;
2. Normalizing concurrent measurements of positron impact cross-sections to established results and applying relevant corrections to obtain a value for k;
3. Normalizing concurrent measurements of electron impact cross-sections to established results and correcting (as above);

4. Determination of each term of k explicitly (where possible), combined with any of the above.

Using method 1, the assumption is made that the Born approximation applies at high (> 600 eV) energies, that is, the sign of the charge of the incidence particle becomes immaterial and the cross-sections therefore merge, the implication being that positronium formation is negligible (Moores, 2001).‖ This approximation is valid for positron impact on atomic targets (e.g. noble gases—see Section 1.3), but insufficient evidence existed prior to this work to demonstrate its applicability (or otherwise) to molecular targets. Method 1 has been employed in studies of atomic and molecular targets for example, to extract Q_{Ps} for CO_2 (Murtagh *et al.*, 2006) and various ionization cross-sections for CO_2 and N_2 (e.g. Bluhme *et al.*, 1998, 1999a). In this method, k is calculated by fitting (Van Reeth *et al.*, 2002) to the corresponding electron data and therefore includes all premultipliers.

Method 2 involves measuring Q_i^t for positron impact on a target gas for which the total ionization cross-section is well known, that is, good agreement in shape and magnitude exists between several independent measurements (e.g. Ar from Laricchia *et al.* (2002); Marler *et al.* (2005)). As the ion extraction efficiency and $\left(n\ell_{eff}\right)$ have slight mass dependence, a normalization gas must be chosen with a similar atomic mass to the target gas. The base value of k is obtained by least-squares fitting the measured points to Q_i^t from the literature. A correction for the possible differences in pressure between the two measurements (and hence a different value for n) must also be made as appropriate:

$$Q_i^t = k\frac{P_{Ar}}{P_{target}}Y_i. \tag{2.23}$$

The gas pressures used are sufficiently low that interactions between the molecules can be ignored (the gases behave ideally), therefore the pressures are directly comparable.** A measurement of Q_i^t for Ar from which a value of k may be extracted is shown in Figure 2.12 compared to the measurement of Laricchia *et al.* (2002), and a comparison of the results obtained using methods 1 and 2 is shown in Figure 2.13. As can be seen, these two methods yield very similar results. Note that measuring 'known' cross-sections is also a useful system diagnostic.

‖ As the capture process does not happen for electron impact, the lack of dependence on the sign of the projectile charge in the Born approximation implies that capture is non-existent for positive projectiles as well.

** The pressure is measured on a capacitance manometer, which provide sufficiently gas-independent measurements for this purpose.

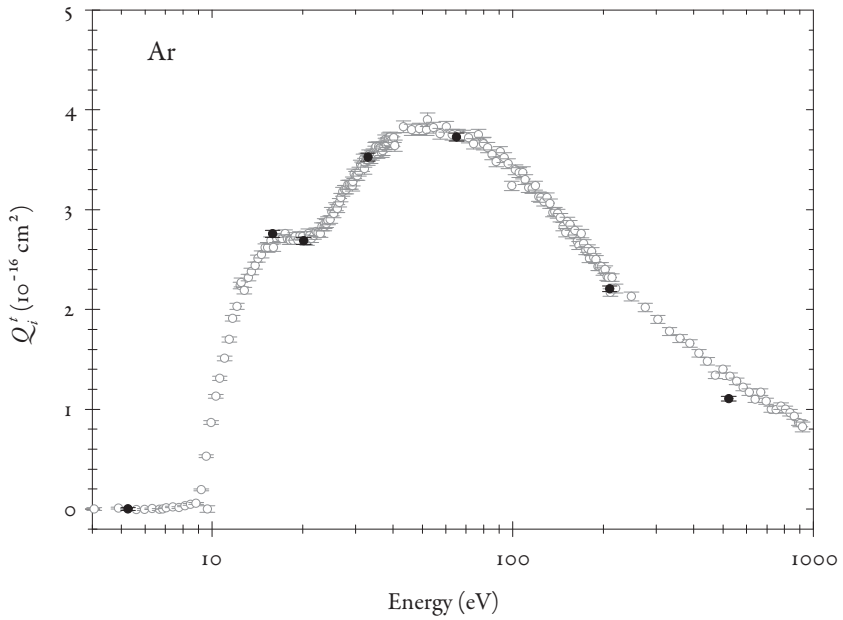

Fig. 2.12: Measurement of Q_i^t for Ar from which the normalization constant used in method 2 was obtained (•), normalized to Laricchia *et al.* (2002) (○).

Method 3 is similar to method 2 except instead of changing target gas, the projectile is changed. This has the advantage of removing potential ambiguities associated with the differing masses of the gases, but the added complication of re-tuning the system for an electron beam. Conversion between the normalization factors obtained via methods 2 and 3 may be achieved, viz.:

$$\left(\frac{Q_i^t}{Y_i}\right)_{e^+} = \left(\frac{Q_i^t}{Y_i}\right)_{e^-} \frac{\varepsilon_+}{\varepsilon_-} \tag{2.24}$$

but this requires knowledge of the absolute electron detection efficiency of the CEM, ε_-. Unlike ε_+ (see Section 2.2.1), this cannot be measured directly as there is no second detector with which to detect electrons, so this value must be obtained using measurements of cross-sections well known for both electron and positron impact. Again, Ar is a sensible choice of target gas. Figure 2.14 shows a measurement of Q_i^t for electron impact on Ar compared with the result of Rejoub *et al.* (2002) from which a value of $\varepsilon_- = 0.62 \pm 0.06$ was determined (assuming a mean positron detection efficiency of $\overline{\varepsilon_+} = 0.70 \pm 0.07$). Note that the conversion introduces an additional error in comparison to method 2 (from both

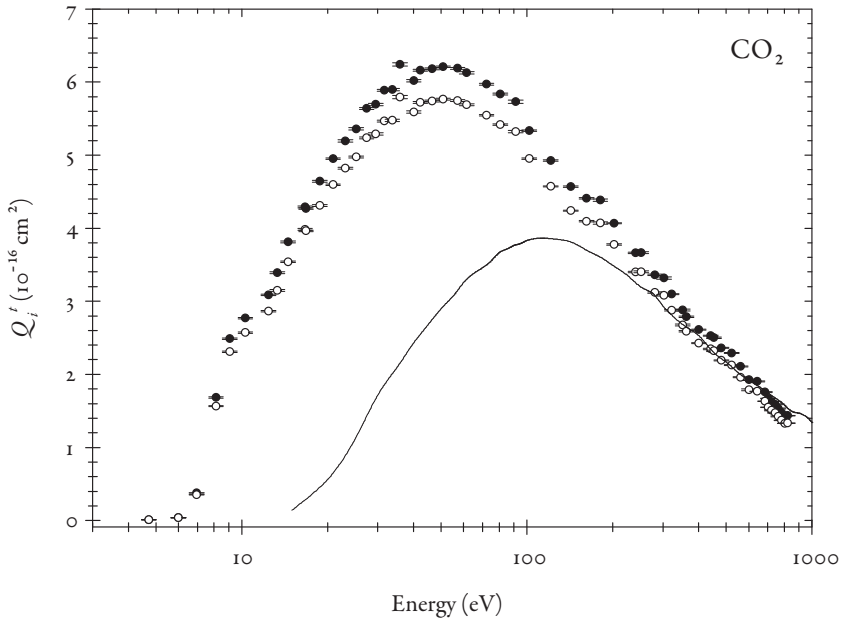

Fig. 2.13: Comparison of two indirect normalization methods (1—● and 2—○) for Q_i^t CO_2. The two results differ at most by 7%. Note the gradients of the cross-sections for the different projectiles do not agree at high energies, casting some doubt over the applicability of the Born approximation, though the agreement level between the two methods serves to moderate this doubt. Electron data (straight line) is from (Straub *et al.*, 1996a).

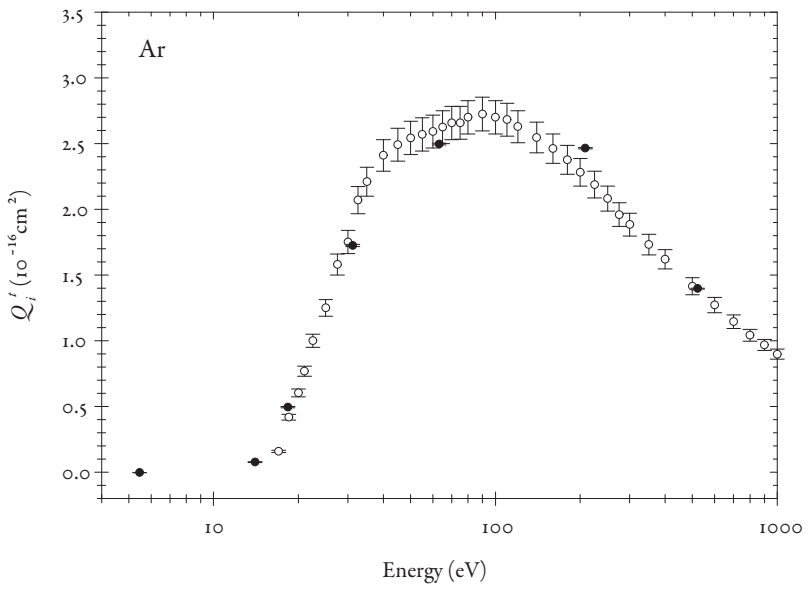

Fig. 2.14: Measurement of electron-impact Q_i^t (•) used for normalization purposes, normalized to Rejoub *et al.* (2002) (○).

ε_+ and ε_-). It was therefore considered that, as these methods are equally valid, method 2 would be used for preference.[††]

Many measurements taken during the course of this work cannot be normalized simply using methods 1–3. This may be because there are few reliable electron cross-section data (or indeed, that the measurement is not possible using electrons e.g. Ps formation), or that there is no precedent in positron impact. In these cases, normalization relies on the capability of the system to record the total ion yield simultaneously to coincidence measurements. Careful characterization of the various efficiencies associated with the system (see Section 2.2.1) allows the coincidence measurements to be normalized to the ion yield, which then may be scaled to any pre-existing cross-sections. Thus, all the measurements have the correct *relative* magnitude.

Table 2.2 summarizes the normalization techniques used during the course of this work. It also highlights the usual approach taken for each particular cross-section. For example, while the normalization of a measurement of simultaneous ionization–excitation (Q_i^{ex}) will rely on establishing Q_i^t; when considering $Q_i^{\mathrm{ex}/+}$, one can reuse the coefficient

[††] Changing gases is also considerably simpler than re-tuning for electrons.

Tab. 2.2: Standardized normalization techniques, showing the full expression and that for practical use for each cross-section category. Note that ε_c is only appreciably different from 1 for coincidence measurements which use detection of a positron as a start signal. This means that, although for the last three cross-sections the value of ε_c is different in each case, it may be safely applied separately to $Q_i^{\mathrm{ex}}/Y_i^{h\nu}$.

Cross-section	Normalization expression	Applied expression
Q_i^t	$\frac{1}{n\ell_{eff}}\frac{t_g^4\varepsilon_+}{\varepsilon_i}Y_i$	—
Q_i^+	$\frac{1}{n\ell_{eff}}\frac{1}{\varepsilon_i\varepsilon_c}Y_i^+$	$\frac{Q_i^t}{Y_i}\frac{1}{t_g^4\varepsilon_+\varepsilon_c}Y_i^+$
Q_{Ps}	$\frac{1}{n\ell_{eff}}\frac{t_g^4\varepsilon_+}{\varepsilon_i\varepsilon_{\mathrm{CsI}}\varepsilon_c}Y_i^\gamma$	$\frac{Q_i^t}{Y_i}\frac{1}{\varepsilon_{\mathrm{CsI}}\varepsilon_c}Y_i^\gamma$
Q_{Ps}^* or Q_i^{ex}	$\frac{1}{n\ell_{eff}}\frac{t_g^4\varepsilon_+ 4\pi}{\varepsilon_i\varepsilon_{\mathrm{PMT}}C_r\Delta\Omega\varepsilon_c}Y_i^{h\nu}$	$\frac{Q_i^t}{Y_i}\frac{4\pi}{\varepsilon_{\mathrm{PMT}}C_r\Delta\Omega\varepsilon_c}Y_i^{h\nu}$
$Q_i^{\mathrm{ex}/+}$	$\frac{1}{n\ell_{eff}}\frac{4\pi}{\varepsilon_{\mathrm{PMT}}C_r\Delta\Omega\varepsilon_c}Y_+^{h\nu}$	$\frac{Q_i^{\mathrm{ex}}}{Y_i^{h\nu}}\frac{\varepsilon_i}{t_g^4\varepsilon_+\varepsilon_c}Y_+^{h\nu}$
$Q_i^{\mathrm{ex}/\mathrm{Ps}}$	$\frac{1}{n\ell_{eff}}\frac{t_g^4\varepsilon_+ 4\pi}{\varepsilon_{\mathrm{CsI}}\varepsilon_{\mathrm{PMT}}C_r\Delta\Omega\varepsilon_c}Y_\gamma^{h\nu}$	$\frac{Q_i^{\mathrm{ex}}}{Y_i^{h\nu}}\frac{\varepsilon_i}{\varepsilon_{\mathrm{CsI}}\varepsilon_c}Y_\gamma^{h\nu}$

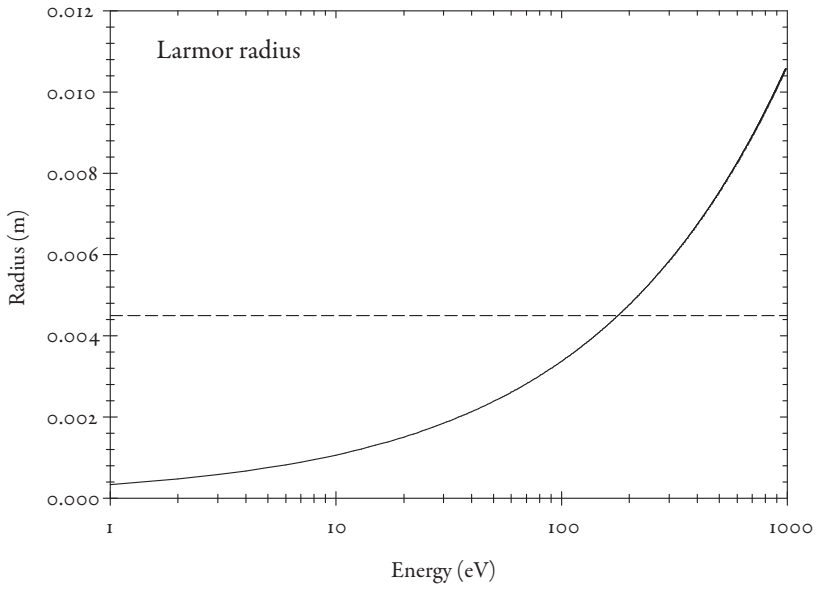

Fig. 2.15: Variation with energy of the Larmor radius of a positron in a 100 G magnetic field. Dashed line shows the radius of the exit aperture.

calculated for Q_i^{ex}.

2.3 Other experimental considerations

2.3.1 Large angle scattering of positrons (including back-scattering)

Though the presence of a magnetic field of approximately 100 G throughout the gas-cell ensures some confinement of the scattered beam, there is a limit to the extent to which large-angle scattered positrons can be collected. This depends on the Larmor radius (r_L) of the positron (and so is energy dependent), given by:

$$r_L = \frac{v_\perp m}{eB} \tag{2.25}$$

where $v_\perp$ is the component of the positron velocity perpendicular to the magnetic field (of strength B), e is the charge and m the mass. Given an ionization event with an energy threshold E_i which deflects the positron with energy E through an angle θ, r_L can be

written:

$$r_L = \frac{\sqrt{2m\,(E - E_i)}\,\sin\theta}{eB}. \tag{2.26}$$

Setting θ to be the largest value it can be for a forward scattered e^+ that is $\theta \to 90°$ and using $E_i = 15$ eV, yields the energy dependence of r_L on $E - E_i$ shown in Figure 2.15. The dashed line represents the radius of the exit aperture, the narrowest hole through which the positron must pass in order to reach the CEM. As can be seen, forward scattered positrons can be entirely contained until an incident energy of approximately 200 eV. Thereafter containment becomes increasingly poor, as positrons scattered to smaller angles can achieve Larmor radii greater than the radius of the exit aperture. However, differential ionization cross-sections become increasingly forward-peaked with increasing collision energy, so the loss of total confinement applies to a correspondingly reduced flux of positrons.

In addition to losing some positrons forward-scattered at large angles, no provision is made to recover those positrons scattered backwards. Without modification of the existing gas-cell, the detection of these positrons is not possible. Measurement of direct ionization cross-sections requires the collection of (ideally) all scattered positrons. However, comparisons of 'known' cross-sections, e.g. Q_i^+ for Ar (Moxom *et al.*, 1996), with the equivalents measured using this system are favourable; certainly possessing the same energy dependence (see, for example, Figure 2.16). This suggests that either the loss of scattered flux is insignificant, or that the cross-section for wide- and back-scattered ionization has the same form as the remainder.

2.3.2 Single-collision regime

In order that coincidence measurements performed on the system represent as accurately as possible only one interaction, the working gas pressure is such that a positron passing through the cell will make, on average, only one collision over the cell length. This pressure is empirically determined for each target gas by measuring beam attenuation at the energy of the peak of the total cross-section; attenuation by more than 10% is not usually accepted. The justification for this is as follows. The Beer–Lambert law may be written as:

$$I = I_0 e^{-\delta x/\lambda} = I_0 e^{-Qn\delta x} \tag{2.27}$$

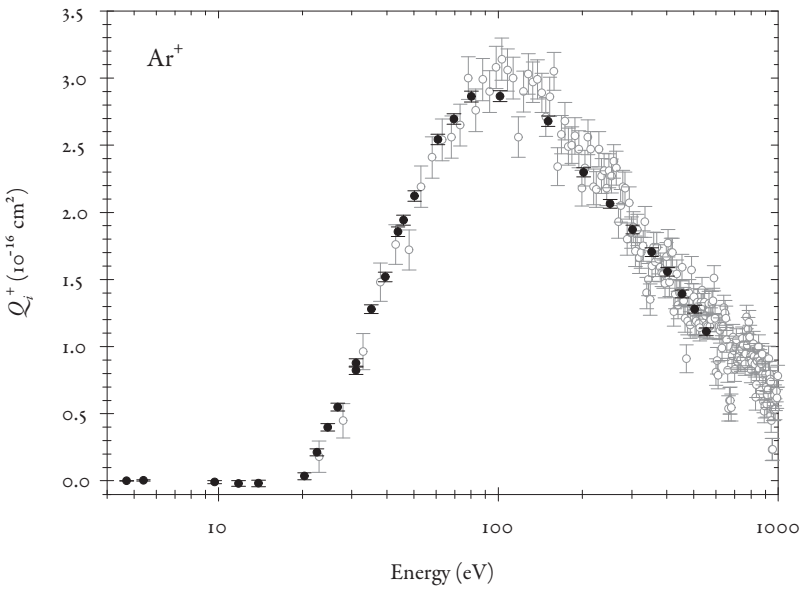

Fig. 2.16: Comparison of present measurement Ar Q_i^+ (•) with that of Moxom *et al.* (1996) (○).

where I_0 and I are incident and transmitted beam intensities, δx is the cell length, λ is the mean free path of the positron, Q is the cross-section and n the number density of the target gas. Setting $\delta x = 0.09$ m and $I/I_0 = 0.9$ reveals that at this attenuation, $\lambda = 0.85$ m, which is large enough to assume an incident positron would collide with only a single atom or molecule (ensuring a linear relationship between pressure and ion yield).[‡‡] Using equation 2.27, one can then calculate a value for n, and therefore for the pressure. The use of low gas pressures also reduces the probability of any ion–neutral collisions occurring. Evidence of this manifests itself in the broadening of TOF spectra to longer times, as such collisions increase the ion time-of-flight.

2.3.3 TAC/MCA timing linearity and mass calibration

In an ideal world, the amplitude response of the time-to-amplitude converter would increase linearly with increasing duration between start and stop pulses. This is important as a linear response allows for calibration of the TAC–MCA system with accurate knowledge of only two points required. One of these points can be t_0, the channel at which start and stop pulses emitted simultaneously are counted, and the other would correspond to

[‡‡] The first order Maclaurin expansion of $e^{-\delta x/\lambda}$ is linear to within 1% using these values.

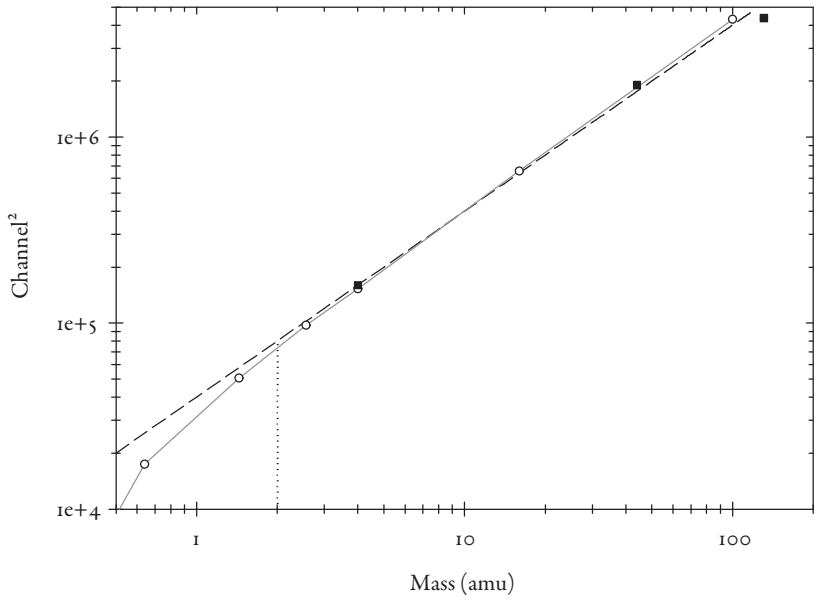

Fig. 2.17: Calibration of the time-to-amplitude converter, showing the positions of He^+, CO_2^+ and Xe^+ (■—heavier targets appear at longer times); points taken using pulses in coincidence with the same pulses delayed (○ with grey continuous curve); a fit to the linear region (continuous curve) and the breakdown of TAC linearity (dotted line). Note that *linearity* refers to the correspondence between channel number and time, not mass.

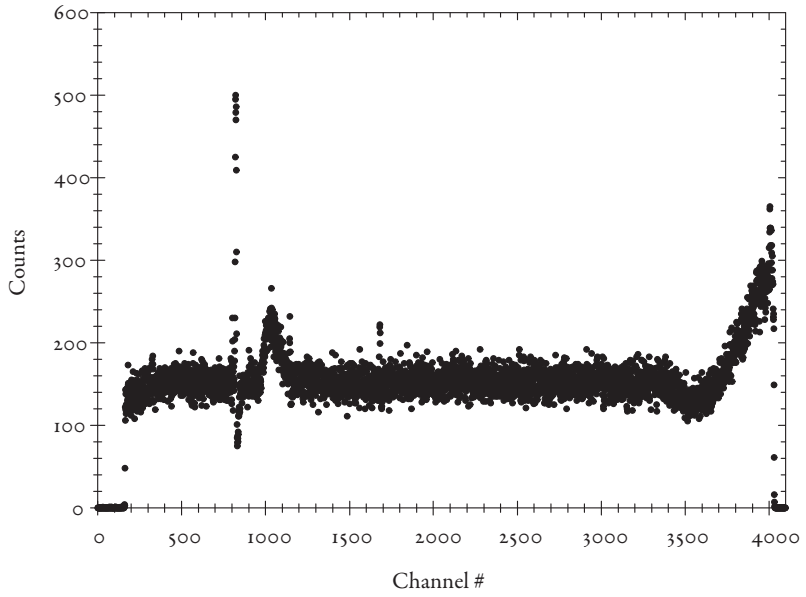

Fig. 2.18: γ-ray–e^+ coincidence spectrum showing the detection of γ-rays from the CEM cone. The noise peak at t_0 (channel 822) is present regardless of the origin of the stop pulse (which passes through the CsI detector electronics).

the arrival of an atomic (so that no fragments are produced) ion, created below the double ionization threshold. The linearity of response has been established using a pulse source and a variable delay, and is shown on Figure 2.17.

2.3.4 *γ-ray–e^+ coincidences*

Using γ-ray based coincidences to determine Ps formation cross-sections (including those involving excitation) assumes that any *correlated* γ-ray detected arises from the decay of Ps in the gas-cell. There are other sources of γ-rays, for example, annihilation without the capture process, those emitted by the ^{22}Na source, those from beamline wall annihilation, and γ-rays from the collision of a positron with the CEM cone. Of these, the first is considered negligible for atomic targets in the energy range considered (Van Reeth *et al.*, 2005); the second would present an extremely low solid angle to the detector and the third contributes only uncorrelated γ-rays. Only the last of these sources can potentially provide a correlated signal when a positron involved in a direct ionization event is detected by the CEM and the resultant γ-ray from the cone detected by the CsI. A measurement of γ-

ray–e^+ coincidences is shown in Figure 2.18 shows a peak centered on approximately the 1010th channel, corresponding to this occurrence. The rate of γ-ray–e^+ coincidences per positron is $(4.90 \pm 0.16) \times 10^{-5}$, which can be transformed into a fractional contribution to Ps formation by multiplying by the direct ionization cross-section. This has been calculated for N_2 and found to be of the order of 0.1%, and so is considered negligible. Also visible is a sharp peak at the 822nd channel, present even in uncorrelatable signals (e.g. e^+–pulser coincidences). This is noise and may be disregarded.

2.3.5 *Vacuum contaminants*

The residual gases present in the vacuum system are atmospheric gases and substances outgassing from adsorption onto internal surfaces. If experimental conditions have been maintained for several weeks (not uncommon) then the only significant component is H_2O (the rubber seals prevent baking of the system to expedite outgassing). However, its presence is only detectable at a rate of < 1 ion s^{-1}, contributing $< 1\%$ to typical e^+–ion measurements. It has not been observed in any other coincidence measurements performed in vacuum (or otherwise), and so can generally be neglected. The use of Santovac® 5 diffusion pump oil provides superior vacuum conditions, given the non-UHV nature of the system.

The system as a whole is well-suited to measuring ionization cross-sections. It has a high ion collection efficiency albeit at the expense of timing resolution, meaning the mass sensitivity is lower than that of, for example, a crossed beam and gas jet set-up, but this allows measurements to be taken on short timescales. The ability to record several coincidences simultaneously, and thus determine several different cross-sections simultaneously, not only increases the rate at which data can be taken, but also ensures consistency between measurements, eliminating the possibility that fluctuations in e.g. gas pressure or e^+ beam intensity could affect normalization of measurements for different processes.

3. EXCITED-STATE POSITRONIUM FORMATION FROM XENON

3.1 Introduction

As part of the work of Murtagh *et al.* (2009), who examined excited-state positronium formation from gaseous targets, this study measured the cross-section for the process in xenon. Though this study forms part of the first *experimental* determination of the cross-section for formation of Ps into an excited state (Q^*_{Ps}) (Murtagh *et al.*, 2009), there are several theoretical calculations for H (Basu &Ghosh, 1988; Hewitt *et al.*, 1990; Kernoghan *et al.*, 1996), He (Khan *et al.*, 1985; Hewitt *et al.*, 1992; Sarkar *et al.*, 1992; Campbell *et al.*, 1998; Chaudhuri &Adhikari, 1998; Utamuratov *et al.*, 2010) and the noble gases (Gilmore *et al.*, 2004). The current measurements allow such theories to be tested. In addition to this motivation, it had been suggested that structure visible in Q_{Ps} for the noble gases (see Figures 1.5–1.15) may arise from excited-state Ps formation (Laricchia *et al.*, 2002). Acting on this hypothesis, upper and lower limits for Q^*_{Ps} were estimated using the method described in section 1.3.3. These measurements allow the plausibility of such limits to be examined.

Excited-state Ps was first observed in 1975 (Canter *et al.*) using Lyman-α–γ-ray coincidence measurements of slow positrons impinging on a Ge target. Using a narrow (2 nm) filter peaked at 243 nm, it was possible to uniquely identify the $2P \rightarrow 1S$ transition. It was first observed from a gaseous target (Ne, Ar and H_2) in 1985 (Laricchia *et al.*), also using Lyman-α–γ-ray coincidences.

The energy level structure of Ps is shown in Figure 3.1 (up to $n = 4$). Ps has an energy level structure very similar to that of H but with the energy levels themselves halved as a result of the low mass of the positron compared with that of the proton. Correspondingly, the wavelengths of transitions are doubled. The transitions significant to this study are the $2P \rightarrow 1S$ transitions; a discussion of the impact of higher n states is in the following

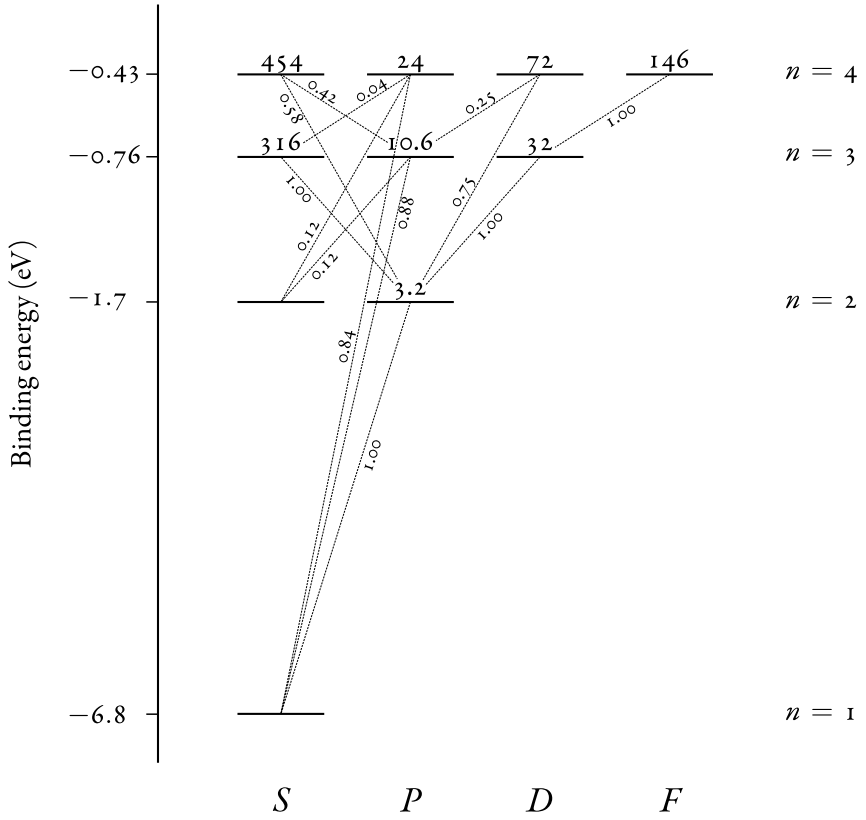

Fig. 3.1: Energy level structure of Ps showing the lifetimes against de-excitation of states up to $n = 4$ and the branching ratios for de-excitation of each state (adapted from Bozek *et al.*, 2006, for H).

section. Note that the $2S \rightarrow 1S$ transitions are dipole forbidden and so $2S$ states, in the absence of perturbation, have extremely long single photon de-excitation lifetimes* and are hence very unlikely to be detected in this study. By contrast, the $2P$ states have much longer lifetimes against annihilation than de-excitation as the wavefunction is nodal at the origin. This means that detection efficiency of $2P$ states is unlikely to be affected by annihilation preceding de-excitation.

* The two photon decay mode is 'unobservably rare' (Berko &Pendleton, 1980), while the equivalent single-photon decay for atomic hydrogen has an unperturbed lifetime of approximately 4.6 days (Solovyev *et al.*, 2010)

3.2 Experimental method

The experimental set-up was used as described in Chapter 2 without modification. For measurement of excited-state Ps formation, the coincidence between the Lyman-α photon and resultant ion was used. Photons of wavelength 243 nm are detected by the PMT with a quantum efficiency of $\varepsilon_{\mathrm{PMT}} = 0.20 \pm 0.02$ and reflected from the polished aluminium surfaces with a coefficient of reflection of $C_r = 2.40 \pm 0.22$. A background can be measured and subtracted by inserting the borosilicate glass filter which completely blocks 243 nm photons. This reduces the effective range of the PMT to 200–280 nm; it is then assumed that in this range only the Lyman-α emission is significant. This can be justified as follows. All but the Lyman series possess wavelengths longer than 600 nm, well outside the wavelength range considered. Therefore, the other series may be ignored unless de-excitation occurs as a cascade via the $2P$ state. In the Lyman series, lines above α are detected with decreasing efficiency as the transmission of the quartz window of the PMT falls off rapidly below 200 nm (ultimately becoming opaque at 160 nm)—β has a wavelength of 206 nm, γ of 195 nm. In addition to this, the higher n states are expected to be formed with decreasing probability according to the scaling law (Guha &Saha, 1980):

$$Q_{\mathrm{Ps}}(n) = Q_{\mathrm{Ps}}(n = 1) \sum \frac{1}{n^3}. \tag{3.1}$$

This predicts that the proportion of Ps formed in an $n = 3$ state is 29.6% (8/27) of that formed in $n = 2$. On average only 1/3 of this will be in the $3P$ state, of which 88% will de-excite directly to $1S$ (Bozek *et al.*, 2006), leading to at most an 8.7% contribution from this state (given sufficient time for de-excitation). It can be seen from this that contributions from n states higher than $n = 3$ are negligible.

Apart from direct detection, there are a number of ways in which other states may be observed. The mechanisms for this fall into two categories: collisional de-excitation and Stark mixing of states.

3.2.1 Collisional de-excitation

All Ps formed in the gas-cell has a probability of colliding with another atom before annihilation which depends on the density of the target gas and the total cross-section for

interaction. The mean time between collisions t_c is given by:

$$t_c = \left(\rho n^4 Q_t \sqrt{\frac{E}{m_e}}\right)^{-1} \tag{3.2}$$

where ρ is the number density (typically $\sim 5 \times 10^{19}\,\mathrm{m}^{-3}$), $n^4 Q_t$ is the Bohr-scaled total cross-section† of (Armitage *et al.*, 2006) and $\sqrt{E/m_e}$ is the velocity of the Ps atom. The value of t_c is small compared to the lifetimes against de-excitation (t_d) of the $n = 3$ states (316 ns, 10.6 ns and 32 ns for the $3S$, $3P$ and $3D$ states respectively). As described in the previous section, states above $n = 3$ may be regarded as having insignificant formation probabilities, however, for the $3P$ and $3D$ states the probability of de-excitation before a collision can be calculated using:

$$P(d) = 1 - \mathrm{e}^{-\frac{t_c}{t_d}} \tag{3.3}$$

leading to values $< 5\%$ for both states. As this must be weighted by the formation cross-section, transitions from these states may be safely neglected as collisional de-excitation is unlikely to occur: for states with $n > 2$, a collision will result in fragmentation rather than de-excitation, with a probability of ~ 1. This was estimated by Murtagh *et al.* (2009) based on similar calculations and measurements with excited-state H atoms (Bates & Walker, 1966; Edwards & Thomas, 1970). In addition, recent work (Brawley *et al.*, 2008) suggests that even ground state Ps has an approximately 30% chance of fragmenting on collision with a target atom. Hence, the detection of $n > 2$ states relies on de-excitation prior to collision which results in less than 10% of the signal arising from $n > 2$ Ps, averaged over the energy range of the measurement.

For $2S$ Ps, the probability of collisional de-excitation can be estimated from:

$$P(\mathrm{CD}) = \frac{Q_{2S\to 2P}}{n^4 Q_t} \tag{3.4}$$

where $Q_{2S\to 2P}$ has been calculated by Starrett & Walters (2008). This contribution is less than 1% of the total signal.

† This scales the ground-state total cross-section to an excited-state one by using the assumption that the radius r of an atom is proportional to n^2 and Q_t is proportional to r^2, so $Q_t(n) \propto n^4$.

Tab. 3.1: Contributions to Q^*_{Ps} from states other than $2P$

$2S \to 2P$ (S.M.)	$2S \to 2P$ (C.D.)	$n > 2$	Total
$< 1\%$	$< 1\%$	$\sim 2.5\%$	$< 5\%$

3.2.2 Stark mixing

In addition to collisional de-excitation, the $2S$ state of Ps may be detected via the Stark effect—the shifting of energy levels which arises from the influence of an external electric field. There are two sources of Stark mixing in the gas-cell:

1. the electric field from the ion extraction lens; and
2. the relativistic transform of the magnetic field, $\gamma\mathbf{v} \times \mathbf{B}$.

An estimate of the contribution from $2S \to 2P$ has been made by considering the various competing processes which can occur. The probability of detecting a transition depends on the rate of Ps loss from the gas cell (f_{cell}), the rate of Ps loss due to annihilation (f_{ann}) and the transition rate of $2S \to 2P$ ($f_{trans.}$), according to equation 3.5.

$$P(\text{trans.}) = 1 - e^{-\frac{f_{trans.}}{f_{cell}+f_{ann}}} \tag{3.5}$$

The transition rate is energy dependent as it relies on the Stark effect. As the energy of the Ps increases, its ability to reach regions of higher electric field in the cell increases which in turn increases the Stark mixing and correspondingly the transition rate. At an energy of 1.2 eV, $f_{trans.} = 1.11 \times 10^7\ \mathrm{s}^{-1}$; at 177 eV this has increased by an order of magnitude.

The estimates of contributions from non-$2P$ states are summarized in Table 3.1. Spontaneous transition between the $2S$ and $2P$ states may be disregarded: the lifetimes against such transitions have been calculated as 1.75×10^5 s, 1.68×10^5 s and 3.46×10^5 s for $2\ ^3S_1$ to $2\ ^3P_0$, $2\ ^3P_1$ and $2\ ^3P_2$, respectively (Burdyuzha &Kauts, 1998). Overall, the measured cross-section is composed of over 95% direct observation of the $2P \to 1S$ transition and shall consequently be referred to as $Q_{\mathrm{Ps}}(2P)$.

In addition to excited-state Ps, consideration must be given to another source of photons: ionization–excitation of the target. Only transitions with photons in the range 200–280

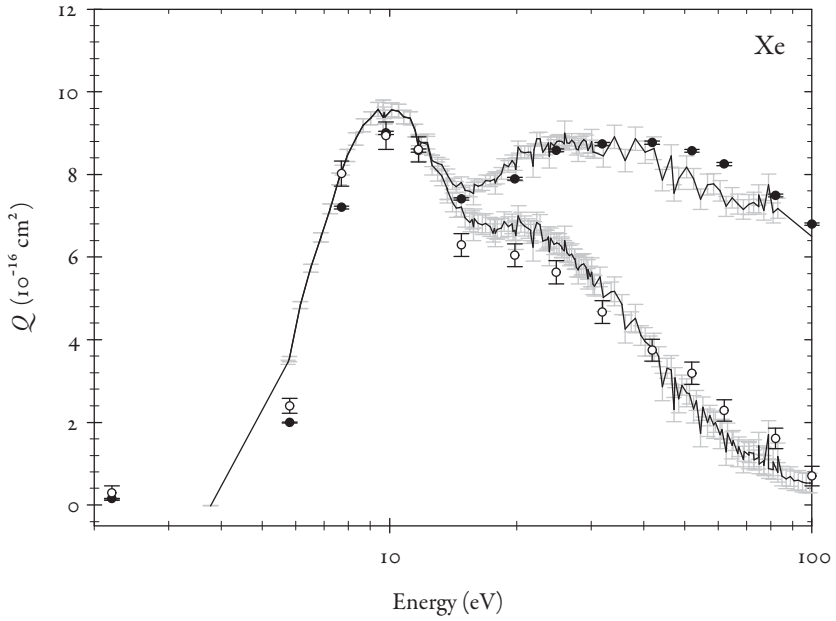

Fig. 3.2: Measurements of Q_i^t (•) and Q_{Ps} (○) taken during this study, compared with the detailed measurements of Laricchia *et al.* (2002) (error bars shown in grey).

nm need be considered, of which there are around 200 (Ralchenko *et al.*, 2010). However, measurements of e^+–photon coincidences revealed no significant signal (zero within errors, on average) over the energy range in consideration. This suggests a very small cross-section for ionization–excitation, though only the direct process can be measured distinctly.[‡]

3.3 Results and Discussion

Figure 3.2 shows the cross-sections measured simultaneously with Q_{Ps} $(2P)$ in this study. These measurements demonstrate good agreement with previous experimental determinations (e.g. Laricchia *et al.*, 2002), reproducing the structures observed in that study. Q_{Ps} was measured using γ-ray–ion coincidences (as with those for CO_2 and N_2—see Chapter 4 and Cooke *et al.* (2010b)). Q_i^t can be seen to peak at ~ 10 eV with a value of ~ 9×10^{-16} cm² and again at ~ 30 eV with a slightly smaller magnitude. The reproducibility of the

[‡] Ps formation simultaneous to ionic excitation is indistinguishable from excited-state Ps formation on this system as both reactions produce ions, photons (of similar wavelengths) and γ-rays. With superior timing resolution it may be possible to identify them by the lifetimes of each state.

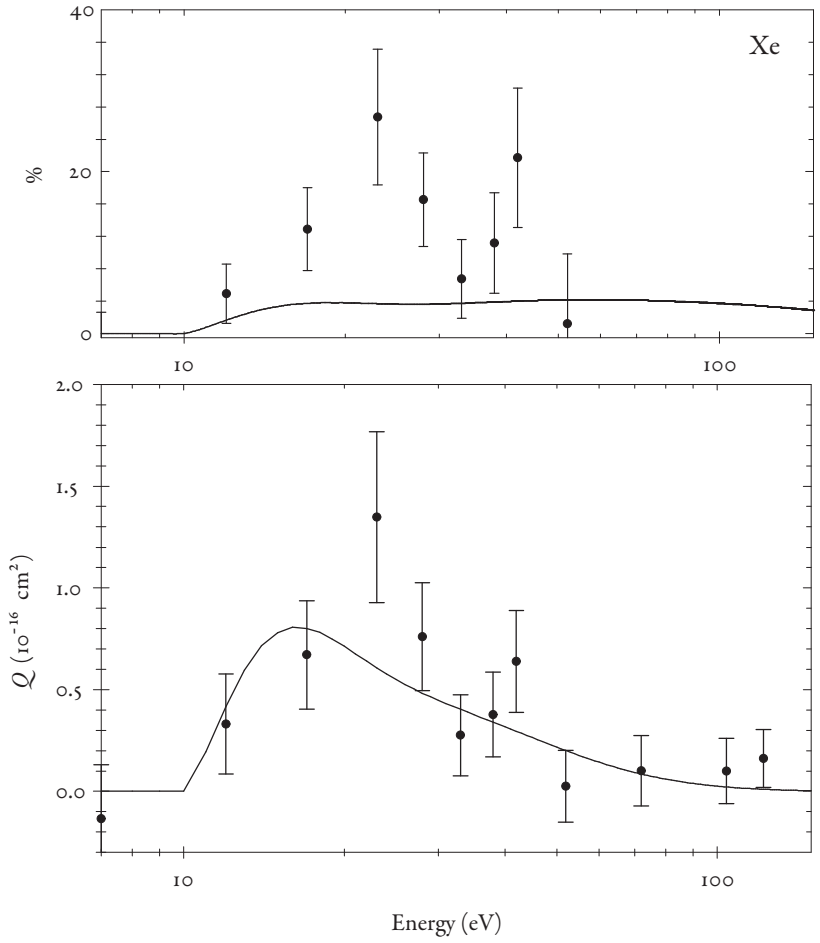

Fig. 3.3: Cross-section for excited-state Ps formation from Xe (•), compared with available theory (Gilmore *et al.*, 2004) (continuous curve). Above: percentage contribution to Q_{Ps} for both experiment and theory (legend as main figure).

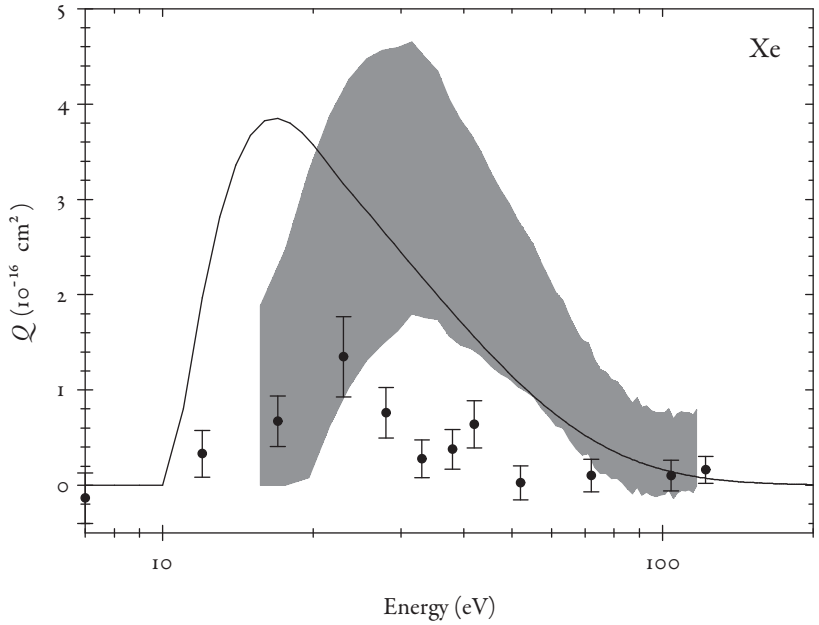

Fig. 3.4: Comparison of the Q_{Ps} ($2P$) from the present study (•) with the upper and lower bounds for excited-state Ps formation (Laricchia *et al.*, 2002) (shaded) and the calculated cross-section $Q_{Ps}(n > 1)$ of Gilmore *et al.* (2004) (continuous curve).

shape of these cross-sections supports the reliability of the normalization technique used to put an absolute scale on $Q_{\mathrm{Ps}}(2P)$ and, indeed, those measurements from Chapter 4.

The first determination of $Q_{\mathrm{Ps}}(2P)$ for Xe is shown in Figure 3.3. It peaks at around 23 eV with a maximum value of 1.3×10^{-16} cm^2, accounting for a quarter of all Ps formed at that energy. As this only accounts for Ps formed in the $2P$ state, this provides some support for the limit estimates of Laricchia *et al.* (2002). A comparison between the present measurements and these deduced limits is shown in Figure 3.4.

Also shown on Figure 3.3 is the theoretical determination of $Q_{\mathrm{Ps}}(2P)$ of Gilmore *et al.* (2004), a distorted-wave Born approximation calculation. Unlike the comparison of $Q_{\mathrm{Ps}}(\text{all } n)$ (see Section 1.3, Figure 1.15) there is good agreement between the magnitudes of theory and experiment. The disparity between the calculations for all n and just $2P$ is highlighted in the upper pane of Figure 3.3 which shows the variation of the ratio $\dfrac{Q_{\mathrm{Ps}}(2P)}{Q_{\mathrm{Ps}}}$ for both experimental and theoretical data sets, the theoretical curve being significantly lower. There is broad agreement in the energy dependence, though there is some disagreement on the peak position.

❧

These measurements demonstrate the importance of excited-state Ps formation to positron-impact ionization in Xe. Considered together with the results for He and Ar (Murtagh *et al.*, 2009, see Figures 3.5–3.6), a trend of increasing Ps($2P$) formation as a function of energy with increasing Z is evident. This can be seen in the behaviour of the fraction $\dfrac{Q_{\mathrm{Ps}}(2P)}{Q_{\mathrm{Ps}}}$ the maximum value of which increases from 0.06 ± 0.01 for He to 0.26 ± 0.09 for Xe. In general, agreement with theory for all three targets is good, though there are some discrepancies in the energy of the peak of the cross section. The agreement in magnitude is something of a surprise, as identical calculations for Ps (all n) exceed experimental determinations by factors of 1.3, 2.0 and 2.8 for He, Ar and Xe, respectively.

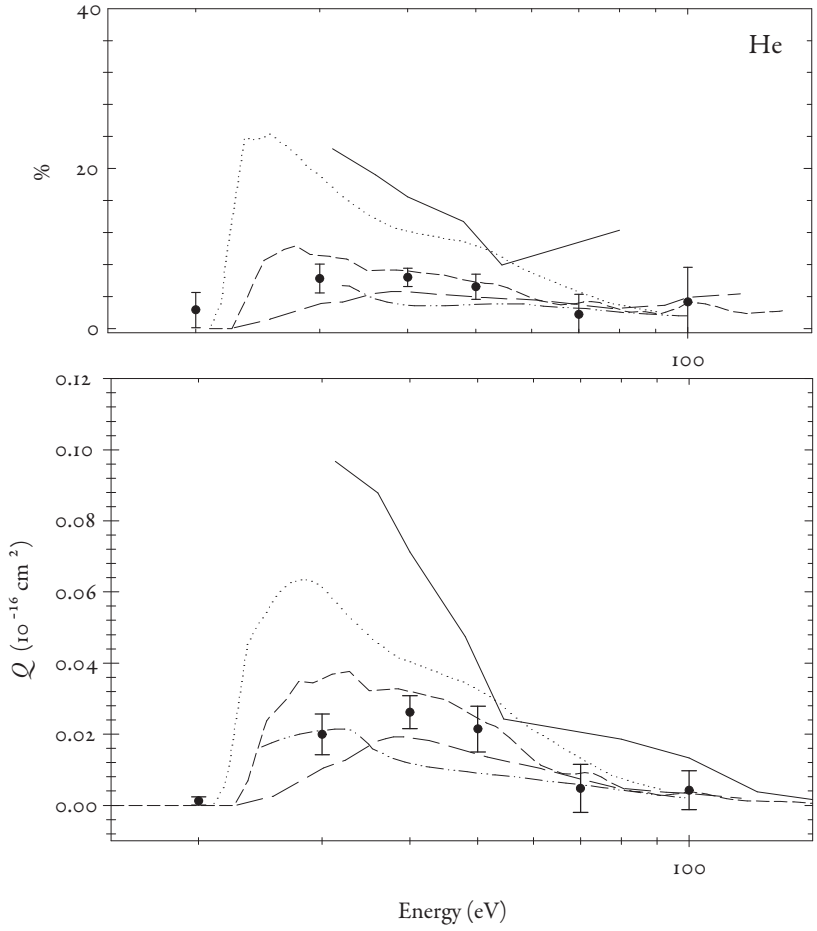

Fig. 3.5: $Q_{\mathrm{Ps}}(2P)$ for He (•) (Murtagh *et al.*, 2009). Also shown are calculations: long dashed line—Utamuratov *et al.* (2010), dotted line—Chaudhuri & Adhikari (1998), dashed line—Campbell *et al.* (1998), solid line—Hewitt *et al.* (1992), chain curve—Khan *et al.* (1985).

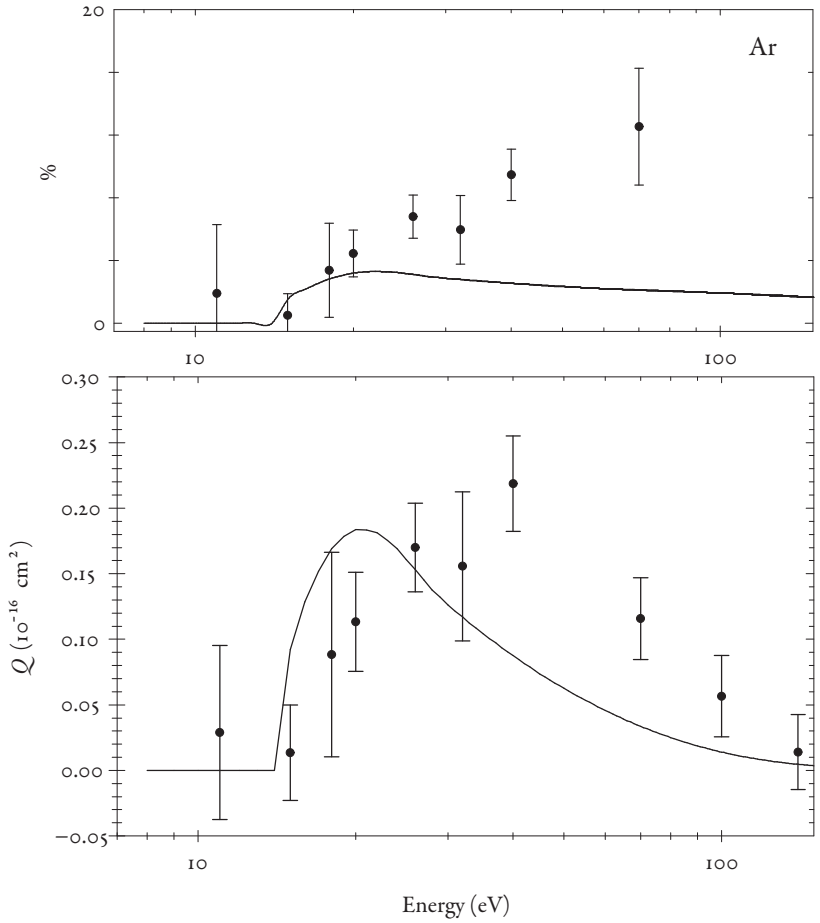

Fig. 3.6: $Q_{\mathrm{Ps}}(2P)$ for Ar (•) (Murtagh *et al.*, 2009). Also shown is the calculation of Gilmore *et al.* (2004).

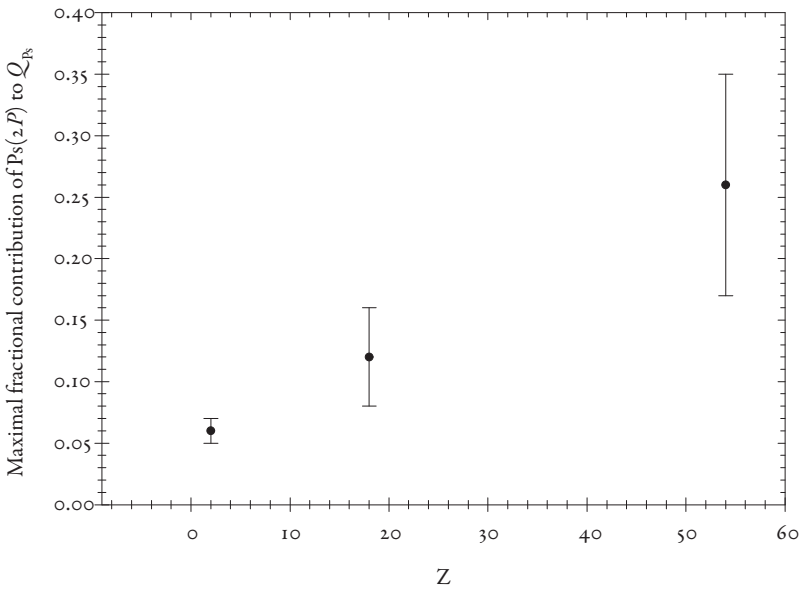

Fig. 3.7: Analysis of the behaviour of excited-state Ps formation with increasing Z.

4. IONIZATION OF CO_2 AND N_2 BY POSITRON IMPACT

4.1 Introduction

IONIZATION and excitation of CO_2 and N_2 have been studied for decades using a variety of projectiles. The reason for this is that both CO_2 and N_2 are important molecules in such diverse fields as biology and planetary science. As basic biological molecules they are among the most fundamental of chemicals for most forms of life on Earth. CO_2 is essential for photosynthesis and is one of the respiration products of all animal life, and N_2 is the largest component of the Earth's atmosphere. As such, they are well-studied molecules, with cross-sections having been measured for electron- (Itikawa, 2002; Itikawa *et al.*, 1986, and references therein), positron- (Hoffman *et al.*, 1982; Bluhme *et al.*, 1998, 1999a; Przybyla *et al.*, 1999; Murtagh *et al.*, 2006; Marler &Surko, 2005), proton- (Birley, 1974; Knudsen *et al.*, 1995; Dimopoulou *et al.*, 2005; Thomas *et al.*, 1967), heavier ion- (Bregman-Reisler &Doering, 1975; Monce, 1988; Doering, 1964) and photon impact (e.g. Brundle &Turner, 1969; Eland, 1972; Judge &Lee, 1973; Cook &Metzger, 1964). A picture has emerged of their responses to the impacts of these various projectiles through such studies, one which it was the aim of this study to add to, by measuring a substantially complete suite of integrated positron-impact cross-sections. A summary of the measured cross-sections is given in Table 4.1.

4.2 Experimental method

The experimental set-up used was again as described in Chapter 2 without modification. The study was performed over a period of approximately 2 years at the beginning of which a new ^{22}Na source of activity 52.6 mCi was installed. This allowed for a maximum beam intensity of $\sim$ 20000 s^{-1} at the beginning of this period, declining to $\sim$ 10000 s^{-1} towards the end. The same moderators were used throughout—4 overlapping 25 μm annealed tungsten meshes—except for the very last set of measurements, for which a set of

Tab. 4.1: Summary of cross-sections investigated during the course of this study. The abbreviation hν is used to refer to a photon.

Cross-section	Symbol	Target	Measurement
Total ionization	Q_i^t	CO_2, N_2	ion
Direct ionization, non-dissociative	Q_i^+	CO_2, N_2	e^+–ion
Direct ionization, dissociative	Q_i^{diss}	CO_2	e^+–ion
Positronium formation	Q_{Ps}	CO_2, N_2	γ-ray–ion
Ionization–excitation	Q_i^{ex}	CO_2, N_2	hν–ion
Ionization–excitation, direct	$Q_i^{\text{ex}/+}$	CO_2, N_2	hν–e^+
Ps formation–excitation	$Q_i^{\text{ex}/\text{Ps}}$	CO_2, N_2	hν–γ-ray
Ionization–excitation, state separated	$Q_i^{\text{ex}/A,B}$	CO_2	hν–ion
Excited-state Ps formation	Q_{Ps}^*	N_2	hν–ion

Tab. 4.2: Visible transitions arranged by target and position of glass filter.

	Glass filter	
Target	In	Out
CO_2	CO_2^+ 0.85 × $A\,^2\Pi_u \rightarrow X\,^2\Pi_g$	$A\,^2\Pi_u \rightarrow X\,^2\Pi_g$
	CO_2^+ 0.22 × $B\,^2\Sigma_u^+ \rightarrow X\,^2\Pi_g$	$B\,^2\Sigma_u^+ \rightarrow X\,^2\Pi_g$
	CO^+ 0.90 × $A\,^2\Pi \rightarrow X\,^2\Sigma^+$	$A\,^2\Pi \rightarrow X\,^2\Sigma^+$
	Ps	$2P \rightarrow 1S$
N_2	0.9 × $B\,^2\Sigma_u^+ \rightarrow X\,^2\Sigma_g^+$	$B\,^2\Sigma_u^+ \rightarrow X\,^2\Sigma_g^+$
	Ps	$2P \rightarrow 1S$

7 overlapping bleach-etched annealed tungsten meshes of thickness 11 μm were installed (Williams, 2009). This allowed a return to count rates of ~ 20000 s^{-1}.

The experimental techniques employed are coincidence measurements as depicted in Figure 2.2, the correspondence between cross-sections measured and particles detected is given in Table 4.1. For the particular case of Q_i^{ex}, the method is almost identical to that used for the measurement of Q_{Ps} $(2P)$. The differences arise as Ps$(2P)$ has a precise de-excitation photon wavelength (243 nm), whereas those from CO_2^{+*} and N_2^{+*} cover a wide range of wavelengths. A summary of visible transitions in each target is shown in Table 4.2, and the method for separating them from each other is described in the following section (4.2.1).

4.2.1 Additional normalization considerations for Q_i^{ex} (CO_2)

In addition to the normalization methods discussed in Section 2.2.2, an extra step in the process must be used to extract the separate contributions from different transitions in CO_2^{+*}. As described in Chapter 3, in order to separate the de-excitation photons by wavelength, the borosilicate glass filter mounted on a manipulator arm was placed between the gas cell and the PMT. This changes the effective wavelength range of the PMT from ~200–600 nm to ~280–600 nm. The $A\ ^2\Pi_u \rightarrow X\ ^2\Pi_g$ transition emits photons in the wavelength range ~293–450 nm, whereas the $B\ ^2\Sigma_u^+ \rightarrow X\ ^2\Pi_g$ photon is at approximately 289 nm. Inserting the glass filter means the $B\ ^2\Sigma_u^+ \rightarrow X\ ^2\Pi_g$ photon is attenuated by a larger factor than the $A\ ^2\Pi_u \rightarrow X\ ^2\Pi_g$ photons. By taking measurements with the glass both in and out (GI and GO respectively, hereafter), the two transitions can be substantially separated by forming two simultaneous equations (equation 4.1—GO, equation 4.2—GI):

$$Y_{GO} = Y_A + Y_B + \sum_N Y_N \tag{4.1}$$

$$Y_{GI} = t_A Y_A + t_B Y_B + \sum_N t_N Y_N \tag{4.2}$$

where $Y_{A,B}$ are contributions arising from the transitions originating from the corresponding initial states; $t_{A,B}$ are the transmission coefficients of these transitions through borosilicate glass and Y_N refers to any additional transitions which may be detected (with transmission coefficient t_N). The largest contributions to Y_N are from the formation of CO^+ in the $A\ ^2\Pi$ state, and of positronium in the $2P$ state (refer to Chapter 3 for further details). The values of t_A and t_B were established to be 0.85 ± 0.05 and 0.22 ± 0.03 respectively by considering the electron-impact de-excitation spectrum (Tsurubuchi & Iwai, 1974) and the transmission curve* of Schott BK7 glass (see Figure 2.6). The spectrum was integrated over the relevant wavelength range to provide an unattenuated intensity, then the same spectrum was weighted by the transmission as a function of wavelength and reintegrated. The ratio of the two provides the transmission coefficients for the transitions when the integration ranges match the wavelength ranges of the transitions. Separating the two transitions both from each other and from the contributions of $\sum Y_N$ is impossible as there are too many variables, however, the remainders, as discussed below, may be surmised to be small. From Furuya *et al.* (2002), the cross-section of electron-impact formation of CO^+ in the

* From Advanced Telescope Supplies: `http://www.atscope.com.au/photometry.html`.

Tab. 4.3: Errors arising from normalization for each cross-section. That for Q_i^t is based on fitting measured Ar ion yields to Ar Q_i^t from Laricchia *et al.* (2002).

Cross-section	Q_i^t	Q_i^+	Q_{Ps}	Q_i^{ex}	$Q_i^{\mathrm{ex}/+}$	$Q_i^{\mathrm{ex}/\mathrm{Ps}}$
Error	1.0%	15.5%	15.5%	11.6%	20.0%	20.0%

$A\,^2\Pi$ state is $\sim 1 \times 10^{-17}$ cm^2, which indicates a contribution of 12%. The cross-section for formation of Ps in the $2P$ state from CO_2 is unknown at present, but indications (Laricchia *et al.*, 1988) are that it is also small by comparison to Q_i^{ex}. The best separation of the $A\,^2\Pi_u \rightarrow X\,^2\Pi_g$ and $B\,^2\Sigma_u^+ \rightarrow X\,^2\Pi_g$ transitions may be achieved thus:

$$\frac{k_{\mathrm{GI}} Y_{\mathrm{GI}} - t_{\mathrm{B}} k_{\mathrm{GO}} Y_{\mathrm{GO}}}{t_{\mathrm{A}} - t_{\mathrm{B}}} = Y_{\mathrm{A}} + Y_{\mathrm{CO}^+} + \frac{t_{\mathrm{B}}}{t_{\mathrm{B}} - t_{\mathrm{A}}} Y_{\mathrm{Ps}^*} \tag{4.3}$$

$$\frac{t_{\mathrm{A}} k_{\mathrm{GO}} Y_{\mathrm{GO}} - k_{\mathrm{GI}} Y_{\mathrm{GI}}}{t_{\mathrm{A}} - t_{\mathrm{B}}} = Y_{\mathrm{B}} + \frac{t_{\mathrm{A}}}{t_{\mathrm{A}} - t_{\mathrm{B}}} Y_{\mathrm{Ps}^*} \tag{4.4}$$

where $k_{\mathrm{GI,GO}} Y_{\mathrm{GI,GO}}$ represents the normalized yield using one of methods 3 or 4 from Section 2.2.3. Note that as the wavelength ranges for the two transitions are very similar, equations 4.3 and 4.4 also assume t for the $A\,^2\Pi \rightarrow X\,^2\Sigma^+$ transition in CO^+ is approximately equal to that for the $A\,^2\Pi_u \rightarrow X\,^2\Pi_g$ transition in $CO_2{}^+$. Hence, the Y_{CO^+} contribution cancels to form equation 4.4.

4.3 *Results and discussion*

The following sections consider each cross-section separately, comparing them to other experimental and theoretical determinations where available. The results are also grouped by target gas. In comparisons where variation between different determinations of a given cross-section are only in the magnitude, rather than in the energy dependence as well, the normalization error for each particular measurement should always be kept in mind. These are summarized in Table 4.3.

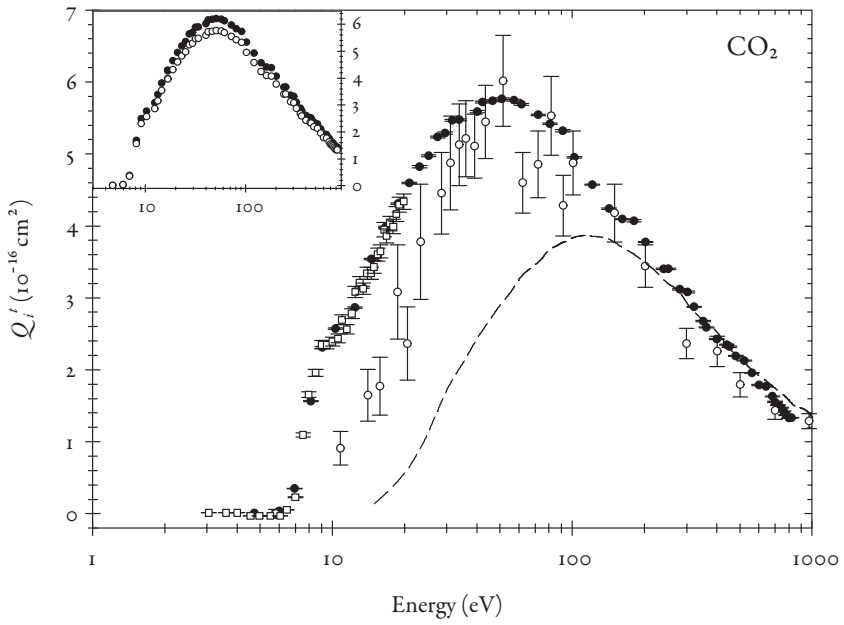

Fig. 4.1: Present measurement of Q_i^t (•) compared to that of Bluhme *et al.* (1999a) (○), the renormalised measurements of Laricchia &Moxom (1993) (▫) and the electron-impact cross-section of Straub *et al.* (1996a) (dashed line). Inset shows the comparison of two normalization methods: •—method 1 and ○—method 2 (as described in Section 2.2.3).

4.3.1 CO_2

Total ionization cross-section, Q_i^t

Figure 4.1 shows the present measurement of Q_i^t for CO_2 (Laricchia *et al.*, 2009). It peaks at an energy of ~ 50 eV with a magnitude of 5.76×10^{-16} cm^2, both earlier and larger in magnitude than the equivalent electron-impact cross-section (Straub *et al.*, 1996a). The cross-sections for positron- and electron-impact merge around 300 eV, though the gradients of the high energy tail differ. In the region 600–800 eV, this difference is approximately 35%. This suggests that the Born approximation may still not be applicable, that is, that the sign of the charge on the particle still has an effect on the processes involved.[†] Fair agreement with Bluhme *et al.* (1999a) above an energy of 40 eV, below which the present measurement exceeds it by as much as a factor of 2. This agreement is coincidental, as the results of Bluhme *et al.* (1999a) are for non-dissociative ionization only, whereas the present results represent the sum of non-dissociative and (a fraction of) dissociative ionization cross-sections. This may be part of the reason for the differences between the two measurements. Also, it should be noted that the normalization method employed by Bluhme *et al.* involved conducting the experiments with a mixture of gases (He and CO_2) and normalizing to a known He cross-section. The raw ion yields for points below the He single ionization threshold were scaled to those just above threshold and normalized accordingly, assuming a substantially constant pressure and e^+ beam intensity. Two independent normalizations of the present results are shown in the inset to Figure 4.1, differing by less than 10%.

Also shown on Figure 4.1 are the high-energy-resolution measurements of Laricchia &Moxom (1993, $\Delta E \sim 1$ eV). Excellent agreement in shape is demonstrated, though the data have been multiplied by a factor of ~2 in order to normalize to the present results. However, the original normalization of the Laricchia &Moxom (1993) data has an uncertainty of up to ±50% (Laricchia *et al.*, 1994), so the difference in absolute scale between these and the present measurements may not be significant.

[†] The agreement between normalization methods demonstrated in Section 2.2.3 suggests that the Born approximation is applicable at least to within 7%; convergence may occur at higher energies than were probed in the present work.

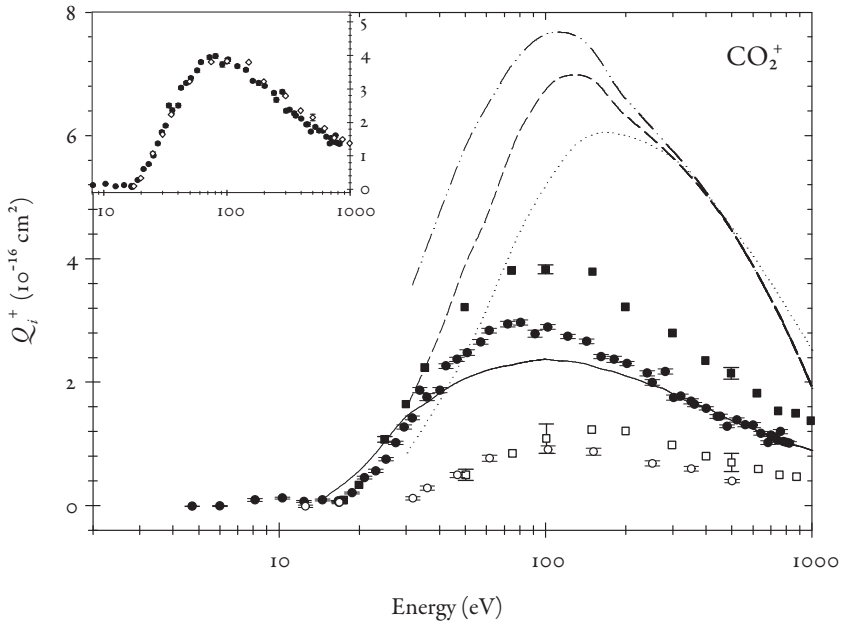

Fig. 4.2: Present measurements of Q_i^+ and Q_i^{diss} (● and ○, respectively) compared with those of Bluhme *et al.* (1999a) (■ and □, respectively). Differences in magnitude between the two measurements arise from the choice of the electron normalization data—the inset shows the present measurement of Q_i^+ renormalized to Bluhme *et al.* (1999a). Also shown are the electron measurements of Straub *et al.* (1996a) (solid line) and the DWBA calculations of Tóth *et al.* (2006) (CPE—dotted curve, ES—dashed curve, TS—double chain curve).

Direct ionization cross-section, Q_i^+

The cross-sections for non-dissociative and dissociative ionization (Cooke *et al.*, 2008) are shown in Figure 4.2. Q_i^+ can be seen to peak at ~ 80 eV with a magnitude of ~ 3.0×10^{-16} cm², and Q_i^{diss} at an energy of 100 eV with a cross-section of ~ 0.9×10^{-16} cm². In this case, disagreement with the only other available experimental determination (Bluhme *et al.*, 1999a) arises solely from the electron data chosen for normalization,[‡] namely those of Orient & Srivastava (1987) and Straub *et al.* (1996a), the former being systematically higher than the more recent measurements. The inset to Figure 4.2 demonstrates the similarity in energy dependence between the two measurements. However, the present normalization has been checked by using Ar Q_i^t via equation 4.5 (method 2, Section 2.2.3):

$$Q_i^+ = \left(\frac{Q_i^t}{Y_i}\right)_{\text{Ar}} \left(\frac{P_{\text{CO}_2}}{P_{\text{Ar}}}\right) \left(\frac{1}{\varepsilon_+ t_g^4}\right) Y_i^+ \tag{4.5}$$

and the two methods agree to within 7% (as demonstrated in the inset to Figure 4.1), so one can have confidence in the determination of the absolute scale.

Comparison with the electron data of Straub *et al.* (1996a) reveals an excess at the peak, but a crossing of the cross-sections at low energy (~ 30 eV) meaning the lowest energy positron impact points lie below those for electron impact. This is commonly observed in other gaseous targets and is attributed to a combination of the additional ionization channel available to positrons at those energies (i.e. Ps formation) and the so-called 'binding/anti-binding' effect (see, e.g Knudsen *et al.*, 1995). This is the process whereby an incoming electron passing inside the atomic (molecular) electron shell (orbital) has the effect of lowering the binding potential for outer electrons (anti-binding), the opposite being true for positrons.

Figure 4.2 also includes the results of DWBA calculations of Tóth *et al.* (2006) (see also Section 1.4). The correspondence between theory and experiment for this molecule is very poor. A reason for this has been suggested (Campeanu *et al.*, 2005), with the possibility of improvement being attainable through the use of a multicentered Coulombic function to describe the outgoing electron.[§]

[‡] The difference in magnitude is also consistent with that observed for Q_i^t where the non-dissociative ionization measurements of Bluhme *et al.* (1999a) are seen to be of the same magnitude as the total ionization cross-section from the present study.

[§] It is noted, however, that this would make the calculations significantly more challenging.

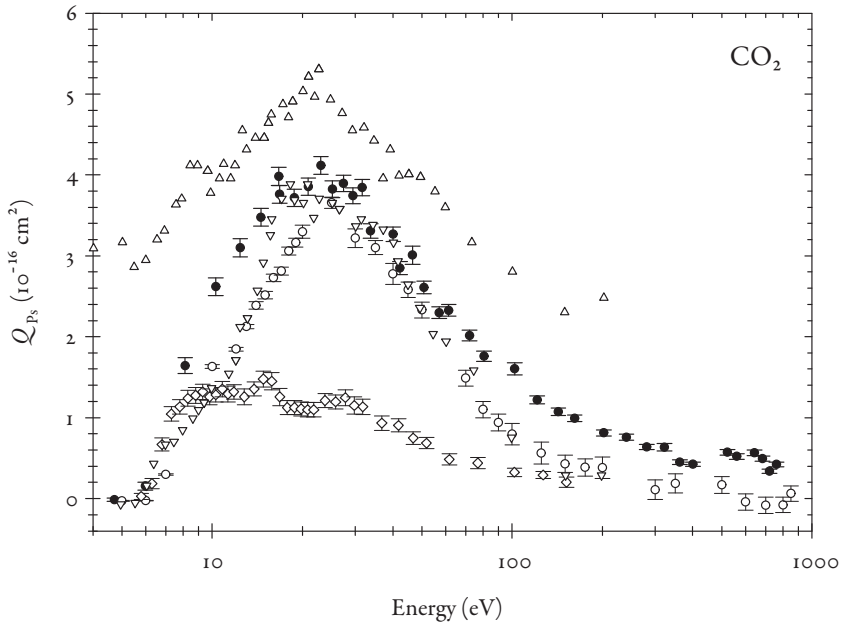

Fig. 4.3: Present measurement of Q_{Ps} (•) (Cooke *et al.*, 2010b) compared with that of Murtagh *et al.* (2006) (○), the upper (△) and lower (▽) limits of Kwan *et al.* (1998) and the early work of Griffith (1984) (◇).

Positronium formation cross-section, Q_{Ps}

Positronium formation from CO_2 has been investigated by a number of groups (Murtagh *et al.*, 2006; Kwan *et al.*, 1998; Griffith, 1984). Figure 4.3 comprises a comparison between the present determination (Cooke *et al.*, 2010b) and earlier measurements. The cross-section peaks at ~ 20 eV with a value of around 4.0×10^{-16} cm^2. Fair agreement is observable between three data sets: the present work, that of Murtagh *et al.* (2006) and the lower limit of Kwan *et al.* (1998). The lowest energy points of Griffith (1984) are also in agreement with these measurements.[¶] The discrepancies between the present measurements and those of Murtagh *et al.* (2006) may arise as a result of the latter work failing to take into account dissociative ionization—this determination having been obtained by subtracting Q_i^+ from Q_i^t. Both Q_i^t and Q_i^+ in the work of Murtagh *et al.* (2006) were normalized to the same electron cross-section, which ensures that Q_{Ps} falls to zero at high energies. The convergence of the results of three (four, at low energy) separate methods

[¶] The higher energy points from this study are now known to have been affected by quenching of Ps on the cell walls and are therefore thought to be incorrect (see Section 1.3.1)

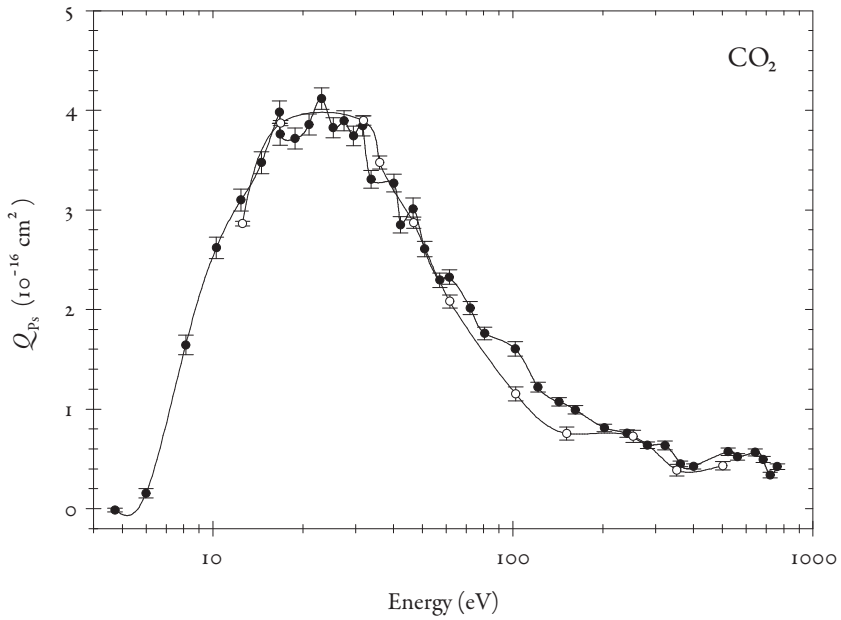

Fig. 4.4: Comparison of Q_{Ps} measured using γ-ray–ion coincidences (•) and the difference between Q_i^t and $Q_i^+ + Q_i^{diss}$ (○).

provides confidence in the energy dependence and absolute scale of the cross-section. As a measure of internal consistency, Figure 4.4 shows the comparison between Q_{Ps} measured in this work in two different ways: using γ-ray–ion coincidences, and using the method of Murtagh *et al.* (2006). As a result of the complexities of modelling capture processes from complex targets, no theoretical data are yet available for comparison.

Simultaneous ionization–excitation cross-section, Q_i^{ex}

Figure 4.5 shows the present determination of Q_i^{ex} for electron impact, compared to the electron measurements of Tsurubuchi & Iwai (1974). These measurements were performed for normalization purposes, in order to test the system parameters described by equations 4.3–4.4, and also as a diagnostic of the system when used as an electron beam. As the performance of the system in electron beam configuration is sub-optimal and the results shown are the product of a limited number of separate measurements, some scatter in the points is be expected. However, from the agreement with previous measurements, confidence can be had in the separation of transitions using the method described in Section 4.2.1.

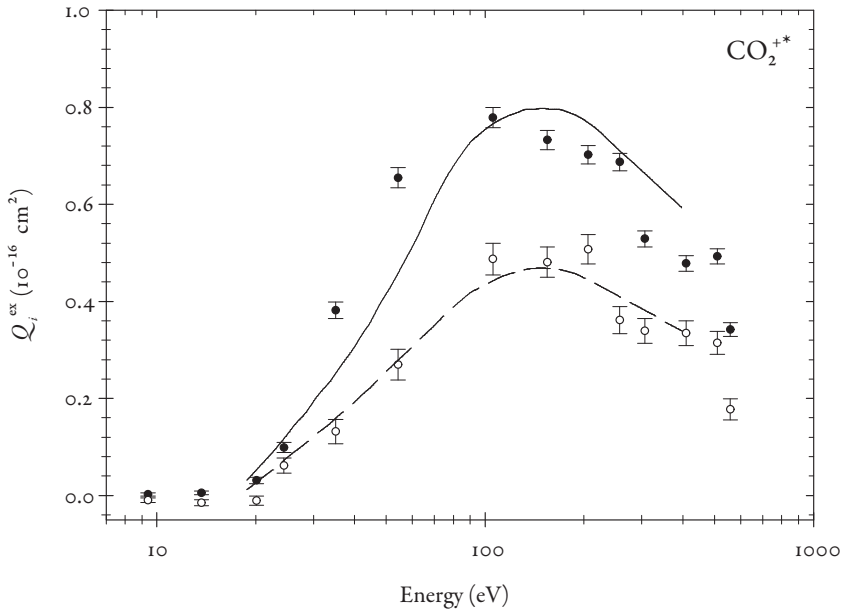

Fig. 4.5: Measurement of state-separated Q_i^{ex} for electron impact ($A\,^2\Pi_u \rightarrow X\,^2\Pi_g$—•, $B\,^2\Sigma_u^+ \rightarrow X\,^2\Pi_g$—○), compared with Tsurubuchi &Iwai (1974) ($A\,^2\Pi_u \rightarrow X\,^2\Pi_g$—solid line, $B\,^2\Sigma_u^+ \rightarrow X\,^2\Pi_g$—dashed line).

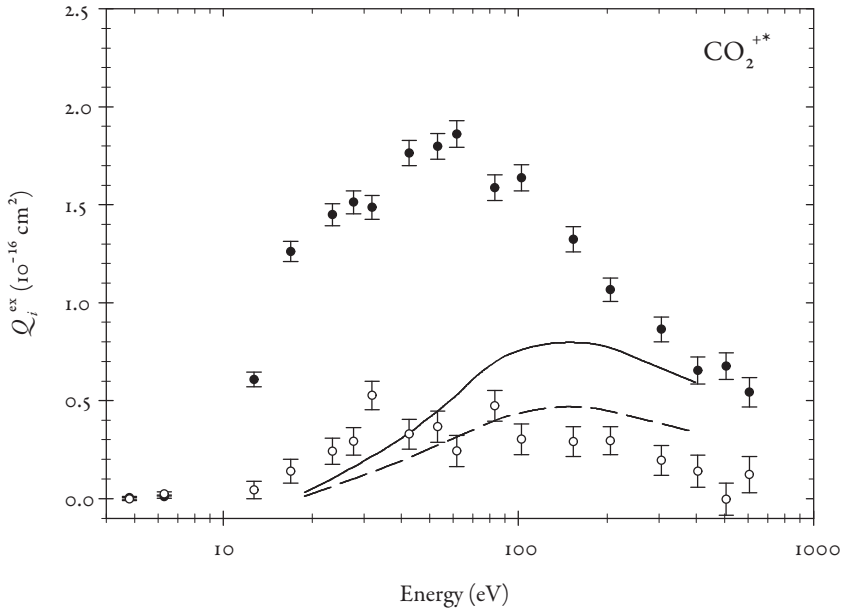

Fig. 4.6: As Figure 4.5, but for positron impact.

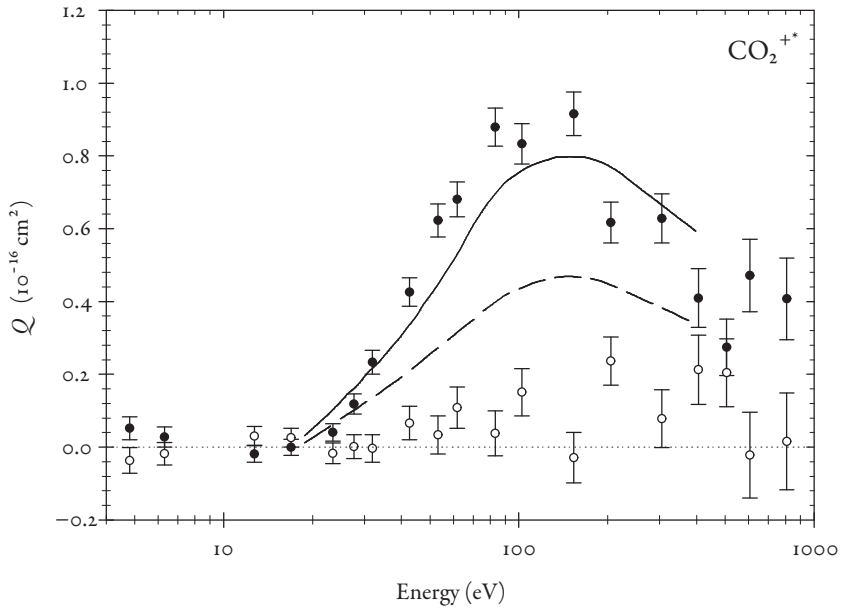

Fig. 4.7: Contribution of direct ionization to the cross-section in Figure 4.6. Legend as Figure 4.6.

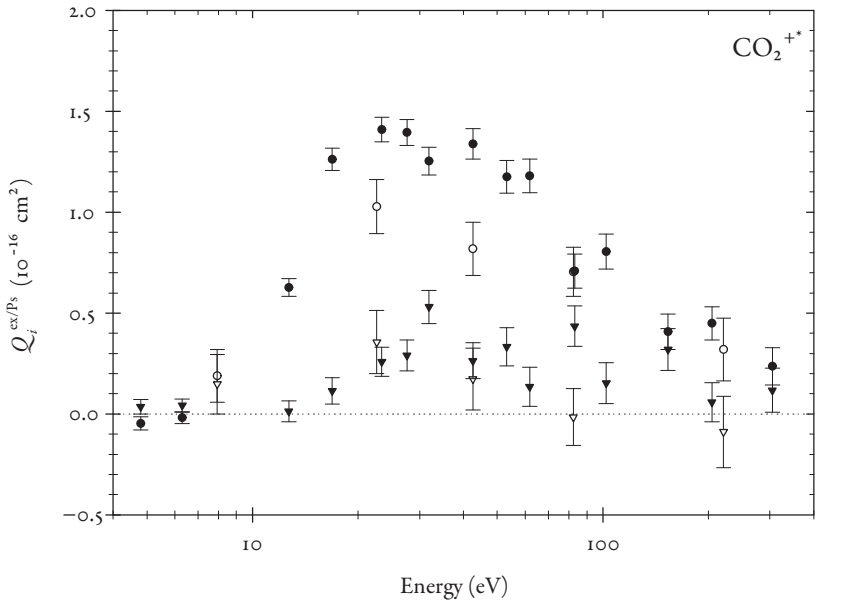

Fig. 4.8: Contribution of Ps formation to the cross-section in Figure 4.6. • and ▾ are contributions from $A\ ^2\Pi_u \rightarrow X\ ^2\Pi_g$ and $B\ ^2\Sigma_u^+ \rightarrow X\ ^2\Pi_g$ respectively, measured using $Q_i^{\mathrm{ex/Ps}} = Q_i^{\mathrm{ex}} - Q_i^{\mathrm{ex/+}}$; ○ and ▿ are the same, measured using γ-ray–photon coincidences.

The situation is more complex in the case of positron impact as equations 4.3–4.4 both contain a residual contribution from excited-state Ps, the magnitude of which is unknown, and cannot be measured with the present set-up. The results for the $B\ ^2\Sigma_u^+ \rightarrow X\ ^2\Pi_g$ transition in figures 4.6–4.8 can therefore only satisfactorily be described as $Q_i^{\mathrm{ex}/B\ ^2\Sigma_u^+ \rightarrow X\ ^2\Pi_g} + Q_{\mathrm{Ps}}^*$. However, on the understanding that this is the case, for brevity this shall be labelled $Q_i^{\mathrm{ex}/B}$ and the corresponding cross-section for the $A\ ^2\Pi_u \rightarrow X\ ^2\Pi_g$ transition labelled $Q_i^{\mathrm{ex}/A}$. Figures 4.6–4.8 show the present positron impact cross-sections $Q_i^{\mathrm{ex}/A}$ and $Q_i^{\mathrm{ex}/B}$ and their partitioning into contributions from direct ionization and Ps formation, respectively (Cooke *et al.*, 2010a). Two things are immediately apparent: first, that the cross-section $Q_i^{\mathrm{ex}/A}$ for positron impact is enhanced with respect to that of electron impact; and second, that this enhancement derives exclusively from Ps formation. The first of these points is perhaps unsurprising—this is common among total ionization cross-sections in atoms. The second point at first seems simply to mirror the situation of Q_i^t as well. However, it also represents corroborative evidence in support of a hypothesis put forward to explain the existence of the 'shoulder' visible in Q_i^t, which states:

> we note that the C-state of CO_2 lies at 10.56 eV above the ground state, i.e. only 60 meV above the threshold for Ps formation simultaneous to ion excitation…It seems as if Ps formation proceeds via a quasi-excitation, followed by a capture of the electron by a near-stationary positron, the remnant ion absorbing the difference in binding energies (Laricchia &Moxom, 1993).

While there appears to still be some ambiguity concerning the assignment of symmetries and energies of excited electronic states of CO_2 (Itikawa, 2002) and the precise energy (and indeed term symbol) may need updating, the argument still stands. Such an updated version, using tentative energy assignments from the review of Itikawa (2002), would relate the proximity of the $^1\Sigma_u^+$ state at 10.30–11.28 eV‖ (Nakatsuji, 1983; Chan *et al.*, 1993a) or ~ 11.34 eV (Buenker *et al.*, 2000) to the energy of Ps formation leaving the ion in the $A\ ^2\Pi_u$ state, which is in the range 10.52–11.22 eV.** The present measurements support this hypothesis by demonstrating that Ps formation is the dominant ionization process that leaves the remnant ion in the $A\ ^2\Pi_u$ state. In addition to this, there is supporting evidence that significant Ps is formed from inner-shell electrons by measurements of 3γ:2γ ratios

‖ The peak in optical oscillator strength is closer to 11.0 eV.

** Based on CO_2 ionization potential 13.77 eV (Linstrom &Mallard, 2010), Ps binding energy of 6.8 eV and the vibrational level assignments of $CO_2^+\ A\ ^2\Pi_u$ from Ajello (1971) and Tsurubuchi &Iwai (1974) for electron impact.

(Kauppila *et al.*, 2004b). An increase in this ratio with energy suggests a new threshold for o-Ps formation (which uniquely produces the three γ-ray signature)—one such peak was identified at an energy of 5–8 eV above the Ps($n = 1$) threshold, consistent with the threshold for this process.

4.3.2 N_2

For N_2, the individual resolution of N_2^+ and N^+ was not possible and it was assumed for normalization purposes that the yields represented the sum of non-dissociative and dissociative processes. This introduces an additional uncertainty on the absolute magnitude of all the present measurements as N^+ will have a lower collection efficiency owing to its higher kinetic energy (Van Brunt &Kieffer, 1975).[††] However, without prior knowledge of the cross-section for dissociative ionization, it is difficult to assess the amount of 'missing' N^+ (a future direction for this work is fragment resolution, as discussed in Chapter 5). An estimate of this uncertainty is given in the next section.

Q_i^t

The upper graph of Figure 4.9 shows the present measurement of Q_i^t for N_2, together with the corresponding electron measurements of Straub *et al.* (1996b) to which they have been normalized. The present cross-section peaks at 40–50 eV with a magnitude of approximately 4.8×10^{-16} cm^2. The convergence between positron- and electron-impact cross-sections is more convincing than in the case of CO_2 (where the gradients fail to match even at the highest measured energies) suggesting that projectile-charge-sign independence is reached by 400–500 eV impact energy. Also shown are the previous experimental determination of Marler &Surko (2005). Excellent shape agreement between the two data sets may be observed in the inset to this figure.

The lower graph of Figure 4.9 shows the total ionization cross-section for N_2^+ production only. In the present work, this has been estimated by assuming no collection of N^+ and normalized to the electron data of Straub *et al.* (1996b) for the non-dissociative component of the cross-section only. The comparison with the results of Bluhme *et al.* (1998) is reminiscent of that between direct non-dissociative ionization of CO_2 results. Data from the present study are consistently lower than those from Bluhme *et al.* (1998) and Bluhme

[††] Typically, the collection efficiency for molecular fragments is ~50% of that for the parent ion, though the kinetic energy profiles vary with the impact energy of the projectile, so the efficiency is energy dependent.

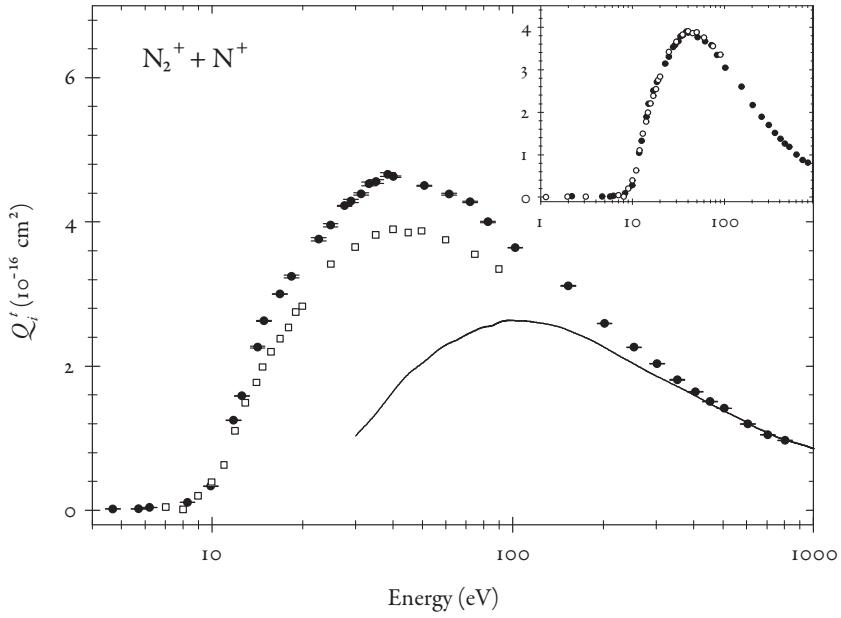

Fig. 4.9: Top: present measurement of Q_i^t for N_2 (•) compared with that of Marler &Surko (2005) (▫) and the electron measurements of Straub *et al.* (1996b) (solid line). Inset shows the present results renormalized to those of Marler &Surko (2005), demonstrating shape agreement. Bottom: present measurement of Q_i^t for N_2 assuming no collection of N^+ (•), compared with the measurements of Bluhme *et al.* (1998) (○) and the electron measurements of Straub *et al.* (1996b) (solid line).

et al. (1999a) which, it is noted, also exceeds the total ionization for N_2^+ and N^+ production of Marler & Surko (2005). These renormalized results for Q_i^t have a magnitude 80% of those in the upper half of Figure 4.9, leading to an upper estimate on the normalization error of 20% (corresponding directly to the ratio of dissociative to non-dissociative ionization cross-sections for electron impact).

Q_i^+

As with Q_i^t for this target, Figure 4.10 shows the cross-section normalized assuming complete (top) and zero (bottom) collection of N^+. Good agreement between the present measurements and those of Marler & Surko (2005) is demonstrated by the top graph, while the lower graph shows the characteristic discrepancy between this study and the work of Bluhme *et al.* (1998), owing to the different electron data sets used for normalization. All three experimental determinations peak at an energy of ~ 100 eV. As with atomic targets (see Section 1.5) and CO_2, the cross-section for positron impact falls below that for electron impact at the lowest impact energies. Comparison with theory (Tóth *et al.*, 2006) is more favourable for this target than for CO_2, though the calculations are still higher than the present measurements at all energies. The improvement over CO_2 may be attributable to the relatively compact nature of the N_2 molecule. The nitrogen triple bond[‡‡] and the lack of a third atom in N_2 may mean the molecule is more accurately modelled by a single-centered potential than CO_2.

Q_{Ps}

The present measurement of Q_{Ps} for N_2 (Cooke *et al.*, 2010b) is shown in Figure 4.11, compared with the other available experimental determinations, that of Marler & Surko (2005) and the early measurements of Griffith (1984). It peaks at approximately 30 eV with a value of 3.6×10^{-16} cm^2. Fair shape agreement between this work and that of Marler & Surko (2005) (as with Q_i^t and Q_i^+) is evident (see inset), though the present work exhibits a high-energy tail, which does not appear in Marler & Surko (2005). However, as these measurements terminate at < 100 eV, it is non-trivial to extrapolate to several hundred eV. As with CO_2, a comparison of two methods for deriving Q_{Ps} is displayed in Figure 4.12 to demonstrate internal consistency in the present measurements. Note that both methods predict the existence of a high-energy tail to the cross-section as with CO_2.

[‡‡] One of the strongest covalent bonds in nature, of length N≡N ~106 pm. Compare this with that of a C=O bond in CO_2 (116 pm), and bear in mind there are two such bonds.

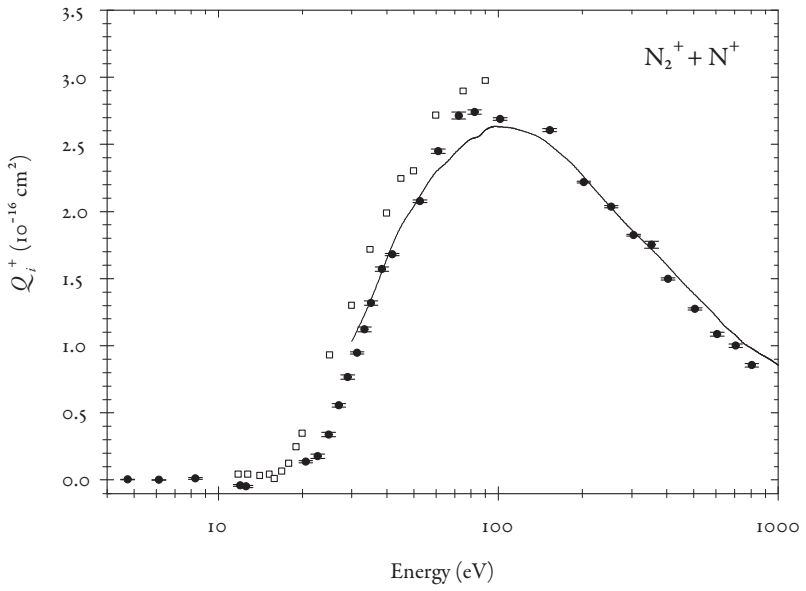

(a)

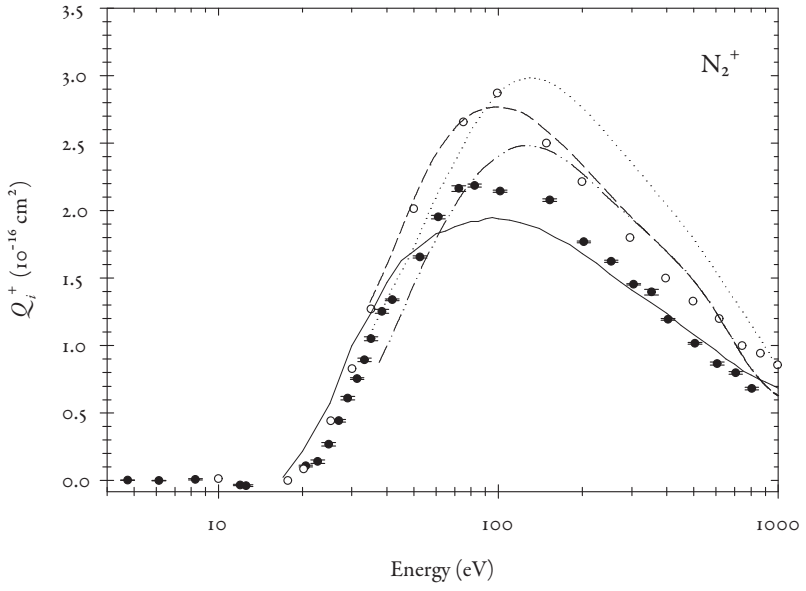

(b)

Fig. 4.10: Top: Present measurement of Q_i^+ (•) compared with measurements of Marler &Surko (2005) (▫) and the electron measurements of Straub *et al.* (1996b) (solid curve). Bottom: present measurement renormalized assuming no collection of N^+ (•) compared to the measurements of Bluhme *et al.* (1998) (○), the electron data of Straub *et al.* (1996b) (solid line), and the DWBA calculations of Tóth *et al.* (2006) (legend as Figure 4.2).

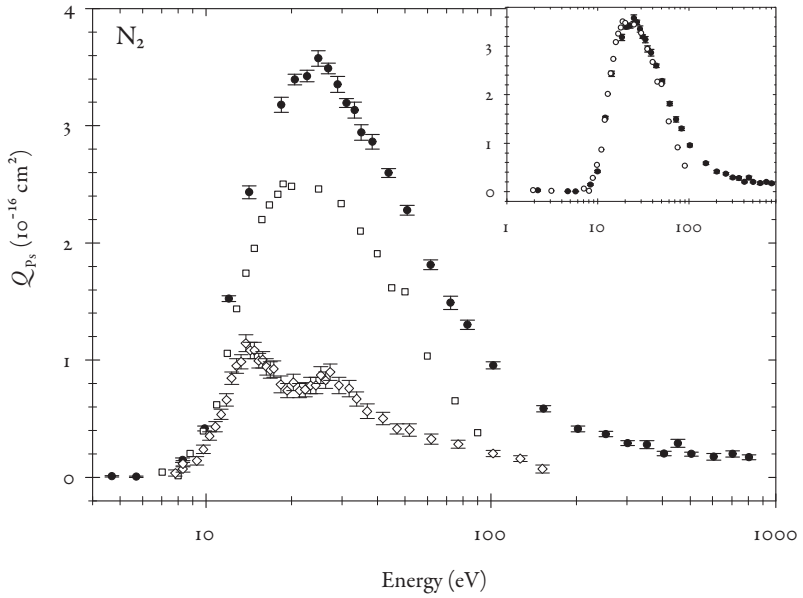

Fig. 4.11: Three experimental determinations of Q_{Ps}: •—present measurement (Cooke *et al.*, 2010b), ▫—Marler &Surko (2005), ◇—Griffith (1984). Inset: present measurement compared those of Marler &Surko (2005) renormalized to demonstrate energy dependence similarity.

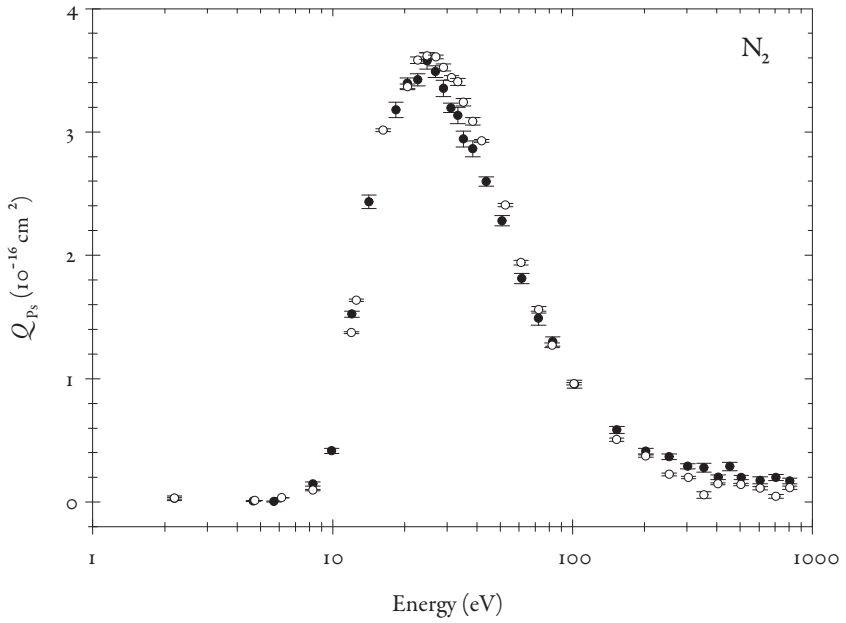

Fig. 4.12: Comparison of Q_{Ps} measured using γ-ray–ion coincidences (•) and the difference between Q_i^t and Q_i^+ (○).

Q_i^{ex}

A summary of cross-sections for ionization leaving the ion in the $B\ ^2\Sigma_u^+$ state is shown in Figure 4.13, including partitioning into contributions from direct ionization and Ps formation (Cooke *et al.*, 2010a), and the equivalent electron data from Borst &Zipf (1970). The total ionization–excitation cross-section is considerably larger (by a factor of approximately 5) than that for electron-impact, disproportionately so in comparison to Q_i^t (Figure 4.9), where the positron- and electron-impact cross-sections have merged by 500 eV. This effect again appears to be associated with Ps formation, though less exclusively than in the case of CO_2. The positron:electron cross-section ratio for the direct process $Q_i^{ex/+}$ is larger than for Q_i^+, by a factor of two at the peak, in contrast to CO_2, where it is suppressed by comparison.

It is possible to form a similar energy threshold proximity argument for this process in N_2, as with CO_2. However, with N_2, the states of the neutral molecule (that is, the initial states in the relaxation process) are less clearly defined. Within the appropriate energy range, there exist four candidate states, namely: $b\ ^1\Pi_u$, $b'\ ^1\Sigma_u^+$, $c\ ^1\Pi_u$ and $c'\ ^1\Sigma_u^+$. These all have energies in the range 12.50–13.95 eV (Chan *et al.*, 1993b; Lofthus &Krupenie, 1977),

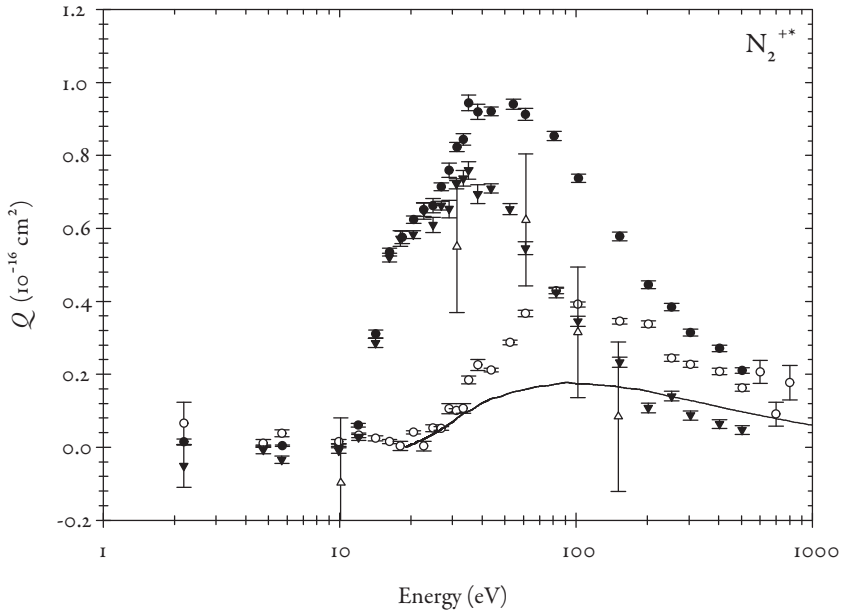

Fig. 4.13: Summary of ionization–excitation cross-sections for N_2: •—Q_i^{ex}, ○—$Q_i^{ex/+}$, ▼ and △—$Q_i^{ex/Ps}$ measured using $Q_i^{ex/Ps} = Q_i^{ex} - Q_i^{ex/+}$ and γ-ray–photon coincidences, respectively; solid curve—electron data of Borst & Zipf (1970).

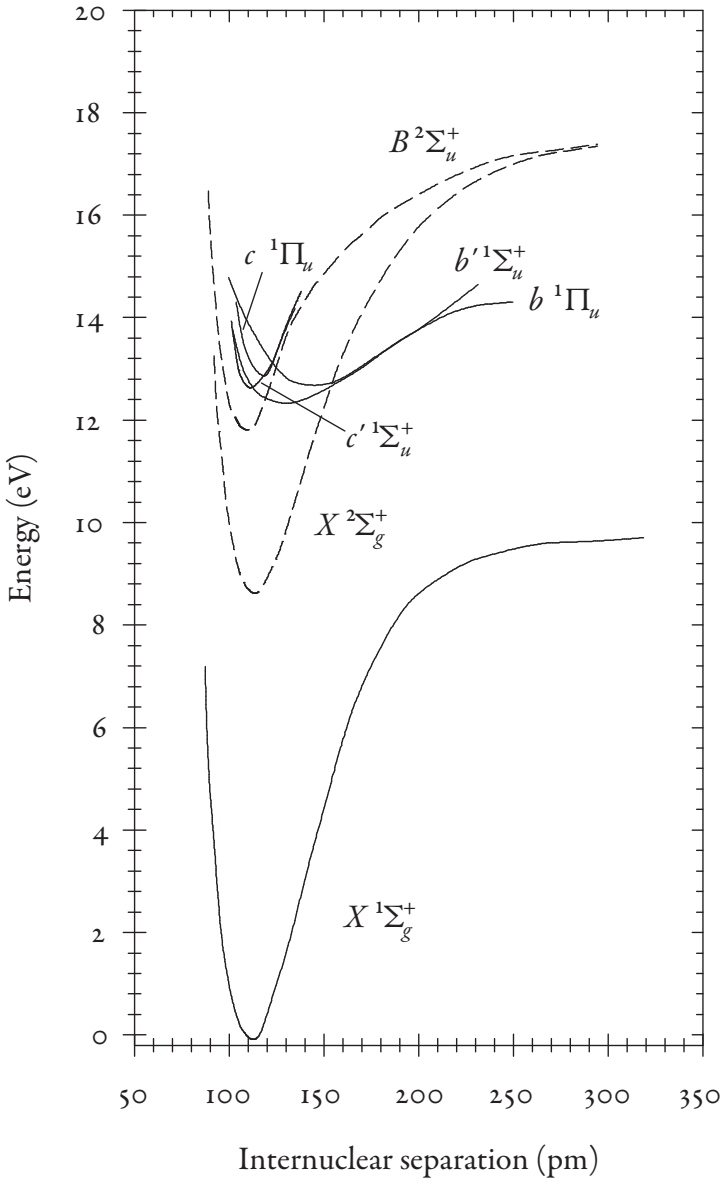

Fig. 4.14: Potential energy curves for relevant states of N_2 (solid curves) and N_2^+ (dashed curves) (Lofthus &Krupenie, 1977), with those of the ion shifted down by 6.8 eV, the binding energy of Ps.

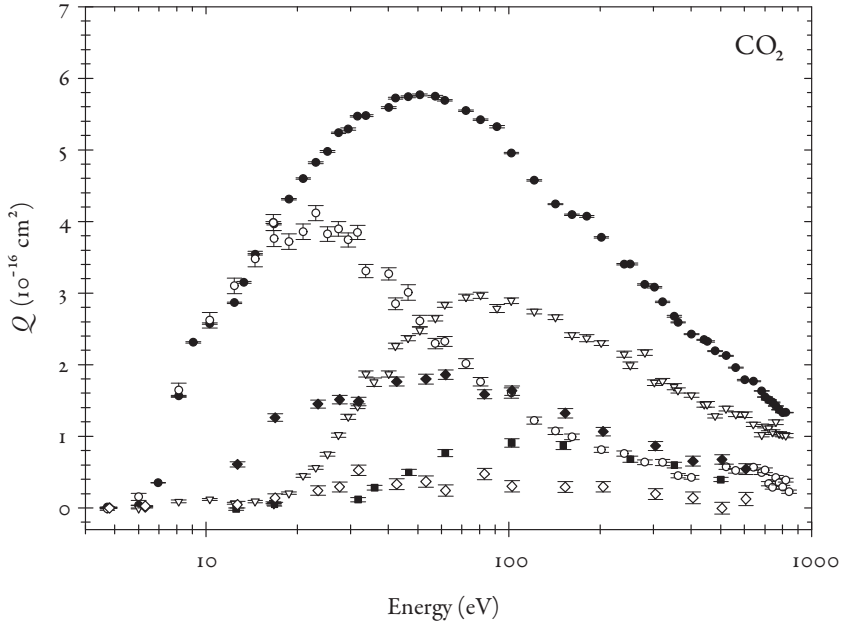

Fig. 4.15: Collection of all present measurements of cross-sections for various positron–CO_2 scattering processes: Q_i^t (●), Q_i^+ (▽), Q_i^{diss} (■), Q_{Ps} (○), Q_i^{ex} for $A\ ^2\Pi_u$ state (◆) and Q_i^{ex} for $B\ ^2\Sigma_u^+$ state (◇). Partitioning of Q_i^{ex} has been omitted for the sake of clarity.

while the energy threshold of ionization–excitation into $B\ ^2\Sigma_u^+$ with Ps formation is ~ 12.0 eV. This is depicted in Figure 4.14, which shows the potential energy curves for these states, and the ground states of the neutral molecule and ion.

An attempt was made to measure the cross-section for excited-state Ps formation using the same method as in Chapter 3. This was possible in the case of N_2, in contrast to CO_2, as no ionic de-excitation photons have wavelength ranges which overlap with that of the Lyman-α line from Ps. The result of this attempt was a mean value of $(1.1 \pm 1.1) \times 10^{-17}$ cm² over the low energy range of Q_{Ps}, that is, zero to within experimental resolution.

4.4 *Concluding remarks*

Figures 4.15 and 4.16 show all measured cross-sections for positron impact on CO_2 and N_2 from the current study. The first important point to note is that the absolute scale of all measurements depends only on the normalization of Q_i^t (see Section 2.2.2). As the relative scale of the cross-sections will remain unchanged even if the absolute scale is adjusted, it is possible to check the consistency of the results by adding up the components of Q_i^t.

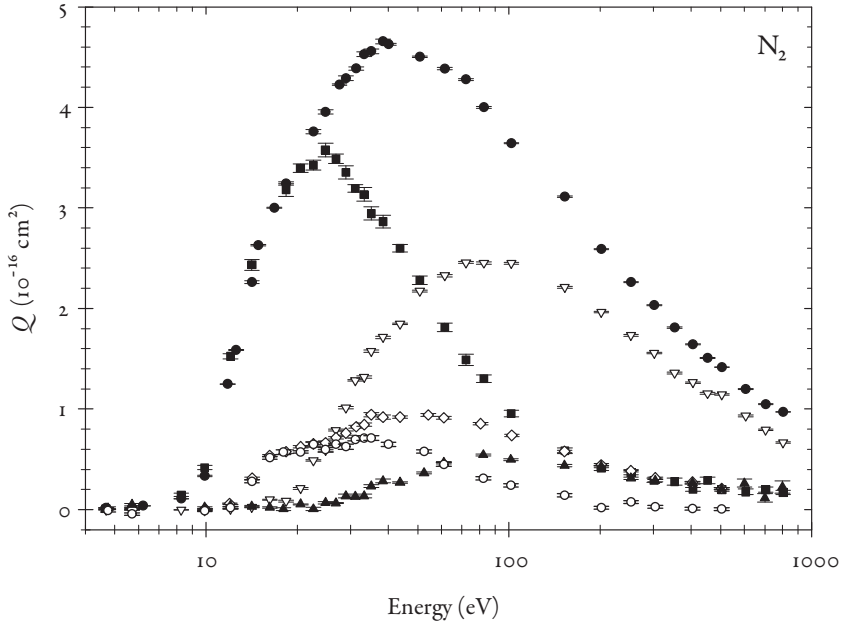

Fig. 4.16: Collection of all present measurements of cross-sections for various positron–N_2 scattering processes: Q_i^t (●), Q_i^+ (▽), Q_{Ps} (■), Q_i^{ex} for $B\ ^2\Sigma_u^+$ state (◇), $Q_i^{ex/+}$ (▲) and $Q_i^{ex/Ps}$ (○).

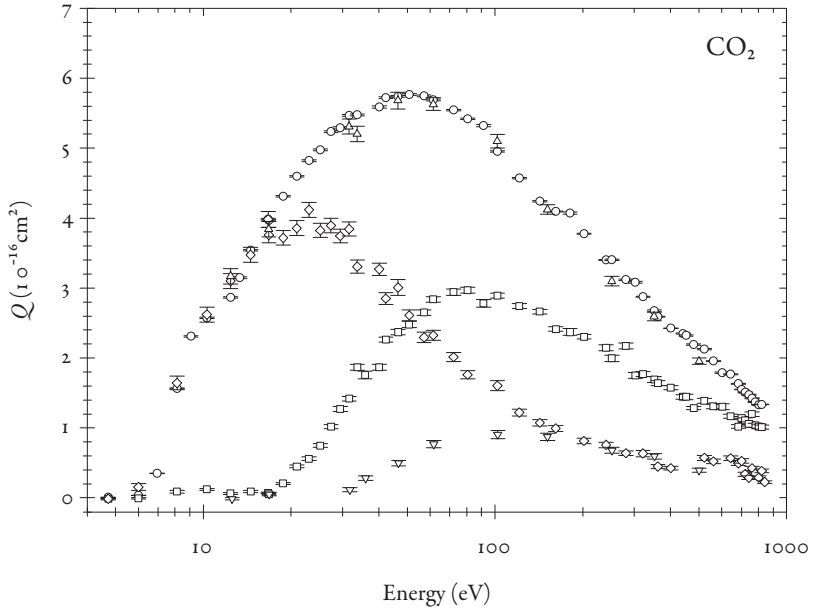

(a)

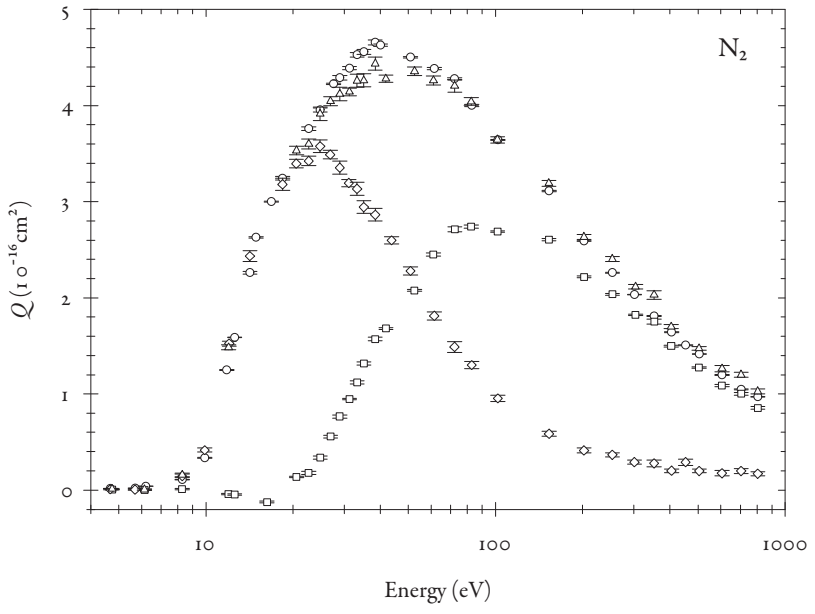

(b)

Fig. 4.17: Comparison of Q_i^t for CO_2 and N_2, as measured directly and formed from the sum of its components. Q_i^t (○), Q_i^+ (□), Q_{Ps} (◇), Q_i^{diss} (▽—CO_2 only), sum of components (△).

This is demonstrated in Figure 4.17, which shows the sum of Q_i^+, Q_{Ps} and Q_i^{diss} (where appropriate) compared with Q_i^t itself. Extremely good agreement is achieved between the two determinations of Q_i^t. Note that for CO_2, the agreement to within 7% of more than one normalization method allows greater confidence in the absolute scale than for N_2, where, due to the lack of resolution of molecular fragments, normalization could only proceed using existing electron data.

The enhancement of Q_i^{ex} by positron impact over electron, for both targets, may be described as an asymmetric or 'accidental resonance' process (Bates &Lynn, 1959). This occurs when the energy defect (that is, the difference in energy) between two states is small, though unlike a symmetric resonance, the states need not be identical.[§§] The study of this phenomenon has mainly concentrated on collisions involving heavy ions (Massey &Gilbody, 1974), so there are no velocity-comparable experimental data from earlier work. Theoretical work (e.g. Rapp &Francis, 1962) is largely confined to the behaviour of collisions involving atoms. However, from these studies, it emerges that for increasing impact energy, the distinction between cross-sections for symmetric and asymmetric resonance processes is lost, i.e. the cross-sections merge (Rapp &Francis, 1962).[¶¶] The energy at which this happens depends on the defect between the states; the larger this energy defect is, the less resonant-like the cross-section appears. At low energies, cross-sections for accidental resonances will fall rapidly to zero. When compared to non-resonant charge-exchanging collisions, a clear enhancement to the cross-section is evident (as seen by Ottinger &Simonis (1978) using projectile ions of the same species in differing excited states). This is similar to the situation observed in the present study, with one difference: the initial state of the resonant system is only accessible above a collision energy equal to the excitation energy of that state. Thus rather than a simple accidentally resonant reaction, it may be more appropriate to describe it as a two-step process (shown here for CO_2):

$$\mathrm{e}^+ + \mathrm{CO}_2 \rightarrow \left(\mathrm{CO}_2\left(^1\Sigma_u^+\right) + \mathrm{e}^+\right) \rightarrow \mathrm{CO}_2{}^+\left(^2\Pi_u\right) + \mathrm{Ps} \qquad (4.6)$$

where the intermediate state is short-lived, but essential for the enhancement. The effect of this (other than to displace the threshold from zero energy) is unknown.

[§§] Symmetric resonances in charge-transfer collisions occur when the final state of the projectile is the same as the initial state of the target, e.g. $\mathrm{H}^+ + \mathrm{H} \rightarrow \mathrm{H} + \mathrm{H}^+$. Asymmetric resonances do not have this property; the small energy defect is an accident arising from the similarity in energy of particular states in the projectile and target.

[¶¶] That is, once the cross-sections have been transformed onto a common velocity scale by dividing the collision energy by the mass of the projectile.

This mechanism for enhancing ground-state Ps formation, although not fully understood,may also be responsible for the relative lack of excited-state Ps observed in N_2. No equivalent molecular states exist at only 1.7 eV (the binding energy of $n = 2$ Ps) below the ionization, so the enhancement mechanism does not exist for excited-state Ps. Indeed, the greater propensity for Ps formation into the ground state which exists for these molecules may reduce the excited-state Ps cross-section further.

5. FINAL REMARKS

In the present work, measurements of positron-impact ionization cross-sections in two molecules, CO_2 and N_2, and of excited-state Ps formation from Xe, have been conducted. An approximately monoenergetic positron beam was used in conjunction with multiple detectors to obtain as complete and self-consistent a set of measurements as possible. The simultaneous recording of several coincidence yields, corresponding to several different ionization processes, combined with careful assessment of the detection efficiencies of the system, has allowed the separation of relative yield from absolute scale. This has reduced the problem of measuring multiple cross-sections to one of normalization of a single yield, which itself has been attempted in more that one way. The good agreement seen between different normalization methods therefore can be taken as a validation of the magnitude of the measured cross-sections.

The present work motivates further investigation into positron–molecule ionization, an area which has had relatively little previous work. The study of additional small molecules, for example O_2, N_2O, CO, could establish whether Ps formation is instrumental in the enhancement of ionization–excitation cross-sections more generally, as it appears to be for CO_2 and N_2,* while examining the interactions of positrons with molecules of biological significance may be of use for the medical physics community. Such targets could include, for example, H_2O, CH_2O and larger organic molecules like DNA/RNA structural units (bases, (deoxy)ribose and phosphates).

The current experimental set-up would prove to be inadequate for investigation of some of these targets; a number of improvements would have to be made to the interaction region. Ideally, the study of any molecule containing hydrogen should be conducted on a system capable of resolving ionic fragments with masses differing only by 1 amu. This would require the ion extraction system to be altered in one (or more) of the following ways:

* A cursory examination of potential energy curves for O_2 suggests that this may *not* be the case for this molecule as the excited states are largely dissociative.

(a) Reduction of spatial extent of extraction region.

(b) Use of time-focussing electrostatic lenses in ion extraction path, to compensate for distribution of creation times and positions (Wiley &McLaren, 1955).

(c) Use of a pulsed extraction method, instead of continuous. This allows the use of significantly larger extraction fields, increasing the extraction efficiency of energetic fragments.

These adjustments all serve to decrease the spread in arrival times of ions at the detector. Initial simulations suggest fairly trivial modification of the existing gas cell would allow 1 amu mass resolution up to a mass of approximately 60 amu. The more complex potential targets may not be in the gas phase at room temperature so significant redesign work would be required to study them.

In order to study excitation events of molecules to a greater degree of accuracy, the photon collection system would also require modification. At present, the single-filter approach is already inadequate for complete state-resolution of even the simplest of molecules. Ideally, a system with a spectrometer would be used for such studies. However, this would usually require a narrow, precisely defined region in which photons were created. With the intensity of positron beam currently achievable, emphasis is placed on maximizing photon collection efficiency, a requirement naturally at odds with a small, collimated photon source. The use of additional glass filters would allow a more complex analysis of the wavelengths present without lowering the collection efficiency significantly. Narrow band-pass filters typically have quite low transmission coefficients even in the pass band (interference filters transmit approximately 30% at their peak wavelength), but the use of several long-pass filters, each with different cut-off wavelengths, would effectively provide fairly narrow band filters, allowing for crude spectroscopy.

As with any branch of experimental physics, it would also be instructive for related theoretical results to be produced. For the simple molecular interaction cross-sections, the reproduction of experimental measurements would be desirable. However, for the larger organic molecules it may be more instructive (and achievable) if the experimental work forms the starting point for theoretical studies of (for example) radiation damage to living tissue, rather than attempting to model the interaction cross-sections themselves.

BIBLIOGRAPHY

Adachi, S., Chiba, M., Hirose, T., Nagayama, S., Nakamitsu, Y., Sato, T. & Yadama, T. (1994). *Phys. Rev. A* **49**, 3201.

Ajello, J. (1971). *J. Chem. Phys.* **55**, 3169.

Andersen, L. H., Hvelplund, P., Knudsen, H., Møller, S. P., Pedersen, J. O. P., Tang-Petersen, S. & Uggerhøj, E. (1990). *Phys. Rev. A* **41**, 6536.

Anderson, C. D. (1933). *Phys. Rev.* **43**, 491.

Armitage, S., Leslie, D. E., Beale, J. & Laricchia, G. (2006). *Nucl. Instr. Meth. B* **247**, 98.

Armour, E. A. G. (1982). *Phys. Rev. Lett.* **48**, 1578.

Bartschat, K. (2005). *Phys. Rev. A* **71**, 032718.

Basu, M. & Ghosh, A. S. (1988). *J. Phys. B* **21**, 3439.

Basu, M., Mazumdar, P. S. & Ghosh, A. S. (1985). *J. Phys. B* **18**, 369.

Bates, D. R. & Lynn, N. (1959). *Proc. Roy. Soc.* **253**, 144.

Bates, D. R. & Walker, J. C. G. (1966). *Planet. Space Sci.* **14**, 1367.

Benedetti, S. D. & Corben, H. C. (1954). *Ann. Rev. Nucl. Sci.* **4**, 191.

Berko, S. & Pendleton, H. N. (1980). *Ann. Rev. Nucl. Part. Sci.* 30, 543.

Birley, J. H. (1974). *Phys. Rev. A* **10**, 550.

Blackett, P. M. S. & Occhialini, G. P. S. (1933). *Proc. Roy. Soc.* **139**, 699.

Bluhme, H., Frandsen, N. P., Jacobsen, F. M., Knudsen, H., Merrison, J. P., Mitchell, R., Paludan, K. & Poulsen, M. R. (1999a). *J. Phys. B* **32**, 5825.

Bluhme, H., Frandsen, N. P., Jacobsen, F. M., Knudsen, H., Merrison, J. P., Paludan, K. & Poulsen, M. R. (1998). *J. Phys. B* **31**, 4631.

Bluhme, H., Knudsen, H., Merrison, J. P. & Nielsen, K. A. (1999b). *J. Phys. B* **32**, 5835.

Borst, W. L. & Zipf, E. C. (1970). *Phys. Rev. A* **1**, 834.

Bozek, J. D., Furst, J. E., Gay, T. J., Gould, H., Kilcoyne, A. L. D., Machacek, J. R., Martín, F., McLaughlin, K. W. & Sanz-Vicario, J. L. (2006). *J. Phys. B* **39**, 4871.

Brawley, S. J., Beale, J., Armitage, S., Leslie, D. E., Kövér, Á. & Laricchia, G. (2008). *Nucl. Instr. Meth. B* **266**, 497.

Bregman-Reisler, H. & Doering, J. P. (1975). *J. Chem. Phys.* **62**, 3109.

Brundle, C. R. & Turner, D. W. (1969). *J. Mass. Spectry, Ion Phys.* **2**, 195.

Buenker, R. J., Honigmann, M., Liebermann, H. & Kimura, M. (2000). *J. Chem. Phys.* **113**, 1046.

Burdyuzha, V. V. & Kauts, V. L. (1998). *Astrophys. Space Sci.* **258**, 329.

Campbell, C. P., McAlinden, M. T., Kernoghan, A. A. & Walters, H. R. J. (1998). *Nucl. Instr. Meth. B* **143**, 41.

Campeanu, R. I., Chiş, V., Nagy, L. & Stauffer, A. D. (2005). *Phys. Lett. A* **344**, 247.

Campeanu, R. I., McEachran, R. P. & Stauffer, A. D. (1996). *Can. J. Phys* **74**, 544.

Campeanu, R. I., McEachran, R. P. & Stauffer, A. D. (2002). *Nucl. Instr. Meth. B* **192**, 146.

Canter, K. F., Coleman, P. G., Griffith, T. C. & Heyland, G. R. (1972). *J. Phys. B* **5**, L167.

Canter, K. F., Mills, A. P. & Berko, S. (1975). *Phys. Rev. Lett.* **34**, 177.

Caradonna, P., Jones, A., Makochekanwa, C., Slaughter, D. S., Sullivan, J. P., Buckman, S. J., Bray, I. & Fursa, D. V. (2009). *Phys. Rev. A* **80**, 032710.

Cassidy, D. B. & Mills, A. P. (2007). *Nature* **449**, 195.

Chan, W. F., Cooper, G. & Brion, C. E. (1993a). *Chem. Phys.* **178**, 401.

Chan, W. F., Cooper, G., Sodhi, R. N. S. & Brion, C. E. (1993b). *Chem. Phys.* **170**, 81.

Charlton, M., Clark, G., Griffith, T. C. & Heyland, G. R. (1983). *J. Phys. B* **16**, L465.

Charlton, M. & Humberston, J. W. (2001). *Positron Physics*, chap. 1. Cambridge University Press, p. 20.

Charlton, M. & Laricchia, G. (1990). *J. Phys. B* **23**, 1045.

Chaudhuri, P. & Adhikari, S. K. (1998). *J. Phys. B* **31**, 3057.

Chen, Z. & Msezane, A. Z. (1994). *Phys. Rev. A* **49**, 1752.

Cheng, Y. & Zhou, Y. (2007). *Phys. Rev. A* **76**, 012704.

Cherry, W. H. (1958). *Secondary Electron Emission Produced from Surfaces by Positron Bombardment.* Ph.D. thesis, Princeton University.

Condon, E. (1926). *Phys. Rev.* **28**, 1182.

Cook, G. R. & Metzger, P. H. (1964). *J. Chem. Phys.* **41**, 321.

Cooke, D. A., Murtagh, D. J., Kövér, Á. & Laricchia, G. (2008). *Nucl. Instr. Meth. B* **266**, 466.

Cooke, D. A., Murtagh, D. J. & Laricchia, G. (2010a). *Phys. Rev. Lett.* **104**, 073201.

Cooke, D. A., Murtagh, D. J. & Laricchia, G. (2010b). *J. Phys. Conf. Ser.* **199**, 012006.

Deutsch, M. (1951). *Phys. Rev.* **82**, 455.

Diana, L. M., Coleman, P. G., Brooks, D. L., Pendleton, P. K., Norman, D. M., Seay, B. E. & Sharma, S. C. (1986). In: *Positron (Electron)–Gas Scattering* (Kauppila, W. E., Stein, T. S. & Wadehra, J. M., eds.). World Scientific.

Dimopoulou, C., Galassi, M. E., Moshammer, R., Rivarola, R. D., Fischer, D., Höhr, C. & Ullrich, J. (2005). *J. Phys. B* **38**, 3173.

Dirac, P. A. M. (1930). *Proc. Roy. Soc. Lond. A* **126**, 360.

Doering, J. P. (1964). *Phys. Rev.* **133**, A1537.

Dunlop, L. J. M. & Gribakin, G. F. (2006). *Nucl. Instr. Meth. B* **247**, 61.

Edwards, J. L. & Thomas, E. W. (1970). *Phys. Rev. A* **2**, 2346.

Eland, J. H. D. (1972). *Int. J. Mass Spec., Ion Phys.* **9**, 397.

Endt, P. M. & Kluyver, J. C. (1954). *Rev. Mod. Phys.* **26**, 95.

Fornari, L. S., Diana, L. M. & Coleman, P. G. (1983). *Phys. Rev. Lett.* **51**, 2276.

Franck, J. & Dymond, E. G. (1926). *Trans. Faraday Soc.* **21**, 536.

Fromme, D., Kruse, G., Raith, W. & Sinapius, G. (1986). *Phys. Rev. Lett.* **57**, 3031.

Furuya, K., Matsuo, A. & Ogawa, T. (2002). *J. Phys. B* **35**, 3077.

Gilbert, S. J., Kurz, C., Greaves, R. G. & Surko, C. M. (1997). *Appl. Phys. Lett.* 70, 1944.

Gilmore, S., Blackwood, J. E. & Walters, H. J. R. (2004). *Nucl. Instr. and Meth. B* **221**, 129.

Griffith, T. C. (1984). *Positron Scattering in Gases*. New York: Plenum, p. 53.

Guha, S. & Saha, B. C. (1980). *Phys. Rev. A* **21**, 564.

Harris, M. J., Share, G. H., Leising, M. D., Kinzer, R. L. & Messina, D. C. (1990). *Astrophys. J.* **362**, 135.

Hewitt, R. N., Noble, C. J. & Bransden, B. H. (1990). *J. Phys. B* **23**, 4185.

Hewitt, R. N., Noble, C. J. & Bransden, B. H. (1992). *J. Phys. B* **25**, 557.

Hoffman, K. R., Dababneh, M. S., Hsieh, Y. F., Kauppila, W. E., Pol, V., Smart, J. H. & Stein, T. S. (1982). *Phys. Rev. A* **25**, 1393.

Hutchins, S. M., Coleman, P. G., Stone, R. J. & West, R. N. (1986). *J. Phys. E* **19**, 282.

Hvelplund, P., Knudsen, H., Mikkelsen, U., Morenzoni, E., Møller, S. P., Uggerhøj, E. & Worm, T. (1994). *J. Phys. B* **27**, 925.

Igarashi, A. & Toshima, N. (1992). *Phys. Lett. A* **164**, 70.

Itikawa, Y. (2002). *J. Phys. Chem. Ref. Data* **31**, 749.

Itikawa, Y., Hayashi, M., Ichimura, A., Onda, K., Sakimoto, K., Takayanagi, K., Nakamura, M., Nishimura, H. & Takayanagi, T. (1986). *J. Phys. Chem. Ref. Data* **15**, 985.

Jacobsen, F. M., Frandsen, N. P., Knudsen, H., Mikkelsen, U. & Schrader, D. M. (1995). *J. Phys. B* **28**, 4691.

Jin, B., Miyamoto, S., Sueoka, O. & Hamada, A. (1994). *At. Coll. Res. Jap.* **20**, 9.

Jones, A. C. L., Caradonna, P., Makochekanwa, C., Slaughter, D. S., Sullivan, J. P., Buckman, S. J. & Mitroy, J. (2009). *J. Phys. Conf. Ser.* **194**, 072012.

Judge, D. L. & Lee, L. C. (1973). *J. Phys. B* **6**, 2150.

Kara, V. (1999). *Positron Impact Ionization Studies*. Ph.D. thesis, University College London.

Kara, V., Paludan, K., Moxom, J., Ashley, P. & Laricchia, G. (1997). *J. Phys. B* **30**(17), 3933–3949.

Kauppila, W. E., Miller, E. G., Mohamed, H. F. M., Pipinos, K., Stein, T. S. & Surdutovich, E. (2004a). *Phys. Rev. Lett.* **93**, 113401.

Kauppila, W. E., Stein, T. S., Miller, E. G. & Surdutovich, E. (2004b). *Nucl. Instr. Meth. B* **221**, 48.

Kernoghan, A. A., Robinson, D. J. R., McAlinden, M. T. & Walters, H. R. J. (1996). *J. Phys. B* **29**, 2089.

Khan, P., Mazumdar, P. S. & Ghosh, A. S. (1985). *Phys. Rev. A* **31**, 1405.

Knudsen, H., Kristiansen, H.-P. E., Thomsen, H. D., Uggerhøj, U. I., Ichioka, T., Møller, S. P., Hunniford, C. A., McCullough, R. W., Charlton, M., Kuroda, N., Nagata, Y., Torii, H. A., Yamazaki, Y., Imao, H., Anderson, H. H. & Tökesi, K. (2008). *Phys. Rev. Lett.* **101**, 043201.

Knudsen, H., Mikkelsen, U., Paludan, K., Kirsebom, K., Møller, S. P., Uggerhøj, E., Slevin, J., Charlton, M. & Morenzoni, E. (1995). *J. Phys. B* **28**, 3569.

Knudsen, H. & Reading, J. P. (1992). *Phys. Rep.* **212**, 107.

Krems, M., Zirbel, J., Thomason, M. & DuBois, R. D. (2005). *Rev. Sci. Instrum.* **76**, 093305.

Kwan, C. K., Kauppila, W. E., Nazaran, S., Przybyla, D., Scahill, N. & Stein, T. S. (1998). *Nucl. Instr. Meth. B* **143**, 61.

Laricchia, G., Armitage, S., Kövér, Á. & Murtagh, D. J. (2008). *Adv. At. Mol. Opt. Phys.*, vol. 56. Elsevier, pp. 1–47.

Laricchia, G., Brawley, S. J., Cooke, D. A., Kövér, Á., Murtagh, D. J. & Williams, A. (2009). *J. Phys. Conf. Ser.* **194**, 012036.

Laricchia, G., Charlton, M., Clark, G. & Griffith, T. C. (1985). *Phys. Lett. A* **109**(3), 97.

Laricchia, G., Charlton, M. & Griffiths, T. C. (1988). *J. Phys. B* **21**, L227.

Laricchia, G. & Moxom, J. (1993). *Phys. Lett. A* **174**, 255.

Laricchia, G., Moxom, J., Charlton, M. & Kövér, Á. (1994). *Hyperfine Interactions* **89**, 209.

Laricchia, G., Van Reeth, P., Szłuińska, M. & Moxom, J. (2002). *J. Phys. B* **35**, 2525.

Ley, R. (1997). *Hyperfine Interactions* **109**, 167.

Linstrom, P. J. & Mallard, W. G. (eds.) (2010). *NIST Chemistry WebBook, NIST Standard Reference Database Number 69*. Gaithersburg MD: National Institute of Standards and Technology.

Lofthus, A. & Krupenie, P. H. (1977). *J. Phys. Chem. Ref. Data* **6**, 113.

Mandal, P., Guha, S. & Sil, N. C. (1979). *J. Phys. B* **12**, 2913.

Mandal, P., Guha, S. & Sil, N. C. (1980). *Phys. Rev. A* **22**, 2623.

Marler, J. P., Sullivan, J. P. & Surko, C. M. (2005). *Phys. Rev. A* **71**, 022701.

Marler, J. P. & Surko, C. M. (2005). *Phys. Rev. A* **72**, 062713.

Massey, H. S. W. & Gilbody, H. B. (1974). *Electronic and Ionic Impact Phenomena Volume IV: Recombination and Fast Collisions of Heavy Particles*. Oxford University Press, pp. 2767–2788.

McAlinden, M. & Walters, H. (1992). *Hyperfine Interactions* **73**, 65.

Mills, A. P. (1981). *Phys. Rev. Lett.* **46**(11), 717.

Mills, A. P. & Gullikson, E. M. (1986). *Appl. Phys. Lett.* **49**(17), 1121.

Mitroy, J., Bromley, M. W. J. & Ryzhikh, G. G. (2002). *J. Phys. B* **35**, R81.

Mohorovičić, S. (1934). *Astron. Nachr.* **253**, 93.

Monce, M. N. (1988). *Phys. Rev. A* **38**, 3351.

Moores, D. I. (1998). *Nucl. Instr. Meth. B* **143**, 105.

Moores, D. I. (2001). *Nucl. Instr. Meth. B* **179**, 316.

Mori, S. & Sueoka, O. (1994). *J. Phys. B* **27**, 4349.

Moxom, J., Ashley, P. & Laricchia, G. (1996). *Can. J. Phys.* **74**, 367.

Murtagh, D. J., Arcidiacono, C., Pešić, Z. D. & Laricchia, G. (2006). *Nucl. Instr. Meth. B* **247**, 92.

Murtagh, D. J., Cooke, D. A. & Laricchia, G. (2009). *Phys. Rev. Lett.* **102**, 133202.

Murtagh, D. J., Szłuińska, M., Moxom, J., Van Reeth, P. & Laricchia, G. (2005). *J. Phys. B* **38**, 3857.

Nakatsuji, H. (1983). *Chem. Phys.* **75**, 425.

Ore, A. (1951). *Phys. Rev.* **83**, 665.

Ore, A. & Powell, J. L. (1949). *Phys. Rev.* **75**, 1696.

Orient, O. J. & Srivastava, S. K. (1987). *J. Phys. B* **20**, 3923.

Ottinger, C. & Simonis, J. (1978). *Chem. Phys.* **28**, 97.

Overton, N., Mills, R. J. & Coleman, P. G. (1993). *J. Phys. B* **26**, 3951.

Paludan, K., Laricchia, G., Ashley, P., Kara, V., Moxom, J., Bluhme, H., Knudsen, H., Mikkelsen, U., Møller, S. P., Uggerhøj, E. & Morenzoni, E. (1997). *J. Phys. B* **30**, L581.

Phelps, M. E., Hoffman, E. J., Mullani, N. A. & Ter-Pogossian, M. M. (1975). *J. Nucl. Med.* **16**, 210.

Przybyla, D., Addo-Asah, W., Kauppila, W. E., Kwan, C. K. & Stein, T. S. (1999). *Phys. Rev. A* **60**, 359.

Ralchenko, Y., Kramida, A. E., Reader, J. & NIST ASD Team (eds.) (2010). *NIST Atomic Spectra Database version 3.1.5*. Gaithersburg MD: National Institute of Standards and Technology.

Rapp, D. & Francis, W. E. (1962). *J. Chem. Phys.* **37**, 2631.

Ratnavelu, K. (1991). *Aust. J. Phys.* **44**, 265.

Rejoub, R., Lindsay, B. G. & Stebbings, R. F. (2002). *Phys. Rev. A* **65**, 042713.

Rich, A. (1981). *Rev. Mod. Phys.* **53**, 127.

Sarkar, N. K., Basu, M. & Ghosh, A. S. (1992). *Phys. Rev. A* **45**, 6887.

Schrader, D. M., Jacobsen, F. M., Frandsen, N. P. & Mikkelsen, U. (1992). *Phys. Rev. Lett.* **69**, 57.

Schultz, D. R. & Olson, R. E. (1988). *Phys. Rev. A* **38**, 1866.

Shah, M. B. & Gilbody, H. B. (1985). *J. Phys. B* **18**, 899.

Shah, M. B., McCallion, P. & Gilbody, H. B. (1989). *J. Phys. B* **22**, 3037.

Siegel, R. W. (1980). *Ann, Rev. Mater. Sci.* **10**, 393.

Solovyev, D., Sharipov, V., Labzowsky, L. & Plunien, G. (2010). *J. Phys. B* **43**, 2010.

Starrett, C. & Walters, H. J. R. (2008). *Nucl. Instr. Meth. B* **266**, 506.

Stein, T. S., Harte, M., Jiang, J., Kauppila, W. E., Kwan, C. K., Li, H. & Zhou, S. (1998). *Nucl. Instr. Meth. B* **143**, 68.

Straub, H. C., Lindsay, B. G., Smith, K. A. & Stebbings, R. F. (1996a). *J. Chem. Phys.* **105**, 4015.

Straub, H. C., Renault, P., Lindsay, B. G., Smith, K. A. & Stebbings, R. F. (1996b). *Phys. Rev. A* **54**, 2146.

Surko, C. M., Leventhal, M. & Passner, A. (1989). *Phys. Rev. Lett.* **62**, 901.

Szłuińska, M. & Laricchia, G. (2004a). *Nucl. Instr. and Meth. B* **221**, 107.

Szłuińska, M. & Laricchia, G. (2004b). *Nucl. Instr. Meth. B* **221**, 100.

Thomas, E. W., Bent, G. D. & Edwards, J. L. (1967). *Phys. Rev.* **165**, 32.

Tsurubuchi, S. & Iwai, T. (1974). *J. Phys. Soc. Jap* **37**, 1077.

Tóth, I., Campeanu, R. I., Chiş, V. & Nagy, L. (2006). *Phys. Lett. A* **360**, 131.

Utamuratov, R., Kadyrov, A. S., Fursa, D. V., Bray, I. & Stelbovics, A. T. (2010). *J. Phys. B* **43**, 125203.

Van Brunt, R. J. & Kieffer, L. J. (1975). *J. Chem. Phys.* **63**, 3216.

Van Reeth, P., Laricchia, G. & Humberston, J. W. (2005). *Physica Scripta* **71**, C9.

Van Reeth, P., Szłuińska, M. & Laricchia, G. (2002). *Nucl. Instr. Meth. B* **192**, 220.

Velotta, R., P. Di Giralamo, Berardi, V., Spinelli, N. & Armenante, N. (1994). *J. Phys. B* **27**, 2051.

Wheeler, J. A. (1946). *Ann. N. Y. Acad. Sci.* **48**, 221.

Wiley, W. C. & McLaren, I. H. (1955). *Rev. Sci. Instrum.* **26**, 1150.

Williams, A. (2009). Private communication.

Wilson, R. J. & Mills, A. P. (1983). *Phys. Rev. B* **27**, 3949.

Wrenn, F. R., L., G. M. & Handler, P. (1951). *Science* **113**, 525.

Simultaneous Ionization and Excitation of Molecules by Positron Impact

D. A. Cooke, D. J. Murtagh, and G. Laricchia

UCL Department of Physics and Astronomy, University College London, Gower Street, London, WC1E 6BT, United Kingdom

(Received 11 December 2009; published 19 February 2010)

Cross sections for ionization excitation of molecules by positron impact have been measured for the first time by scattering a positron beam from CO_2 and N_2. The cross sections have been observed to exceed those for electron impact by up to a factor of ~3 for CO_2 and ~5 for N_2. The enhancement arises primarily via positronium formation. The cross sections account for up to ~12% and 20% of the *total* cross sections for positron scattering from N_2 and CO_2, respectively.

DOI: 10.1103/PhysRevLett.104.073201 PACS numbers: 34.80.Uv, 36.10.Dr

The understanding of positron reactions with atoms and molecules remains a significant challenge, driven by the quest to advance fundamental knowledge of the underlying physical mechanisms, as well as to be able to control and to apply them. In this respect, ionization (including annihilation and Ps formation) is particularly pertinent, with examples ranging from damage limitation to healthy tissue during a scan employing β^+ emitters (or indeed targeting of tumors by the same means (e.g., [1]) to the investigation of the interstellar medium (e.g., [2]), and the solar atmosphere (e.g., [3]).

This Letter presents the first measurements of a cross section for positron-induced simultaneous ionization and excitation. CO_2 and N_2 have been investigated and, in each case, the cross section has been partitioned into direct ionization excitation and positronium (Ps) formation simultaneous with excitation. This work forms part of a broader study of positron-impact ionization phenomena of molecules, the other results of which will be reported elsewhere [4–6]. This study has also been motivated by the earlier observation of considerable γ-ray–UV photon coincidences following positron impact on CO_2 not arising from excited-state Ps formation [7]. The large magnitude of this signal led to the suggestion that it was the result of a channel-coupled mechanism [8,9], a phenomenon which had recently been identified in positron–O_2 collisions [10]. It was suggested that the proximity of the thresholds for the C state of CO_2 (reported as 10.56 eV) and for Ps formation leaving behind CO_2^+ ($A^2\Pi_u$) (reported as 10.50 eV) might account for the sizeable coincident signal seen between the γ ray from Ps annihilation and the UV photon resulting from the ionic deexcitation.

Details of the present experimental setup can be found in [11,12]; those elements specific to this work, along with a brief description, are outlined below and illustrated in Fig. 1. A beam of approximately 10^4 slow positrons s^{-1}, generated by moderating the fast β^+ output of a ^{22}Na source with an annealed W-mesh moderator, is constrained radially by a magnetic field of $\sim 10^{-2}$ T. By applying a positive potential V_m to the moderator, the peak energy of the beam can be varied according to $E_+ \approx eV_m + 2$ eV, as established by a retarding-potential analysis. This value is consistent with other determinations for W under similar non-UHV conditions, including the absolute determinations of 2.4 ± 0.1 eV [13] and 2.4 ± 0.3 eV [14] using time-of-flight methods. The transmission of unwanted components, for example, unmoderated positrons or secondary electrons, is substantially reduced by a Wien filter and a cylindrical electrode held at -500 V, the latter being grounded during measurements with electron projectiles which may be obtained by reversing the polarity of the moderator. In this way, measurements using either positrons or electrons may be taken without substantial modification to the apparatus.

The interaction region consists of a hemispherical polished aluminum gas cell. Ions are extracted from the cell perpendicularly to the beam axis using a lens held at -500 V and detected using a channel electron multiplier (CEM) with the cone held at -2800 V. Opposite this, a photomultiplier tube (PMT) mounted on an extension arm is used to detect low energy (200–600 nm) photons. Light guides coated with $Al + MgF_2$ line the interior of the extension arm; in conjunction with the polished surface of the gas cell, these serve to enhance photon collection. A borosilicate glass disc may be inserted in front of the PMT

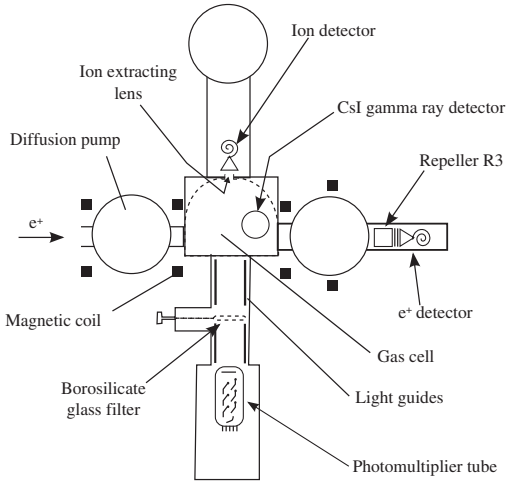

FIG. 1. Interaction region of the beam line showing the positioning of the detectors.

to block photons with wavelengths shorter than ~280 nm. A photodiode coupled to a CsI scintillation crystal used to detect γ rays is positioned above the gas cell. After the interaction region, the intensity of the positron beam is measured by a second CEM.

In the wavelength range of this study, the photons observable following collisions with CO_2 arise from the $A^2\Pi_u \rightarrow X^2\Pi g$ and $B^2\Sigma_u^+ \rightarrow X^2\Pi g$ transitions (293–438 and 288–289 nm, respectively [15]), in CO_2^+, while no transitions in the neutral molecule are reported in the same range [15,16]. The possibility of cascade from higher excited states of CO_2^+ may be disregarded as the $C^2\Sigma_g^+$ state is known to be fully predissociative [17] and excitations to higher states are also known to lead to dissociation [18]. Other transitions which may be detectable are $A^2\Pi \rightarrow X^2\Sigma^+$ in CO^+, formed by the dissociation of CO_2^+ and the $2P \rightarrow 1S$ transition from positronium formed in the $2P$ state. Based, respectively, on electron-impact data [19] and the earlier positron-impact study of [7], both these contributions are expected to be small. For N_2, only the $B^2\Sigma_u^+ \rightarrow X^2\Sigma_g^+$ (391.4 nm) transition in N_2^+ is visible together with the photon from the deexcitation of Ps. Unlike the case of CO_2, where the contribution from Ps($2P$) is inseparable from the $B^2\Sigma_u^+ \rightarrow X^2\Pi g$ transition, in N_2^+, it can be resolved using the borosilicate glass filter.

The present measurements of the simultaneous ionization excitation cross section (Q_i^{ex}) were performed by counting coincidences between the PMT and ion detector (henceforth, referred to as "photon–ion" coincidences) on a multichannel analyzer. Similarly, the partitioning of this cross section into contributions from direct ionization ($Q_i^{\mathrm{ex}/+}$) and positronium formation ($Q_i^{\mathrm{ex}/\mathrm{Ps}}$) was achieved using e^+-photon and γ-ray-photon coincidences, respectively. These, and the total ionization cross section (Q_i^t), were measured simultaneously, ensuring consistent normalization. The lifetimes of the $A^2\Pi_u$ and $B^2\Sigma_u^+$ states of CO_2^+ are 115 ± 5 ns and 126 ± 3 ns, respectively [20], and that of the $B^2\Sigma_u^+$ state of N_2^+ is 61.5 ± 1.1 ns [21], i.e., less than 1% of the ion extraction times (typically, ~20 μs), thus resulting in negligible loss of signal.

Generally, a cross section can be derived from a coincidence yield Y (that is, coincidences for the given process per incident positron) via Eq. (1):

$$Q_{\mathrm{process}} = \frac{1}{n\ell_{\mathrm{eff}}(\text{detection efficiencies})} Y_{\mathrm{process}} \qquad (1)$$

where n is the gas number density measured in the center of the cell and ℓ_{eff} is the effective cell length. The relevant efficiencies depend on which detectors are involved and, for these measurements, the methods employed are outlined below. Full details will be presented elsewhere [4]. The positron detection efficiency of the CEM ($\varepsilon_+ = 0.70 \pm 0.07$) was determined with the aid of an auxiliary detector (CsI) placed in close proximity and by taking the ratio of the number of γ-ray–e^+ coincidences (CsI + CEM) and of the γ-ray counts (CsI) recorded simultaneously. The ion extraction efficiency ($\varepsilon_{\mathrm{ext}} = 0.45 \pm 0.023$) was determined by performing a SIMION$^{\mathrm{TM}}$ simulation of the electric field permeating the gas cell with ions created at various positions along the cell while the detection efficiencies for these ions were derived from the work of [22]. The effective (i.e., including geometrical effects) detection efficiency of the CsI [$\varepsilon_{\mathrm{CsI}} = (6.24 \pm 0.05) \times 10^{-3}$] was measured by impinging an e^+ beam of known intensity upon a retractable annihilation plate. The quantum efficiency of the PMT photocathode as a function of wavelength was supplied by the manufacturer, ET Enterprises Ltd. The solid angle ($\Delta\Omega = 0.016 \pm 0.001$) subtended by the PMT was calculated by considering the active area of the photocathode. The enhancement to this ($C_r = 9.15 \pm 0.13$) due to the internal reflectors was determined by taking the ratio of identical photon–ion coincidence measurements with and without the mirrors. The areal density $n\ell_{\mathrm{eff}}$ was established by the normalization of Q_i^t for Ar (taken under identical conditions to the present measurements) to that of [23]. The normalization expressed by (1) was carried out via two separate methods: one was to apply the normalization constants determined as described above, the other method was to measure the equivalent electron cross section (where possible) using the same apparatus in order to extract an overall normalization constant and apply it to the positron data after correcting for differences between positron and electron measurements (e.g., in detection efficiencies, in operating pressure—electron measurements having been performed at lower pressures than positrons to retain single-collision conditions). The absolute scales achieved by the two methods have been found to be equal within the total statistical and systematic errors, the latter—amounting up to (+21, −19)%—being energy independent as arising from the overall uncertainty on the normalization [4]. Measurements were taken with the borosilicate glass filter both in and out to allow the separation of contributions from the $A^2\Pi_u \rightarrow X^2\Pi g$ and $B^2\Sigma_u^+ \rightarrow X^2\Pi g$ transitions in CO_2^+, and the separation of Ps($2P$) from $B^2\Sigma_u^+ \rightarrow X^2\Sigma_g^+$ in N_2^+. A summary of observable transitions for the two glass filter positions is presented in Table I. The mean transmission coefficient through borosilicate glass for each wavelength range was determined from CO_2^+

TABLE I. Visible transitions for each target gas. With the glass filter inserted, the transmission coefficients are given as premultipliers.

	Glass filter	
Target	In	Out
CO_2	CO_2^+ $0.85 \times A^2\Pi_u \rightarrow X^2\Pi g$	$A^2\Pi_u \rightarrow X^2\Pi g$
	CO_2^+ $0.22 \times B^2\Sigma_u^+ \rightarrow X^2\Pi g$	$B^2\Sigma_u^+ \rightarrow X^2\Pi g$
	CO^+ $0.90 \times A^2\Pi \rightarrow X^2\Sigma^+$	$A^2\Pi \rightarrow X^2\Sigma^+$
	Ps	$2P \rightarrow 1S$
N_2	$0.9 \times B^2\Sigma_u^+ \rightarrow X^2\Sigma_g^+$	$B^2\Sigma_u^+ \rightarrow X^2\Sigma_g^+$
	Ps	$2P \rightarrow 1S$

emission-spectra by electron impact [24] and borosilicate transmission curves (e.g., [25]). Note that the $A^2\Pi \rightarrow X^2\Sigma^+$ transition in CO^+ is inseparable from the $A^2\Pi_u \rightarrow X^2\Pi g$ transition in CO_2^+ by this method as the wavelength ranges (300–650 nm [26]) are almost entirely overlapping, so the transmission coefficients are effectively identical. However, it has been estimated from [19] that this should contribute $<10\%$ to the overall signal and is henceforth neglected in the present analysis. Separation of states in CO_2^+ may be achieved using simultaneous equations derived from glass-in and glass-out measurements (see Table I for coefficients); for N_2^+, the glass-in measurement corrected for the transmission coefficient provides the $B^2\Sigma_u^+ \rightarrow X^2\Sigma_g^+$ yield, while subtracting glass-in from glass-out allows estimation of the yield from Ps($2P$).

Figure 2(a) shows the measured cross section for total ionization (i.e., including Ps formation) simultaneous to ionic excitation $Q_i^{\mathrm{ex}/A}$ and $Q_i^{\mathrm{ex}/B}$ for positron impact on CO_2. Both cross sections peak at an energy significantly lower than corresponding electron cross sections, and ionization into the $A^2\Pi_u$ state is considerably enhanced over both the equivalent electron-impact cross section and the $B^2\Sigma_u^+$ state for positron impact; indeed, at its peak, it is approximately 20% of the *total* cross section [27]. Figures 2(b) and 2(c) show, respectively, the partitioning of this cross section into direct ionization and Ps formation components. From these, it is immediately apparent that Ps formation is exclusively responsible for the enhancement of ionization into the $A^2\Pi_u$ state of CO_2^+ by positron impact. This is corroborative evidence for the hypothesis of [8] (as discussed earlier) concerning Ps formation in CO_2 and is consistent with the observations of [28], which identified inner-shell Ps formation using $3\gamma/2\gamma$ ratio measurements.

Figure 2(d) shows a summary of ionization excitation measurements for the $B^2\Sigma_u^+ \rightarrow X^2\Sigma_g^+$ transition in N_2^+. In contrast to CO_2, the direct ionization process is more important for positrons than electrons—reflecting the situation with ionization without excitation [4,29]. However, the excess of Q_i^{ex} for positron impact over that for electron impact (a factor of ~ 5 around the peak) is again largely due to Ps formation. At its peak, Q_i^{ex} is approximately 12% of the corresponding total cross section [27].

For both targets, the contribution from Ps($2P$) appears to be small, unlike in the noble gases [30]. For N_2, it is separable, yielding an estimate for $Q_{\mathrm{Ps}}(2P)$ of $\sim(1.1 \pm 1.1) \times 10^{-17}$ cm^2, i.e., zero within experimental error. In the case of CO_2, it is mixed inseparably, in this work, with the signal from the $B^2\Sigma_u^+ \rightarrow X^2\Pi g$ transition.

The augmentation of Q_i^{ex} by positron impact over that by electron for these two molecules is clearly dominated by the contribution associated with Ps formation. This is over and above what would be expected from the partitioning of Q_i^t between Ps formation and direct ionization for the inert atoms [31] and, indeed, these two molecules [6]. As previously noted in [8], in the case of CO_2, there is an

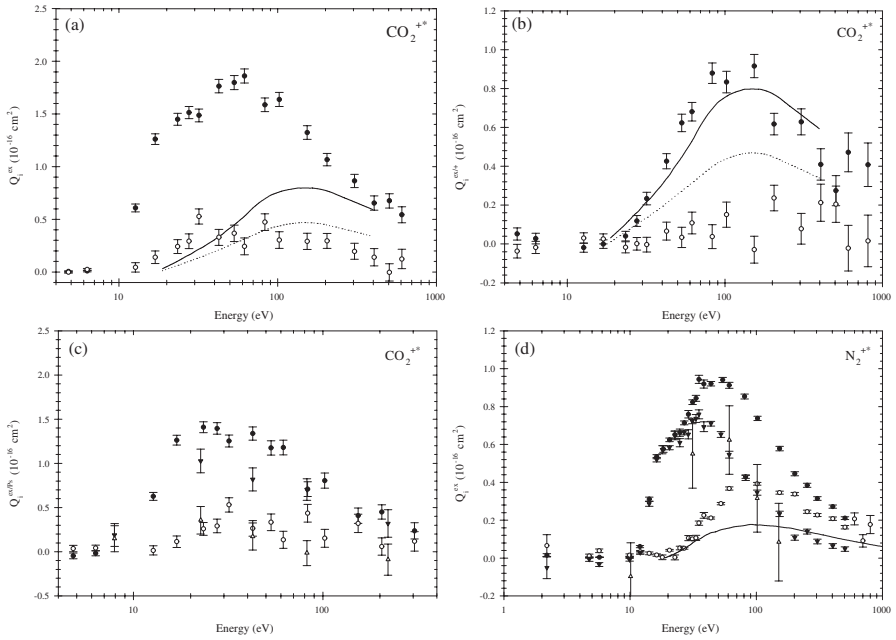

FIG. 2. Present measurements of Q_i^{ex} for CO_2 and N_2. (a) Q_i^{ex} for the $A^2\Pi_u \rightarrow X^2\Pi_g$ (●) and $B^2\Sigma_u^+ \rightarrow X^2\Pi_g$ (○) transitions in CO_2^+, compared with equivalent electron measurements of [24] (solid and dotted curves, respectively); (b) as (a), but for direct ionization; (c) as (a), but for Ps formation determined by using two methods: (i) the difference between Q_i^{ex} and $Q_i^{\mathrm{ex}/+}$ (● and ○) and (ii) γ-ray—photon coincidences (▼ and △); (d) Q_i^{ex} for the $B^2\Sigma_u^+ \rightarrow X^2\Sigma_g^+$ transition in N_2^+, showing the total (●), contributions from direct ionization (○) and Ps formation (determined as in (c)—▼ and △, respectively). The line corresponds to equivalent electron impact results [38]. There is an additional uncertainty of up to $(+21, -19)\%$ on the absolute scale of the present measurements due to the errors on the normalization.

extremely close energetic proximity for the excitation of the $^1\Sigma_u^+$ neutral state {10.30–11.28 eV (see, e.g., [32,33])} and the $A^2\Pi_u$ ionic state formed by Ps formation (10.52–11.22 eV, based on an ionization potential of 13.78 eV [34] and vibrational level assignments of [15,24]). Also, from the potential energy curves for N_2 [35], it is possible to deduce that a similar near degeneracy may exist between a number of neutral excited states ($b^1\Pi_u$, $b'^1\Sigma_u^+$, $c^1\Pi_u$, and $c'^1\Sigma_u^+$, over the energy range 12.50–13.95 eV [36]) and the ionic $B^2\Sigma_u^+$ state produced via Ps formation (at approximately 12.0 eV). Thus, for both targets, the enhancement of Q_i^{ex} might result from the coupling between two quasidegenerate channels: one the excitation of the neutral, the other of an ionic state induced by Ps formation. Indeed, since formation of ground state Ps lowers the ionic energy thresholds by 6.8 eV, an amount close to typical energy differences between excited molecular and ionic states, the ''accidental resonance'' between these excitations is likely to be a common feature of molecular ionization by positronium formation—the near-degeneracy made probable (in contrast with atoms) by the variation of the molecular interaction energy with internuclear distance and the fine energy-structure associated with vibrational and rotational excitations.

In addition to providing a hypothesis for the enhancement of the simultaneous Ps formation–excitation cross section, the accidental resonance described above may provide an explanation for the comparative dearth in N_2 of Ps formation in excited states, as corresponding binding energies (1.7 eV for $n = 2$) are too small to result in significant overlap of molecular states.

In conclusion, ionization excitation of CO_2 and N_2 is a more significant process for positron impact than for electrons. An examination of the potential energy curves ([35], for N_2) or energy levels (e.g., [33,37], for CO_2) for these molecules suggests that the positron may be able to excite the molecules quasiresonantly by coupling excited neutral and ionic states through Ps formation and, perhaps, allow the system to relax to the slightly lower energy configuration formed by Ps and an excited ionic state. Further experimental and theoretical work is anticipated.

We wish to thank Ann Orel and Jonathan Tennyson for useful discussions, Rafid Jawad and John Dumper for expert technical assistance, the Engineering and Physical Sciences Research Council for supporting this research.

[1] V. Caridad *et al.*, Cancer Biotherapy and Radiopharm. **23**, 371 (2008).
[2] N. Guessoum, P. Jean, and W. Gillard, Astron. Astrophys. **436**, 171 (2005).
[3] R. J. Murphy, G. H. Share, J. G. Skibo, and B. Kozlovsky, Astrophys. J. Suppl. Ser. **161**, 495 (2005).
[4] D. A. Cooke, D. J. Murtagh, and G. Laricchia (to be published).
[5] D. A. Cooke, D. J. Murtagh, and G. Laricchia, J. Phys. Conf. Ser. (to be published).
[6] G. Laricchia *et al.*, J. Phys. Conf. Ser. **194**, 012036 (2009).
[7] G. Laricchia, M. Charlton, and T. C. Griffiths, J. Phys. B **21**, L227 (1988).
[8] G. Laricchia and J. Moxom, Phys. Lett. A **174**, 255 (1993).
[9] G. Laricchia, J. Moxom, M. Charlton, Á. Kövér, and W. E. Meyerhof, Hyperfine Interact. **89**, 209 (1994).
[10] G. Laricchia, J. Moxom, and M. Charlton, Phys. Rev. Lett. **70**, 3229 (1993).
[11] D. A. Cooke, D. J. Murtagh, À. Kövér, and G. Laricchia, Nucl. Instrum. Methods Phys. Res., Sect. B **266**, 466 (2008).
[12] M. Szłuińska, P. Van Reeth, and G. Laricchia, Nucl. Instrum. Methods Phys. Res., Sect. B **192**, 215 (2002).
[13] V. Kara, Ph.D. thesis, University College London, 1999.
[14] M. Szłuińska and G. Laricchia, Nucl. Instrum. Methods Phys. Res., Sect. B **221**, 100 (2004).
[15] J. M. Ajello, J. Chem. Phys. **55**, 3169 (1971).
[16] M. Monce, Phys. Rev. A **38**, 3351 (1988).
[17] J. H. D. Eland, Int. J. Mass Spectrom. Ion Phys. **9**, 397 (1972).
[18] J. H. D. Eland and J. Berkowitz, J. Chem. Phys. **67**, 2782 (1977).
[19] K. Furuya, A. Matsuo, and T. Ogawa, J. Phys. B **35**, 3077 (2002).
[20] C. Herran, F. Arqueros, and J. Campos, J. Mol. Spectrosc. **97**, 244 (1983).
[21] F. Remy and M. A. Dumont, J. Quant. Spectrosc. Radiat. Transfer **20**, 217 (1978).
[22] M. Krems, J. Zirbel, M. Thomason, and R. D. DuBois, Rev. Sci. Instrum. **76**, 093305 (2005).
[23] G. Laricchia, P. Van Reeth, M. Szłuińska, and J. Moxom, J. Phys. B **35**, 2525 (2002).
[24] S. Tsurubuchi and T. Iwai, J. Phys. Soc. Jpn. **37**, 1077 (1974).
[25] http://www.atscope.com.au/photometry.html, 2009.
[26] J. M. Ajello, J. Chem. Phys. **55**, 3158 (1971).
[27] W. E. Kauppila and T. S. Stein, Adv. At. Mol. Opt. Phys. **26**, 1 (1990).
[28] W. E. Kauppila, E. G. Miller, H. F. M. Mohamed, K. Pipinos, T. S. Stein, and E. Surdutovich, Phys. Rev. Lett. **93**, 113401 (2004).
[29] H. Bluhme *et al.*, J. Phys. B **31**, 4631 (1998).
[30] D. J. Murtagh, D. A. Cooke, and G. Laricchia, Phys. Rev. Lett. **102**, 133202 (2009).
[31] G. Laricchia, S. Armitage, Á. Kövér, and D. J. Murtagh, Adv. At. Mol. Opt. Phys. **56**, 1 (2008).
[32] H. Nakatsuji, Chem. Phys. **75**, 425 (1983).
[33] W. F. Chan, G. Cooper, and C. E. Brion, Chem. Phys. **178**, 401, 1993.
[34] *NIST Chemistry Web-Book, NIST Standard Reference Database Number 69*, edited by P. J. Linstrom and W. G. Mallard (National Institute of Standards and Technology, Gaithersburg, MD, 2005).
[35] A. Lofthus and P. H. Krupenie, J. Phys. Chem. Ref. Data **6**, 113 (1977).
[36] W. F. Chan, G. Cooper, R. N. S. Sodhi, and C. E. Brion, Chem. Phys. **170**, 81 (1993).
[37] R. J. Buenker, M. Honigmann, H-P. Liebermann, and M. Kimura, J. Chem. Phys. **113**, 1046 (2000).
[38] W. L. Borst and E. C. Zipf, Phys. Rev. A **1**, 834 (1970).

Excited-State Positronium Formation from Helium, Argon, and Xenon

D. J. Murtagh, D. A. Cooke, and G. Laricchia

UCL Department of Physics and Astronomy, University College London, Gower Street, London WC1E 6BT, United Kingdom

(Received 19 December 2008; published 1 April 2009)

The cross sections for the formation of positronium in the $2P$ state in collisions of positrons with He, Ar, and Xe atoms have been determined by measuring coincidences between the remnant ion and the Lyman-α photon from positronium. The maximum fractional contributions of these to the total Ps formation cross sections increase from approximately 0.06 ± 0.01 in He to 0.12 ± 0.04 in Ar and 0.26 ± 0.09 in Xe. In the case of He, good agreement is found with a coupled-state calculation; for Ar and Xe, measurements are compared with a distorted-wave Born approximation.

DOI: 10.1103/PhysRevLett.102.133202 PACS numbers: 34.80.Uv, 36.10.Dr

Positronium (Ps) is the quasistable bound state of a positron (e^+) and an electron (e^-). It is readily formed in encounters of positrons with matter, and its own interactions with atoms and molecules (e.g., [1]), including its fragmentation [2,3] and even its combination with another Ps atom [4], are amenable to experimental investigations. Interest in positronium encompasses the quest for the understanding of fundamental matter-antimatter interactions (e.g., [5–7]), tests of collision physics theories (e.g., [8,9]) and bound-state QED calculations (e.g., [10]), the analysis of energetic events occurring in the Galactic center (where it is estimated 93% of all annihilations occur through the decay of Ps) [11], and problems of medical relevance [e.g. [12]].

Positronium is structurally equivalent to a hydrogen atom with half the reduced mass and thus Bohr energy levels ($E_n = -6.8\ \mathrm{eV}/n^2$). Its decay into m γ rays is governed by CP conservation according to $(-1)^m = (-1)^{L+S}$, where L and S are the Ps orbital and spin angular momenta, respectively. Thus ground-state para- (1^1S_0) and ortho- (1^3S_1) positronium decay dominantly into 2 and 3 γ rays, respectively, with corresponding lifetimes $\tau_\gamma \approx$ 125 ps and 143 ns. Those of the excited S states increase with n^3, while states with $L > 0$ are considerably longer lived due to their wave functions having a node at the origin, resulting in $\tau_\gamma(2P)$ being extended to (0.1–3) ms and the decay of $2P$ states being dominated by Lyman-α transitions ($\tau_\alpha \approx 3.2$ ns). Conversely, $2S \rightarrow 1S$ transitions by the emission of a single photon are forbidden, and, in the absence of perturbative forces, the intrinsic survival of the metastable $2S$ state is limited by annihilation.

The first unambiguous observation of excited-state positronium (Ps^*) was in the $2P$ state [13]. This was achieved by bombarding a room temperature Ge target with a slow positron beam ($E = 25$ and 40 eV) and by measuring the coincidences between an annihilation γ ray and the Lyman-α deexcitation photon ($\lambda = 243$ nm). A decade later, using a similar method, Ps^* was also observed in low density gases (namely, Ne, Ar, and H_2) formed by positron projectiles of a few tens of eV [14]. While formation cross sections for Ps in the $2S$ and $2P$ states have been theoretically calculated for H (e.g., [15]), He [16–20], and the noble gases [21], experimental determinations have been lacking until now. It was recently considered that structure observed in the total positronium formation cross section (Q_{Ps}) for the heavier noble gases might be due to Ps^* [22–24], and estimates were made which inferred increasing contributions from Ps^* to Q_{Ps} as the target atomic number was increased from He to Xe [22]. However, discrepancies exist on the magnitude [25] and the conjectured physical origin [24,26] of this structure.

In the present work, coincidences between the residual ion and the deexcitation photon from Ps^* have been measured in order to determine Q_{Ps^*} for the first time. In comparison with the previous work [14], the present method has the advantage that, by detecting ions rather than annihilation quanta, the signal can be easily enhanced by focusing onto a detector and a number of now-well-known systematic effects [27] are avoided. Helium, argon, and xenon targets have been chosen to test available theories as well as the hypothesis of Ref. [22].

The experimental apparatus generating the beam of low energy positrons ($\Delta E \sim 2$ eV) has been described in detail elsewhere [28,29]. Briefly, fast β^+ emitted from a ^{22}Na source are moderated by annealed W meshes. The slow positrons are radially confined by a magnetic field ($\vec{B} \approx$ 100 G) along the length of the beam line and pass through a bent solenoid, an electron repeller, and a Wien filter in order to reduce the number of unwanted γ rays, secondary electrons, and fast positrons transported to the interaction region. A positively biased electrode may be used to repel the slow portion of the beam, allowing measurement of the background produced by the remaining particles. The interaction region is a hemispherical gas cell constructed from polished Al. A small electrostatic lens held at -500 V extracts ions from the cell towards the detector, consisting of a channel electron multiplier (CEM) housed in a separately pumped chamber. A photomultiplier tube (PMT) with sensitivity in the range $200\ \mathrm{nm} \leq \lambda \leq 600$ nm is mounted on an extension arm in order to remove it from the beam-guiding magnetic field. The extension arm is lined with UV reflectors, consisting of glass tubes

coated with Al + MgF_2. A removable borosilicate glass disk may be inserted in front of the PMT to reduce its sensitivity range to 280 nm $\leq \lambda \leq$ 600 nm. Measurements of ion-photon coincidences are performed with and without the glass filter. The difference between the two measurements therefore corresponds to the detection of photons with wavelengths of 200 nm $\leq \lambda \leq$ 280 nm. The positron beam intensity is monitored by another CEM at the end of the flight path. Two ^{22}Na sources were used ($\sim$5 and 50 mCi); for He and Ar, the measured beam intensity was typically $\sim 10^3$ s^{-1}, whereas for Xe, the stronger source yielded $\sim 10^4$ s^{-1}.

The total ion yield (Y_i) is given by

$$Y_i(E) = \frac{N_i - B_i}{N_+ - B_+}, \quad (1)$$

where N_i and N_+ refer, respectively, to the ion and incident beam rates and $B_{i,+}$ represent the associated backgrounds measured by biasing off the slow portion of the beam. Y_i is directly proportional to the total ionization cross section:

$$Q_i^t = \sum Q_x = \frac{1}{\rho l_{\text{eff}}} \frac{\epsilon_+}{\epsilon_i} Y_i, \quad (2)$$

where Q_x is the cross section for any ion-producing process, i.e., Ps formation, direct ionization, annihilation, etc. (e.g., [30]), ρ is the target number density, l_{eff} is the effective length of the cell, ϵ_+ is the detection efficiency for positrons, and ϵ_i that for the ions, the latter comprising that for extraction.

The yield of Ps* is accordingly given by

$$Y_{\text{Ps}^*} = \frac{(N_{\text{go}} - B_{\text{go}}) - (N_{\text{gi}} - B_{\text{gi}})}{N_+ - B_+}, \quad (3)$$

where N_{go} is the coincidence rate obtained without the glass filter and by integrating the ion time-of-flight (TOF) spectra over the region corresponding to the desired charge-to-mass ratio, N_{gi} that with the filter inserted, and $B_{\text{go,gi}}$ the associated random backgrounds determined from a flat portion of the TOF spectra. The beam-off backgrounds were found to be negligible for the coincidence measurements.

The cross section for the formation of excited-state positronium Q_{Ps^*} is then determined according to

$$Q_{\text{Ps}^*} = \left(\frac{1}{\rho l_{\text{eff}}} \frac{\epsilon_+}{\epsilon_i}\right)\left(\frac{1}{C_r} \frac{4\pi}{\Delta\Omega}\right)\left(\frac{1}{\epsilon_{\text{PMT}}}\right) Y_{\text{Ps}^*}, \quad (4)$$

where $\Delta\Omega = (0.0164 \pm 0.0004)$ sr is the solid angle subtended by the PMT; $C_R = (2.40 \pm 0.22)$ corresponds to the enhancement of the photon collection due to the UV reflectors (determined by performing measurements without the light guides and the cell blackened with graphite), and ϵ_{PMT} is the quantum efficiency of the PMT [$\sim(20 \pm 2)$% at $\lambda < 280$ nm] (Electron Tubes LTD.). Y_i is measured simultaneously and allows the determination of the first term using Eq. (2) and Q_i^t from Ref. [29] for He and Ref. [22] for Ar and Xe.

Contributions to the present measurements from Ps states other than the $2P$ have been considered and will be discussed in detail elsewhere [31]. Briefly, they may originate from perturbations of the metastable $2S$ state or from states with $n > 2$. Lyman-α deexcitation from the $2S$ state may occur via Stark mixing or collisional deexcitation. The former may be induced by the static electric field from the ion extraction lens and by the motion of the Ps transversely to the guiding magnetic field [32]. Collisional deexcitation of the $2S$ via $2P$ state has been evaluated using the cross section recently calculated in Refs. [33,34] together with a Bohr-scaled total cross section, i.e., $Q_t \propto n^4$. In combination, these effects imply a contribution from the $2S$ state to the measured signal in the range of $\sim$(1–3)%. Using an isotropic distribution instead of the shape of the differential cross section for ground-state Ps formation [35] to estimate the average Ps* velocity perpendicular to the B field, the overall contribution from Stark-quenched Ps($2S$) increases by less than 1%.

The possibility of detection of states with $n > 2$, either directly (i.e., $3P \rightarrow 1S$) or via cascade from $n > 2$ via $2P$ (e.g., $3D \rightarrow 2P$) has been estimated by calculating the deexcitation probability before a collision occurs (assumed for $n > 2$ to result in breakup with unit probability, as in the case of H scattering [36,37]) and weighting this by $1/n^3$, taken as a measure of the formation probability into higher n states [19,24]. Overall, the contribution arising from states with $n > 2$ is assessed to be again of the order of a few percent. Decreasing the probability of fragmentation of Ps($n > 2$) from unity to 50% [as is the case for Ps($n = 1$)] (e.g., [30]) gives a contribution of $<$5% for all targets. Thus states other than $2P$ are expected to contribute $<$10% to the present measurement. Henceforth, the measured cross section shall be referred to as $Q_{\text{Ps}}(2P)$.

The results are presented in Figs. 1–3 for He, Ar, and Xe, respectively. The error bars shown in these figures comprise the statistical errors on the yields and the $\pm$14% overall uncertainty on the normalization factors in Eq. (4). Above each figure is the percentage contribution to the total (all n) Q_{Ps} (shown in the inset) [22,29]. In the case of He, $Q_{\text{Ps}}(2P)$ rises from the threshold at 22.9 eV reaching a maximum of $(2.6 \pm 0.6) \times 10^{-18}$ cm^2 at an energy around 40 eV. The cross section decays rapidly after 50 eV towards zero (within errors) at 100 eV. The maximum contribution to Q_{Ps} (all n) [29] may be seen in the figure to be (6 ± 1)%. For Ar, $Q_{\text{Ps}}(2P)$ increases from the threshold at 14.1 eV and peaks near 40 eV with a magnitude of $(2.2 \pm 0.5) \times 10^{-17}$ cm^2, reducing to zero within errors by 140 eV. In this case, the maximum contribution to Q_{Ps} is (12 ± 4)%. Finally, in the case of Xe, the experimental $Q_{\text{Ps}}(2P)$ rises from the threshold at 10.4 eV and peaks at approximately 23 eV with a magnitude of $(1.4 \pm 0.5) \times 10^{-16}$ cm^2 decaying rapidly after 25 eV. For Xe, Ps($2P$) contributes a maximum of (26 ± 9)% to Q_{Ps} [22]. Note that, for Ar and Xe, the uncertainties on the percentage contributions for the higher energy points are too large for the values to be meaningful.

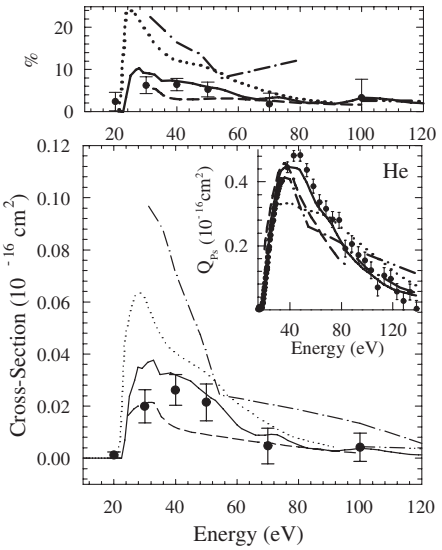

FIG. 1. The present $Q_{Ps}(2P)$ for He (circles) compared with available theories: solid curve, Ref. [19]; dotted line, Ref. [20]; chain curve, Ref. [16]; dashed curve, Ref. [17]; double chain curve, Ref. [18]. The error bars include the statistical errors on the yields and the uncertainties on the normalization factors. Above the main figure is the percentage contribution of $Q_{Ps}(2P)$ to the Q_{Ps}(all n) of Ref. [29]. In the inset, Q_{Ps}(all n) are displayed: circles, Ref. [29]; lines, as in main figure.

Included in Figs. 1–3 are corresponding available theories. For He, they comprise the coupled-state calculation of Ref. [19], the close-coupling calculations of Refs. [17,20], the distorted-wave approach of Ref. [16], and from 100 eV, the second Born approximation of Ref. [18]. In Fig. 1, the theories exhibit a similar energy dependence to one another, all peaking at ~35 eV, somewhat earlier than experiment, then decreasing rapidly above 50 eV. There are, however, significant differences in absolute magnitude among them, and the best agreement is found between the present results and the elaborate calculation of Ref. [19], as was also the case between their Q_{Ps}(all n) and the most recent experimental determination [29] (see inset). The results of the close-coupling approximation calculations of Refs. [17,20] are, respectively, a factor of 2 and 3 higher in magnitude at their peak than the experimental $Q_{Ps}(2P)$.

The measurements for Ar and Xe are compared with a distorted-wave Born approximation (DWBA) calculation [21]. In Fig. 2, the theoretical results for Ar may be seen to peak earlier than experiment, undercutting it by ~35% between energies of 40 and 100 eV. Finally, in the case of Xe (Fig. 3), there is a broad agreement in shape and magnitude between theory and experiment although the experimental $Q_{Ps}(2P)$ is on average higher around the peak region. Concerning Q_{Ps} (all n) for these targets, the DWBA calculation of Ref. [24] exceeds experimental measurements [22] by approximately factors of 2 and 3 (see insets).

Figure 4 compares upper and lower limit estimates of $Q_{Ps}(n > 1)$ [22] with the results of the DWBA and the present measurements of $Q_{Ps}(2P)$. In the case of Ar, the measured $Q_{Ps}(2P)$ accounts for approximately 1/3 of the lower limit estimate of $Q_{Ps}(n > 1)$, while for Xe they are of a similar magnitude around the peak region.

Detection of the fluorescence of the ion (i.e., from simultaneous excitation-Ps formation or ionization) is possible above the thresholds for transitions resulting in photons of wavelengths in the range 200 nm $\leq \lambda \leq$ 280 nm. These thresholds, corresponding to $E_{sim} = I - 6.8$ eV + E_{ex} (I being the ionization energy of the ground-state target atom, 6.8 eV the binding energy of ground-state Ps, and E_{ex} the relevant excitation energy of the ion), are approximately 58.6 eV for He, 30.1 eV for Ar, and 21.3 eV for

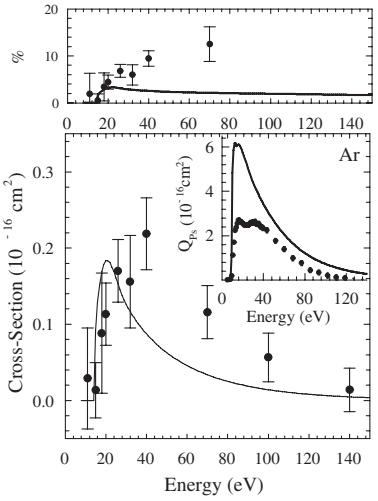

FIG. 2. The present $Q_{Ps}(2P)$ for Ar (circles) compared with theory [21] (line). Error bars as per Fig. 1. Above the main figure is the percentage contribution of $Q_{Ps}(2P)$ to the Q_{Ps} (all n) of Ref. [22] compared with the corresponding calculation [21,24]. In the inset, Q_{Ps} (all n) are displayed: circles, Ref. [22]; lines, Refs. [21,24].

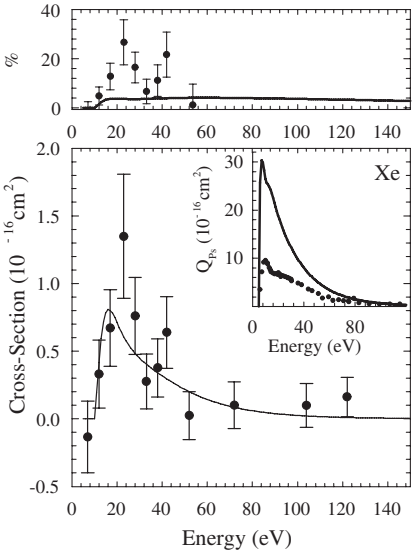

FIG. 3. As per Fig. 2 but for Xe.

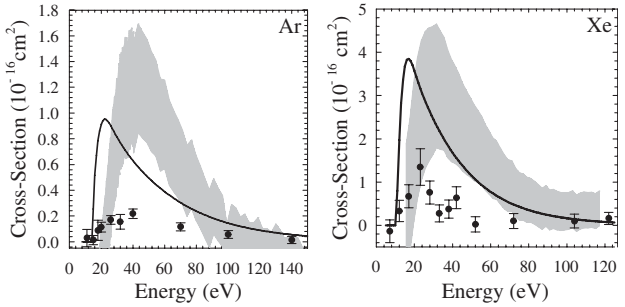

FIG. 4. Present $Q_{Ps}(2P)$ for Ar and Xe (circles), the limits of $Q_{Ps}(n > 1)$: gray region, Ref. [22]; line, DWBA results [24].

Xe [38]. Thus, the said type of contribution, which in the case of CO_2 peaks at around 4 times the threshold energy and remains significant ($\approx$30% of its maximum) at $\sim$0.5 keV [39], may be expected to be negligible in the observed signal. In the case of Xe, explicit measurements of positron-photon coincidences (corresponding to simultaneous excitation ionization) were also performed and found to be zero within errors.

In conclusion, the first measurements of $Q_{Ps}(2P)$ have been presented for He, Ar, and Xe targets. The results for He are in good agreement with the coupled-state calculation of Ref. [19], and there is broad agreement between the experimental $Q_{Ps}(2P)$ for Xe and the DWBA of Ref. [21], while for Ar experiment exceeds theory. As discussed above, however, a large discrepancy exists between theory and experiment in the case of Q_{Ps} (all n) for these two targets. The contributions of $Q_{Ps}(2P)$ to the total Ps formation cross sections are found to increase from approximately 0.06 ± 0.01 in He to 0.12 ± 0.04 in Ar and 0.26 ± 0.09 in Xe, in qualitative agreement with the estimates of Ref. [22].

Further attention from theory to both integral and differential state-resolved Q_{Ps} would seem warranted. Possible experimental investigations of metastable Ps states and molecular targets are being considered.

We thank H. R. J. Walters and C. Starrett for sending us their results prior to publication, them and A. Crowe for valuable discussions, J. Dumper and R. Jawad for technical support, and EPSRC for funding this research.

[1] A. J. Garner, G. Laricchia, and A. Ozen, J. Phys. B **29**, 5961 (1996); N. Zafar *et al.*, Phys. Rev. Lett. **76**, 1595 (1996); D. E. Leslie, S. Armitage, and G. Laricchia, J. Phys. B **35**, 4819 (2002); J. Beale, S. Armitage, and G. Laricchia, J. Phys. B **39**, 1337 (2006); M. Skalsey *et al.*, Phys. Rev. A **67**, 022504 (2003); H. Saito and T. Hyodo, Phys. Rev. Lett. **97**, 253402 (2006).
[2] S. Armitage *et al.*, Phys. Rev. Lett. **89**, 173402 (2002).
[3] S. Brawley *et al.*, Nucl. Instrum. Methods Phys. Res., Sect. B **266**, 497 (2008).
[4] D. B. Cassidy and A. P. Mills, Phys. Rev. Lett. **100**, 013401 (2008).
[5] G. Gabrielse *et al.*, Phys. Lett. B **548**, 140 (2002).
[6] A. Speck *et al.*, Phys. Lett. B **597**, 257 (2004).
[7] M. H. Holzscheiter, M. Charlton, and M. M. Nieto, Phys. Rep. **402**, 1 (2004).
[8] C. Starrett, M. T. McAlinden, and H. R. J. Walters, Phys. Rev. A **72**, 012508 (2005).
[9] A. S. Ghosh *et al.*, Phys. Rev. A **63**, 042706 (2001).
[10] M. Barham and J. W. Darewych, J. Phys. B **41**, 185001 (2008).
[11] G. Bélanger *et al.*, Astrophys. J. **636**, 275 (2006).
[12] C. Champion and C. L. Loirec, Phys. Med. Biol. **51**, 1707 (2006).
[13] K. F. Canter, A. P. Mills, and S. Berko, Phys. Rev. Lett. **34**, 177 (1975).
[14] G. Laricchia *et al.*, Phys. Lett. **109A**, 97 (1985).
[15] A. A. Kernoghan *et al.*, J. Phys. B **29**, 2089 (1996).
[16] P. Khan, P. S. Mazumdar, and A. S. Ghosh, Phys. Rev. A **31**, 1405 (1985).
[17] R. N. Hewitt, C. J. Noble, and B. H. Bransden, J. Phys. B **25**, 557 (1992).
[18] N. K. Sarkar, M. Basu, and A. S. Ghosh, Phys. Rev. A **45**, 6887 (1992).
[19] C. P. Campbell *et al.*, Nucl. Instrum. Methods Phys. Res., Sect. B **143**, 41 (1998).
[20] P. Chaudhuri and S. K. Adhikari, J. Phys. B **31**, 3057 (1998).
[21] S. Gilmore, Ph.D. thesis, Queen's University Belfast, 2004.
[22] G. Laricchia *et al.*, J. Phys. B **35**, 2525 (2002).
[23] M. Szłuińska, P. Van Reeth, and G. Laricchia, J. Phys. B **35**, 4059 (2002).
[24] S. Gilmore, J. E. Blackwood, and H. R. J. Walters, Nucl. Instrum. Methods Phys. Res., Sect. B **221**, 129 (2004).
[25] J. P. Marler, J. P. Sullivan, and C. M. Surko, Phys. Rev. A **71**, 022701 (2005).
[26] L. J. M. Dunlop and G. F. Gribakin, Nucl. Instrum. Methods Phys. Res., Sect. B **247**, 61 (2006).
[27] M. Charlton and G. Laricchia, J. Phys. B **23**, 1045 (1990).
[28] J. Moxom, G. Laricchia, and M. Charlton, J. Phys. B **28**, 1331 (1995).
[29] D. J. Murtagh *et al.*, J. Phys. B **38**, 3857 (2005).
[30] G. Laricchia *et al.*, in *Advances in Atomic, Molecular, and Optical Physics*, edited by E. Arimondo, P. Berman, and C. Lin (Elsevier, New York, 2008), Vol. 56.
[31] D. J. Murtagh *et al.* (to be published).
[32] S. M. Curry, Phys. Rev. A **7**, 447 (1973).
[33] H. R. J. W. C. Starrett and M. McAlinden, Nucl. Instrum. Methods Phys. Res., Sect. B **266**, 506 (2008).
[34] C. Starrett and H. R. J. Walters, Nucl. Instrum. Methods Phys. Res., Sect. B **266**, 3221 (2008).
[35] M. T. McAlinden and H. R. J. Walters, Hyperfine Interact. **89**, 407 (1994).
[36] J. L. Edwards and E. W. Thomas, Phys. Rev. A **2**, 2346 (1970).
[37] D. R. Bates and J. C. G. Walker, Planet. Space Sci. **14**, 1367 (1966).
[38] Using National Institute of Standards and Technology Atomic Spectra Database data for the lowest energy excited ionic state radiating a photon in the sensitivity range.
[39] D. A. Cooke *et al.* (to be published).

Journal of Physics: Conference Series **199** (2010) 012006 doi:10.1088/1742-6596/199/1/012006

Positronium formation cross-sections for Xe, CO_2 and N_2

D A Cooke, D J Murtagh and G Laricchia

UCL, Department of Physics and Astronomy, University College London, Gower Street, London, WC1E 6BT, UK

E-mail: g.laricchia@ucl.ac.uk

Abstract. The positronium formation cross-sections for Xe, CO_2 and N_2 have been measured using coincidences between γ-rays from positronium self-annihilation and the resultant ion. In the case of Xe, there is excellent agreement with previous experimental determinations. For CO_2 there is broad agreement in magnitude with previous measurements in contrast with N_2 where good shape agreement at low energies (< 40 eV) is found though the magnitude of the present cross-section is significantly higher.

1. Introduction

When considering ionization by positron impact, there are two dominant channels: direct ionization ($e^+ + A \rightarrow A^+ + e^+ + e^-$) and positronium (Ps) formation ($e^+ + A \rightarrow A^+ + Ps$). For an atomic target, the total ionization cross-section (Q_i^t) is defined as the sum of the Ps formation (Q_{Ps}) and direct ionization (Q_i^+) cross-sections, contributions from higher order processes and from direct annihilation of a target electron are considered generally negligible [1]. This is illustrated in figure 1, which shows the partitioning of Q_i^t for He into contributions from Q_i^+ and Q_{Ps}. In the case of a molecular target, the dissociative ionization cross-section ($Q_i^{\rm diss}$) must also be included in the sum for Q_i^t.

Recently, there have been experimental determinations of Q_{Ps} for the noble gases [e.g. 2, 3] and the first experimental measurements of Ps formation into the $2P$ state ($Q_{Ps}(2P)$) for He, Ar and Xe [4]. With the exception of He, there have been fewer theoretical determinations of Q_{Ps}, however, there are a number of cross-sections for excited-state Ps formation [e.g. 5, 6] and Ps formation from inner-shell electrons [e.g. 6–8].

Figure 2 shows the available experimental determinations of Q_{Ps} and $Q_{Ps}(2P)$ for Xe compared with theory. There is a large distribution of magnitudes and shapes when considering all determinations. There is, however, convergence between two recent measurements, those of [2] and [3]. The determination of [16], measured using γ-ray–ion coincidences, reproduces the structure observed by [2] in energy dependence only—an absolute scale was set by normalizing the coincidence yield to this previous determination. These measurements also suffered from a systematic effect at high energies ($E > 16$ eV) whereby the magnetic field failed to contain scattered projectiles, yielding an excess of γ-rays from annihilation on the cell walls.

In the present work, γ-ray–ion coincidences have been used to measure Q_{Ps} for Xe, N_2 and CO_2 with particular attention paid to confining all positrons after scattering. Unlike previous work [15], an absolute scale has been set on these measurements using Q_i^t. For Xe, there is good agreement between all determinations [see e.g. 17]; for the molecules, a concurrent measurement of Q_i^t for Ar was used for normalization.

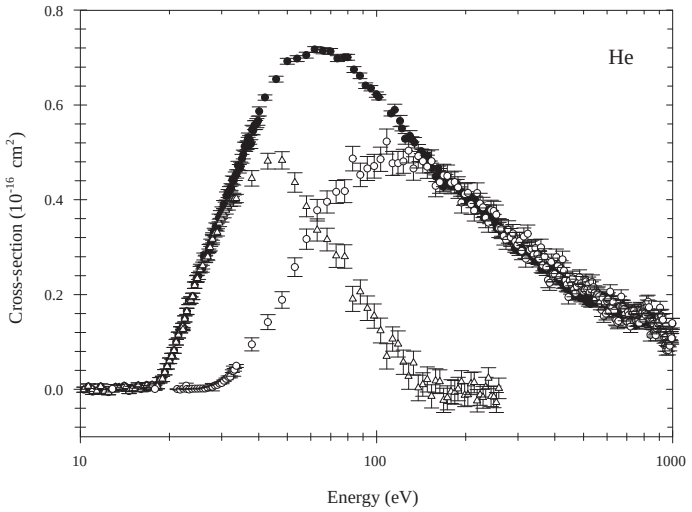

Figure 1. Partitioning of Q_i^t (●) of He into Q_i^+ (○) and Q_{Ps} (△). Data from [9–11].

2. Experimental Method

The experimental apparatus used in the present work is shown in figure 3 and has been described in detail elsewhere [18, 19]. Briefly, fast β^+ particles emitted from a ^{22}Na source are moderated by annealed W meshes producing a slow positron beam with $\Delta E \sim 2$ eV. The slow positrons are radially confined by a magnetic field ($\vec{B} \approx 100$ G) along the length of the beam-line (see black squares in figure 3). The beam passes through a bent solenoid, an electron repeller (repeller R1 in figure 3) and a Wien filter in order to reduce the number of unwanted γ-rays, secondary electrons and fast positrons transported to the interaction region. A positively-biased electrode (repeller R2 in figure 3) may be used to repel the slow portion of the beam, allowing measurement of the background produced by the remaining particles. The interaction region is a hemispherical gas cell constructed from polished Al. A small electrostatic lens held at -500 V extracts ions from the cell towards the detector, which consists of a channel electron multiplier (CEM) housed in a separately-pumped chamber. A CsI γ-ray detector is placed directly on top of the interaction region to detect annihilation quanta from the cell, and a second CEM is positioned at the end of the beamline for the detection of positrons. The photomultiplier tube mounted on an extension arm was used for the determination of $Q_{Ps}(2P)$.

The measurements were normalized by recording the total ion yield (Y_i)[1] simultaneously with the γ-ray–ion coincidence yield. Y_i is proportional to Q_i^t via:

$$Q_i^t = \frac{1}{nl}\frac{\varepsilon_+}{\varepsilon_i} Y_i \tag{1}$$

where n is the number density of the target gas, l is the effective cell length and ε refers to a detector efficiency. This normalization is performed similarly to that for Q_i^+ in [18], and allows the determination of $\frac{1}{nl}\frac{\varepsilon_+}{\varepsilon_i}$ for use in other normalizations. The error on this method is approximately $\pm 5\%$ [20]. The γ-ray–ion coincidence yield can then be normalized relative to the ion yield by correcting for the CsI detector efficiency which has been measured as 0.010 ± 0.001. This places an additional $\pm 10\%$ error on the absolute scale of the measured cross-sections.

[1] Yield is defined as event per positron recorded

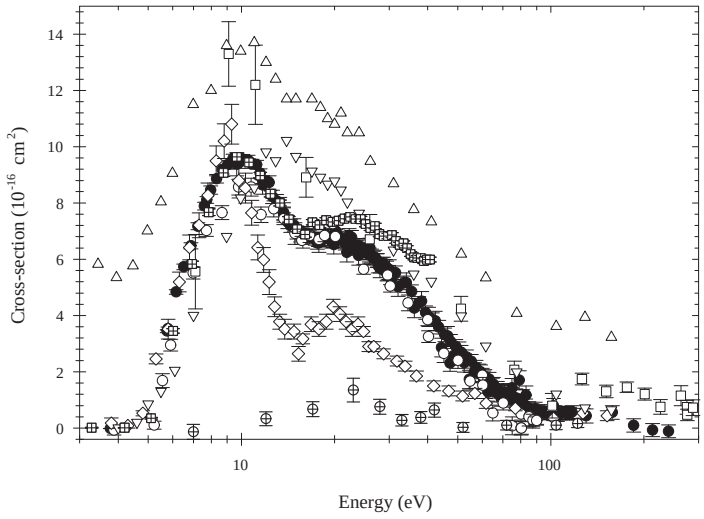

(a)

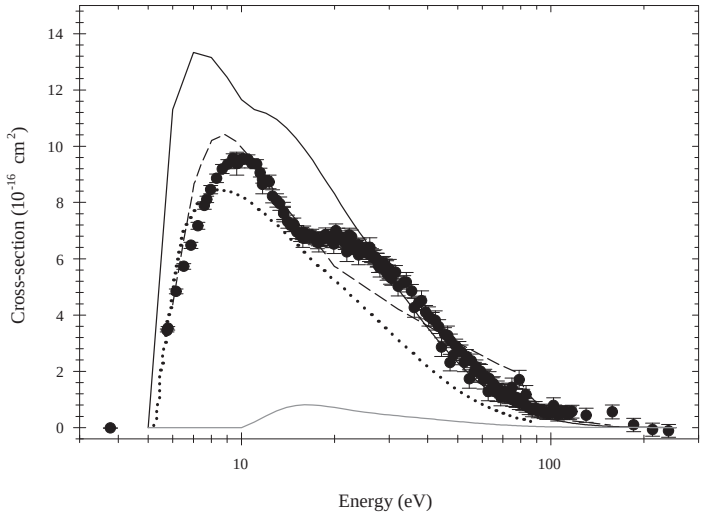

(b)

Figure 2. Review of experimental and theoretical determinations of Q_{Ps} for Xe. 2(a), experimental: ●—[2], ○—[3], ◇—[12], □—[13], ▽ and △—lower and upper limits of [14] respectively, ⊞—[15], ⊕—$Q_{Ps}(2P)$ [4]. 2(b), theoretical: solid line—[6]×0.5, dashed line—[7]×0.5, dotted line—[8], solid grey line—$Q_{Ps}(2P)$ [6], ●—as 2(a).

3. Results

Figures 4, 5 and 6 show Q_{Ps} for Xe, CO_2 and N_2, respectively. In the case of Xe (figure 4), the present determination of Q_{Ps} peaks at ∼10 eV with a magnitude of $8.9 \pm 0.3 \times 10^{-16}$ cm^2. A shoulder feature is observed between ∼14 eV and 24 eV with the cross-section becoming negligible after ∼100 eV. In comparison with other determinations of Q_{Ps}, there is excellent agreement, within errors, between the present results and those of [2] and [3].

Figure 5 shows the present Q_{Ps} for CO_2 compared with other experimental measurements. The present results peak at ∼23 eV with a magnitude of $4.1 \pm 0.1 \times 10^{-16}$ cm^2 and extend to 750 eV. In

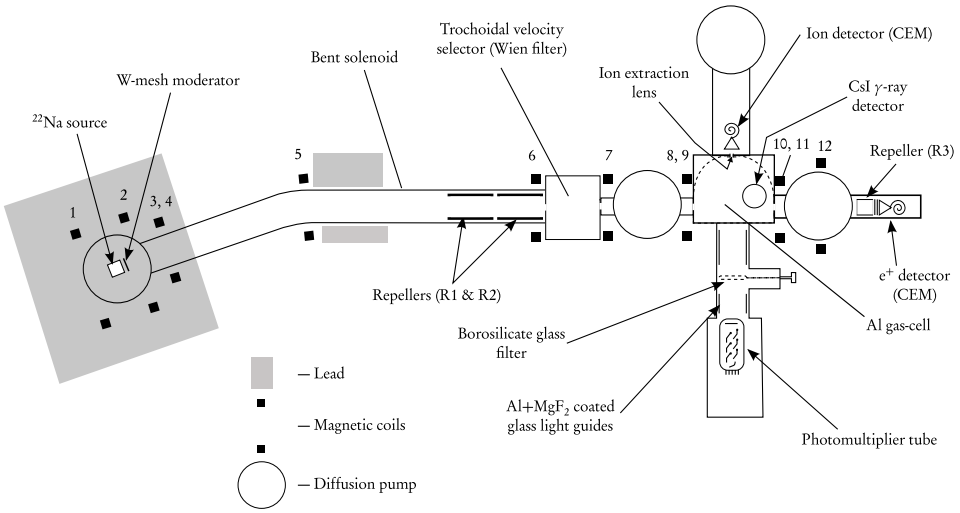

Figure 3. The magnetically guided positron beam and interaction region, showing the placement of various detectors.

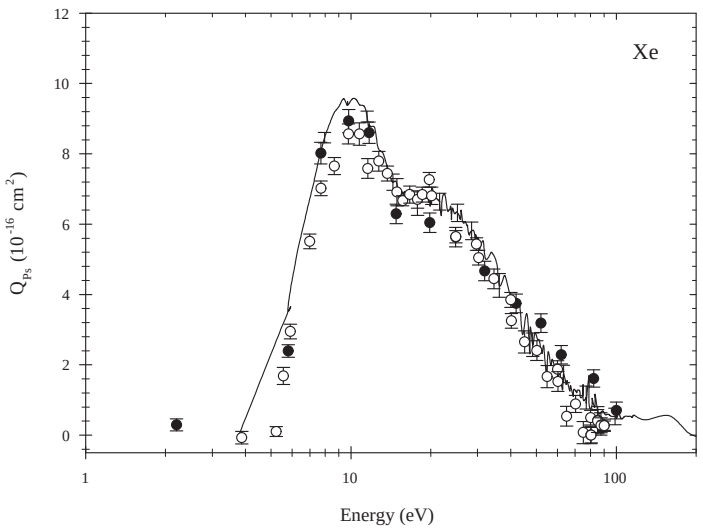

Figure 4. Determinations of Q_{Ps} for Xe: ●—present measurement, ○—[3], continuous curve—[2] (representative error bars are displayed).

comparison with previous determinations, the present Q_{Ps} displays fair agreement in the position and magnitude of the peak with the lower limit measurement of [22]. The present results are higher than the previous determination of [21] except in the peak region.

Finally, in the case of N_2 (see figure 6) the present measurement peaks at $\sim$25 eV with a magnitude of $3.57 \pm 0.06 \times 10^{-16}$ cm^2 and extends to 350 eV. In comparison with the data of [23] there is excellent agreement in shape up to 40 eV (see inset), though the magnitude disagrees by $30 \pm 15\%$. Unlike for CO_2 [18], the separation of dissociation products from the parent ion has not been achieved for N_2. The extent to which N^+ is detected will affect the absolute scale placed on the reported results, and is the subject of ongoing investigation.

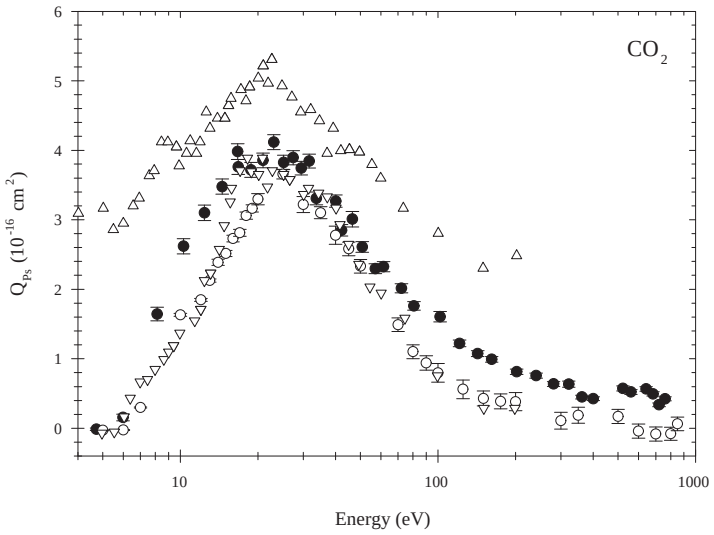

Figure 5. Q_{Ps} from CO_2: ●—present measurement, ○—[21], △ and ▽—upper and lower limits of [22], respectively.

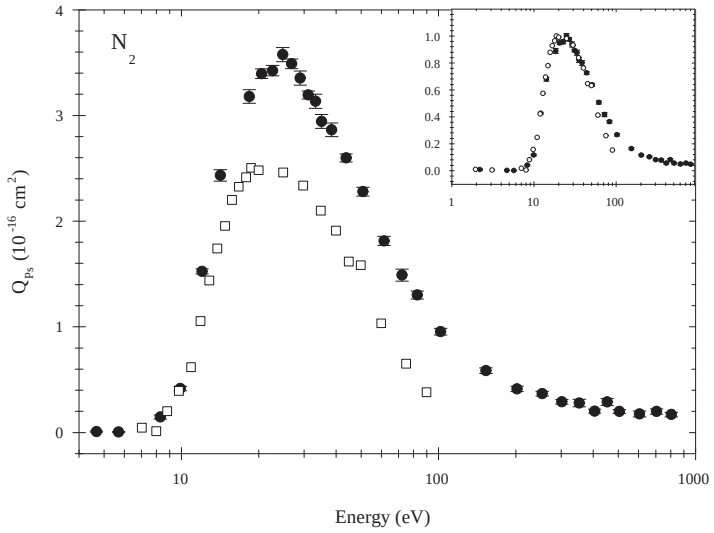

Figure 6. Q_{Ps} from N_2: ●—present measurement, □—[23]. Inset shows data normalized to each other for comparison of energy dependence (arbitrary units).

4. Conclusions

In the present work, γ-ray–ion coincidences have been used to determine Q_{Ps} for Xe, CO_2 and N_2. In the case of Xe, excellent agreement has been found between the present results and the two most recent determinations [2, 3]. For CO_2, there are a number of determinations of Q_{Ps} among which agreement is moderate. For N_2, there is an excellent agreement in shape between the present results and [23] up to 40 eV, although there is a $\sim$30% difference in magnitude. The apparent importance of Ps formation in molecules several hundred eV above threshold (in contrast to atoms) as implied by the present data is currently not understood, though it is noted that N_2 was found to be an efficient converter for positron-to-positronium beams up to $\sim$250 eV [24]. Clearly, further investigations are necessary.

5. Acknowledgements

We would like to thank J. Dumper and R. Jawad for technical assistance as well as EPSRC for funding this research.

References

[1] Van Reeth P, Laricchia G and Humberston J W 2005 *Physica Scripta* **71** C9

[2] Laricchia G, Van Reeth P, Szłuińska M and Moxom J 2002 *J. Phys. B* **35** 2525

[3] Marler J P, Sullivan J P and Surko C M 2005 *Phys. Rev. A* **71** 022701

[4] Murtagh D J, Cooke D A and Laricchia G 2009 *Phys. Rev. Lett.* **102** 133202

[5] Campbell C P, McAlinden M T, Kernoghan A A and Walters H R J 1998 *Nucl. Instr. Meth B* **143** 41

[6] Gilmore S, Blackwood J E and Walters H R J 2004 *Nucl. Instr. Meth B* **221** 129

[7] McAlinden M and Walters H 1992 *Hyperfine Interactions* **73** 65

[8] Dunlop L and Gribakin G 2006 *Nucl. Instr. Meth B* **247** 61

[9] Murtagh D J, Szłuińska M, Moxom J, Van Reeth P and Laricchia G 2005 *J. Phys. B* **38** 3857

[10] Ashley P, Moxom J and Laricchia G 1996 *Phys. Rev. Lett.* **77** 1250

[11] Moxom J, Ashley P and Laricchia G 1996 *Can. J. Phys* **74** 367

[12] Charlton M, Clark G, Griffith T C and Heyland G R 1983 *J. Phys. B* **16** L465

[13] Diana L M, Brooks D L, Coleman P G, Chaplin R L and Howell J P 1989 *Positron Annihilation* ed Dorikens-Vanpraet L, Dorikens M and Segers D (World Scientific) p 311

[14] Stein T S, Harte M, Jiang J, Kauppila W E, Kwan C K, Li H and Zhou S 1998 *Nucl. Instr. Meth B* **143** 68

[15] Szłuińska M and Laricchia G 2004 *Nucl. Instr. Meth. B* **221** 100

[16] Szłuińska M and Laricchia G 2004 *Nucl. Instr. Meth. B* **221** 107

[17] Laricchia G, Armitage S, Kövér Á and Murtagh D J 2008 *Adv. At. Mol. Opt. Phys.* vol 56 (Elsevier) pp 1–47

[18] Cooke D A, Murtagh D J, Kövér Á and Laricchia G 2008 *Nucl. Instr. Meth. B* **266** 466

[19] Szłuińska M, Van Reeth P and Laricchia G 2002 *J. Phys. B* **35** 4059

[20] Cooke D A, Murtagh D J and Laricchia G In preparation

[21] Murtagh D J, Arcidiacono C, Pešić Z D and Laricchia G 2006 *Nucl. Instr. Meth. B* **247** 92

[22] Kwan C K, Kauppila W E, Nazaran S, Przybyla D, Scahill N and Stein T S 1998 *Nucl. Instr. Meth. B* **143** 61

[23] Marler J P and Surko C M 2005 *Phys. Rev. A* **72** 062713

[24] Leslie D E, Armitage S and Laricchia G 2002 *J. Phys. B* **35** 4819

Journal of Physics: Conference Series **194** (2009) 012036 doi:10.1088/1742-6596/194/1/012036

Ionization in positron- and positronium- collisions with atoms and molecules

G. Laricchia, S. Brawley, D. A. Cooke, Á. Kövér*, D. J. Murtagh and A. I. Williams

UCL Department of Physics and Astronomy, University College London, Gower Street, London WC1E 6BT, United Kingdom

*permanent address: ATOMKI, Institute for Nuclear Research, Debrecen, Hungary

Abstract. Recent progress in the experimental study of positron- and positronium-induced ionization of atoms and molecules is outlined. Investigations include integral and differential cross-sections, as well as formation of positronium in the first excited state. Future prospects are discussed.

1. Introduction

The study of positron and positronium collisions with atoms and molecules is motivated by the need to understand basic matter–antimatter interactions, to support the development of scattering theories, to assist the analysis of astrophysical events and tests of QED bound-state problems as well as calculations of radiation damage at the molecular level for positron-emission tomography e.g. [1–3].

In this article, we review recent progress made at UCL in the measurement of cross-sections for ionization processes arising from collisions of positrons and positronium atoms with atomic and molecular targets.

2. Positron induced ionization

In collisions between a positron and an atomic/molecular target (X), ionization may proceed via a number of channels: annihilation, transfer and direct ionization. These are summarized, respectively, by reactions 1–3 below:

$$X + e^+ \longrightarrow X^{z+} + 2\gamma + (z-1)e^- \quad (1)$$

$$X + e^+ \longrightarrow X^{z+} + Ps + (z-1)e^- \quad (2)$$

$$X + e^+ \longrightarrow X^{z+} + e^+ + ze^- \quad (3)$$

where Ps and/or X^{z+} in the final state may be excited, and z corresponds to the number of electrons removed from the target. If X is a molecule, the above reactions may be accompanied by dissociation. The total ionization cross-section (Q_i^t, defined as the sum of the cross-sections for all ion producing processes) is dominated by the cross-sections for Ps formation (Q_{Ps}) and single direct ionization (Q_i^+) (reactions 2 and 3 with $z = 1$) above their respective thresholds, E_{Ps}^{thr} and E_i^{thr}. Being an exothermic reaction, annihilation is the only possible ionization channel below E_{Ps}^{thr}. It is considered generally negligible except at very low energies [4], although enhancements in the annihilation probability have been observed below E_{Ps}^{thr} near vibrational excitation thresholds and associated with the formation of vibrational Feshbach resonances [3].

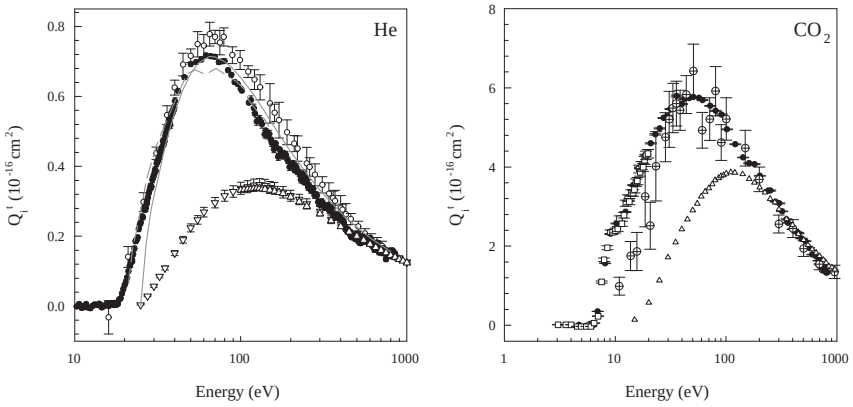

Figure 1. Theoretical and experimental determination of $Q_i^t(e^+)$: **Left:** He ●—[5], ○—[6], grey dashed curve—[7], solid grey curve—[8]. Corresponding results for e^- impact, $Q_i^t(e^-)$, shown for comparison: △—[9], ▽—[10]; **Right:** CO_2, ●—[11], □—[12], ⊕—[13], △—$Q_i^t(e^-)$ [14].

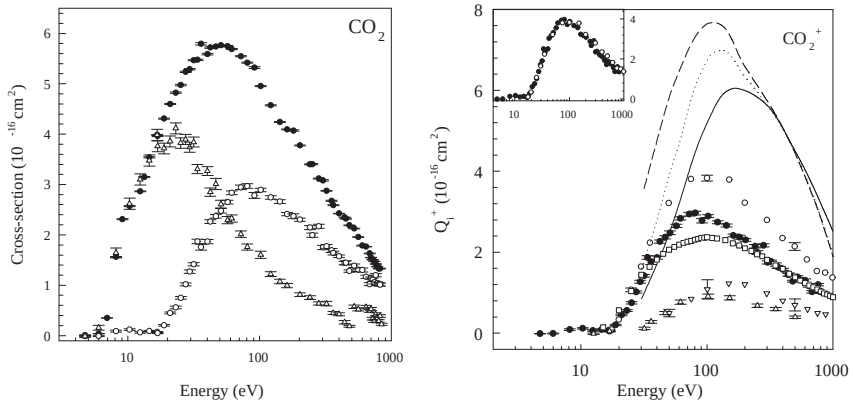

Figure 2. Left: Partitioning of Q_i^t for CO_2 [11, 15] into Q_{Ps}—△and Q_i^+—○. **Right:** Q_i^+ for CO_2 compared with theory and experiment. ●—[11], ○—[13], □—[14], ▽—$Q_i^{\rm diss}$ [13], △—$Q_i^{\rm diss}$ [15], all curves—[16]. **Inset:** normalized [15] and [13] to illustrate identical energy dependence.

Results of $Q_i^t(e^+)$ for He and CO_2 are shown in figure 1 where some discrepancies may be noted among experiments. However in He, there is excellent agreement between the data of [5] and the coupled-pseudostate calculation of [7], the maximum being better described by the results of [8]. In CO_2, there is excellent agreement in shape between the high-resolution measurements of [12] and the absolute determination of [11], the latter also agreeing in magnitude at higher energies with the earlier data of [13]. $Q_i^t(e^+)$ may be seen to exceed corresponding results for electron-impact $Q_i^t(e^-)$ at low and intermediate energies primarily due to Ps formation, as illustrated for CO_2 in figure 2 (LHS). Whilst for He (and indeed all the noble gases) Q_{Ps} tends to zero around 100–150 eV, positronium formation in CO_2 remains a significant channel at much higher energies [11].

Concerning direct ionization, as discussed in [2], there is good accord for He among experimental determinations e.g. [5, 17, 18] and with theories [7, 19–22], however the energy region within 1 eV of the threshold remains a major experimental challenge. In the case of CO_2, as shown in figure 2 (RHS), there is excellent shape agreement over the whole energy range between experimental results [13, 15], the

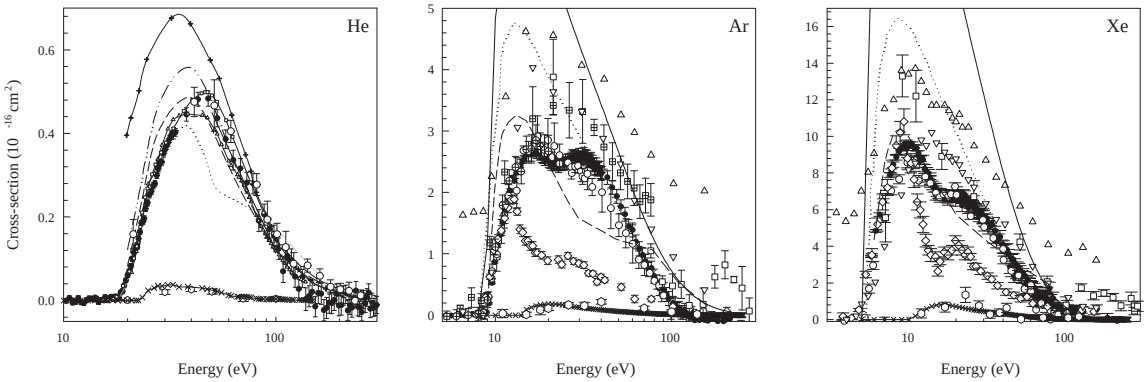

Figure 3. Left: Q_{Ps} for He, ●—[5], ○—[23], dotted black curve—[24], curve with △—[25], black chain curve—[7], solid black curve (from 50 eV)—[26], curve with + —[27], black double chain curve—[28], curve with □—[29], curve with ×—$Q_{Ps}(2P)$ [7], △—$Q_{Ps}(2P)$ [30]. **Centre:** Q_{Ps} for Ar, ●—[31], ○—[32], ◇—[33], ⊕—[34], □— [35], ⊞—[36], ▽—[37] LL, △—[37] UL, solid black curve—[38], dashed black curve—[39], dotted black curve—[40], curve with ×—$Q_{Ps}(2P)$ [38], ⬡—$Q_{Ps}(2P)$ [30]. **Right:** Q_{Ps} for Xe (symbols as for Ar).

discrepancy being entirely attributable to the electron data chosen for normalization (as illustrated in the inset) whilst the distorted-wave-Born-approximation (DWBA) results of [16] exceed experimental data by a factor of 2–3. At its maximum, the cross-section for dissociative direct ionization ($Q_i^{\rm diss}$) accounts for approximately 20% of $Q_i^t(e^+)$ for CO_2 [15].

Convergence has considerably improved in recent measurements of Q_{Ps} for the inert atoms [2], as illustrated in figure 3 for He, Ar and Xe. Whilst in helium, there is also good agreement between experimental and theoretical determinations, the situation for more complex targets is less satisfactory. Differences remain among experiments concerning structure around the peak and even greater discrepancies exist between experiment and theory, the latter overestimating measurements by a factor 2–3, although [40] and [41] found that inclusion of higher order processes leads to a significant reduction of the cross-section magnitude. Both the existence and the significance of the structure apparent in some of the experiments has been the subject of some speculation. Ps formation from higher thresholds has been considered either via capture of an inner-shell (*ns*) electron or Ps formation in an excited state (Ps*). An analysis based on an empirical scaling for ionization cross-sections [42] predicted increasing contributions of Ps* with decreasing ionization energy, I [31]. A DWBA method [38] found *ns* contributions to be very minor whilst Ps* gave rise to structure similar to that observed experimentally. Cross-sections for formation of Ps into the 2P state ($Q_{Ps}(2P)$) have now been measured [30]. The results are included in figure 3 where they are compared with corresponding theories. In He, the best agreement is with the coupled-pseudostate calculation [7]. In Ar and Xe, whilst the DWBA overestimates Q_{Ps}(all n) by factor 2–3, its predictions agree fairly well for 2P states. Interestingly, $Q_{Ps}(2P)$ is found to make a significant contribution to Q_{Ps}(all n) which increases from 6% in He to 23% in Xe.

Differential investigations of ionization by positron projectiles are scant. Triple differential studies have been carried out at UCL around 0° by measuring coincidence between scattered e^+ and ionized e^-. At 100 eV incident positron energy, a small peak was observed in the spectrum of the electrons ejected from the H_2 target at half-the-residual energy, E_r [47], a signature of the electron-capture to the continuum (ECC) phenomenon predicted ten years earlier [48]. Instead at 50 eV, an asymmetry between the energy spectra of electrons and positrons was found [49]. As shown in the LHS of figure 4, the electron spectrum was shifted by around 1.6 eV with respect to quantum theoretical expectations [44] whilst being in good agreement with classical-trajectory-Monte -Carlo calculations [45]. This latter

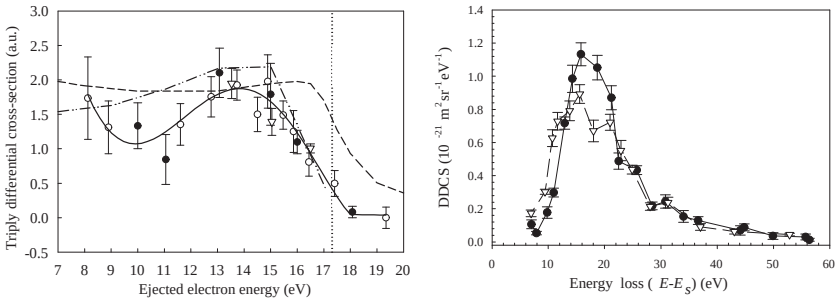

Figure 4. Left: Experimental and theoretical results for triply differential cross-sections for ejected electrons in 50 eV positron collision with H_2, D_2 and He: ●—D_2, ○—H_2, ▽—He at same E_r [43], solid curve—fit to experimental data as a guide to the eye; dashed curve—[44], double chain curve—[45], dotted line—$E_r/2$. **Right:** Double differential cross-section as a function of the energy loss of the scattered e^+ projectile in coincidence with H_2O^+ fragments: ●—100 eV [46], ▽—153 eV [46].

approach, however, failed to describe the 100 eV data [47]. All these findings are the subject of current theoretical scrutiny (e.g. [50]). More recently, investigations have been extended to H_2O because of its universal importance and in order to probe whether its strong dipole moment, responsible for strong forward-scattering of electron projectiles [51], might result in the ECC cusp becoming conspicuous at the doubly differential level as is the case by ion impact [52]. The energy distributions of e^+ scattered around 0° from H_2O were measured in coincidence with the remnant ions (H_2O^+, OH^+ and H^+) at 100 and 153 eV incident energy [46]. The maxima of the double differential cross-ections (DDCS) associated with the production of OH^+ and H^+ were found to be about 5–10 times smaller than that for H_2O^+ and the shape was observed to be similar to non-polar targets. As shown in the RHS of figure 4, at both incident energies, a small shoulder in the energy loss spectra associated with H_2O^+ production was seen around 28 eV. This feature appears consistent with e^- momentum spectroscopy results [53] which identifies it with the onset of a weak shake-up band at 27.1 eV connected with the $2a_1$ orbital. Further investigations would be justified.

3. Positronium induced ionization

A positronium atom makes an interesting projectile as it has no nucleus, its constituents having the same mass and opposite charge [e.g. 2]. Since both target and projectile have structure, ionization may be accompanied by excitations of either or both colliding partners, namely: projectile fragmentation, Ps^- formation, target ionization, projectile fragmentation with target excitation, target ionization with projectile excitation and, finally, projectile fragmentation with target ionization, as summarised in reactions 4–9 below:

$$A + Ps \rightarrow A + e^+ + e^- \quad (4)$$

$$A + Ps \rightarrow A^+ + Ps^- \quad (5)$$

$$A + Ps \rightarrow A^+ + e^- + Ps \quad (6)$$

$$A + Ps \rightarrow A^* + e^+ + e^- \quad (7)$$

$$A + Ps \rightarrow A^+ + e^- + Ps^* \quad (8)$$

$$A + Ps \rightarrow A^+ + 2e^- + e^+ \quad (9)$$

Reaction 4 is the only one not involving a change in the internal energy of the target and is referred to as target-elastic (TE); all the others are said to be target-inelastic (TI). Experimentally, these have been

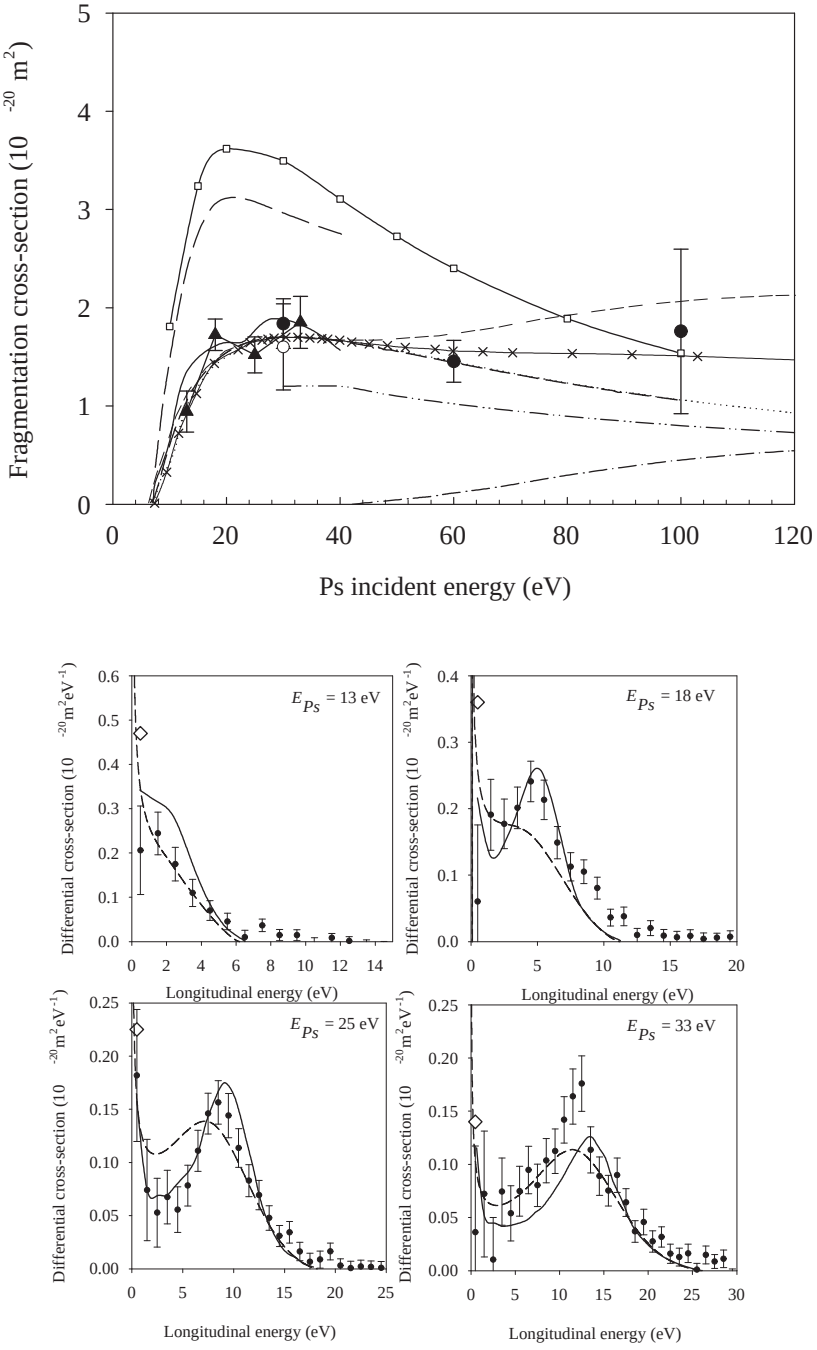

Figure 5. Top: The fragmentation cross-sections for Ps impact on He. ▲—Q_f^+ [54], ●—Q_f^+ [55], ○—Q_f^- [55], curve with □—TE [56], long dashed curve—TE [57], solid curve—TE [58], double chain curve—TE [59], medium dashed curve—TE [60], curve with ×—TE+TI Q_f^+ [61], short dashed curve—TE+TI Q_f^- [62]. **Bottom:** The absolute single differential cross-section dQ_f^+/dE_ℓ for the fragmentation of Ps in collision with He atoms. In this figure, longitudinal energy refers to that of the ejected positron and E_{Ps} to the incident energy of the Ps projectile. ●—[54], solid curve—[57] $\times 0.5$, dashed curve—[60], ◇—Average value < 1 eV [60].

investigated by detecting the positron or the electron in the final state: the total Ps fragmentation cross-section Q_f^+ (corresponding to the sum of the cross-sections for all processes involving the break-up of Ps) is measured when detecting positrons; the total fragmentation cross-section Q_f^- (corresponding to the sum of the cross-sections for all target and projectile ionization channels) is determined when detecting electrons. The differential cross-section with respect to the (longitudinal) energy of the ejected positron (dQ_f^+/dE_ℓ) has also been determined by a time-of-flight method [54] and by retarding field analysis [55, 63].

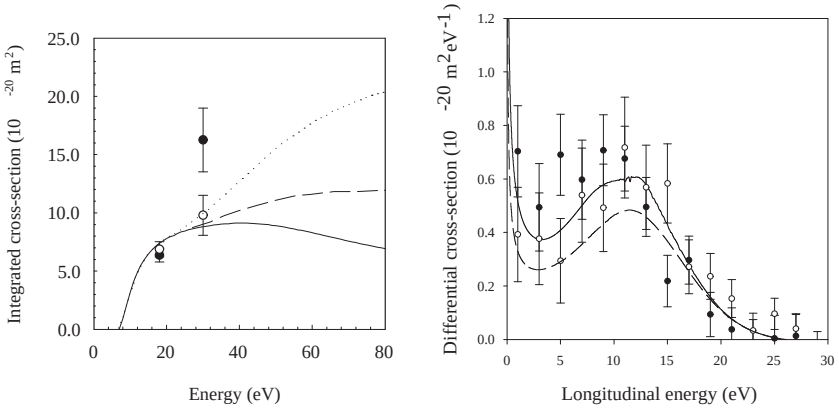

Figure 6. Left: The fragmentation cross-section for Ps impact on Xe. ●—Q_f^+ [63], ○—Q_f^- [63], solid curve—TE [61], dashed curve—TE+TI Q_f^+ [62], dotted curve—TE+TI Q_f^- [62]. **Right:** Longitudinal energy distributions of the ejected positrons form Ps collisions with Xe at 30 eV. ●—[63], solid line—[61]; ○—corresponding He data ×4 [54], dashed line— He×4 [60].

The results for He are shown in figure 5. In the top figure, both Q_f^+ and Q_f^- may be seen to agree with a coupled-pseudostate calculation [58] and an impulse approximation [60] supplemented by a first Born calculation for target inelastic processes [62]. The dQ_f^+/dE_ℓ shown in the bottom figure display a peak which grows in significance with positronium incident energy and arises from the occurrence of electron-loss to the continuum (a phenomenon related to ECC) where, following Ps break-up, the electron and the positron in the final state move with a small relative velocity. The agreement in shape with the results of the classical-trajectory Monte Carlo calculation [57] is very good and that with the impulse approximation [60] is good both in shape and absolute magnitude.

In figure 6, corresponding results for xenon are displayed. On the left, Q_f^- may be seen to exceed Q_f^+ at 30 eV, implying a degree of target ionization, contrary to theoretical expectations. On the right, the experimental dQ_f^+/dE_ℓ results for Xe [63] are compared with theory [61] with which they are in broad accord. Also included in the figure are the corresponding experimental results for He multiplied by a factor of 4 for shape comparison: the distributions for the two targets appears very similar, except perhaps at the lowest energy.

4. Conclusions and outlook

Recent progress in the study of ionization induced by positron and positronium impact on atoms and molecules has been presented. Results now comprise both integral and differential cross-sections, with and without Ps formation in the case of positron impact, and with and without target ionization for positronium projectiles. Whilst exploration of molecular targets is comparatively less advanced, investigations are now progressing to photon–ion coincidences to probe reactions where the target ion

is left in an excited state [11]. The pace is expected to quicken further with the realization of positron reaction microscopes which are currently under development [e.g 64].

5. Acknowledgments

We wish to thank John Dumper and Rafid Jawad for expert technical support and express our gratitude to the Engineering and Physical Science Research Council UK (Grant no. GR/S16041/01, EP/E053521/1), the Hungarian Scientific Research Foundation (NKTH-OTKA, Grant No. 67719, OTKA K73703), the European Union (HPRN-CT-2002-00179 EPIC) and COST-STSM-P9-02555 for funding this research.

References

[1] Gribakin G and Walters H R J (eds) 2008 *Proceedings of the XIV International Workshop on Low Energy Positron and Positronium Physics* vol 266 (Nucl. Inst. Meth. B)

[2] Laricchia G, Armitage S, Kövér Á and Murtagh D J 2008 *Adv. At. Mol. Opt. Phys.* vol 56 (Elsevier) pp 1–47

[3] Surko C M, Gribakin G F and Buckman S J 2005 *J. Phys. B* **38** R57

[4] Van Reeth P, Laricchia G and Humberston J W 2005 *Physica Scripta* **71** C9

[5] Murtagh D J, Szłuińska M, Moxom J, P Van Reeth and Laricchia G 2005 *J. Phys. B* **38** 3857

[6] Fromme D, Kruse G, Raith W and Sinapius G 1986 *Phys. Rev. Lett.* **57** 3031

[7] Campbell C P, T McAlinden M, Kernoghan A A and Walters H R J 1998 *Nucl. Instr. Meth. B* **143** 41

[8] Wu H, Bray I, Fursa D V and Stelbovics A T 2004 *J. Phys. B* **37** 1165

[9] Sorokin A A, Beigman I L, Bobashev S V, Richter M and Vainshtein L A 2004 *J. Phys. B* **37** 3215

[10] Rejoub R, Lindsay B G and Stebbings R F 2002 *Phys. Rev. A* **65** 042713

[11] Cooke D A, Murtagh D J and Laricchia G 2009 *In preparation*

[12] Laricchia G and Moxom J 1993 *Phys. Lett. A* **174** 255

[13] Bluhme H, Frandsen N P, Jacobsen F M, Knudsen H, Merrison J P, Mitchell R, Paludan K and Poulsen M R 1999 *J. Phys. B* **32** 5825

[14] Straub H C, Lindsay B G, Smith K A and Stebbings R F 1996 *J. Chem. Phys.* **105** 4015

[15] Cooke D A, Murtagh D J, Kövér Á and Laricchia G 2008 *Nucl. Instr. Meth. B* **266** 466

[16] Tóth I, Campeanu R I, Chiş V and Nagy L 2006 *Phys. Lett. A* **360** 131

[17] Moxom J, Ashley P and Laricchia G 1996 *Can. J. Phys* **74** 367

[18] Ashley P, Moxom J and Laricchia G 1996 *Phys. Rev. Lett.* **77** 1250

[19] Campeanu R I, McEachran R P and Stauffer A D 1996 *Can. J. Phys* **74** 544

[20] Ihra W, Macek J H, Mota-Furtado F and O'Mahony P F 1997 *Phys. Rev. Lett.* **78** 4027

[21] Deb N C and Crothers D S F 2002 *J. Phys. B* **35** L85

[22] Kuo T Y, Sun H L and Huang K N 2003 *Phys. Rev. A* **67** 012705

[23] Overton N, Mills R J and Coleman P G 1993 *J. Phys. B* **26** 3951

[24] Hewitt R N, Noble C J and Bransden B H 1992 *J. Phys. B* **25** 557

[25] Sarkar N K, Basu M and Ghosh A S 1992 *Phys. Rev. A* **45** 6887

[26] Igarashi A and Toshima N 1992 *Phys. Lett. A* **164** 70

[27] Schultz D R and Olson R E 1988 *Phys. Rev. A* **38** 1866

[28] Mandal P, Guha S and Sil N C 1980 *Phys. Rev. A* **22** 2623

[29] Cheng Y and Zhou Y 2007 *Phys. Rev. A* **76** 012704

[30] Murtagh D J, Cooke D A and Laricchia G 2009 *Phys. Rev. Lett.* **102** 133202
[31] Laricchia G, Van Reeth P, Szłuińska M and Moxom J 2002 *J. Phys. B* **35** 2525
[32] Marler J P and Surko C M 2005 *Phys. Rev. A* **72** 062713
[33] Charlton M, Clark G, Griffith T C and Heyland G R 1983 *J. Phys. B* **16** L465
[34] Jin B, Miyamoto S, Sueoka O and Hamada A 1994 *At. Coll. Res. Jap.* **20** 9
[35] Fornari L S, Diana L M and Coleman P G 1983 *Phys. Rev. Lett.* **51** 2276
[36] Diana L M, Coleman P G, Brooks D L, Pendleton P K, Norman D M, Seay B E and Sharma S C 1986 *Positron (Electron) - Gas Scattering* ed Kauppila W E, Stein T S and Wadehra J M (World Scientific)
[37] Stein T S, Harte M, Jiang J, Kauppila W E, Kwan C K, Li H and Zhou S 1998 *Nucl. Instr. Meth. B* **143** 68
[38] Gilmore S, Blackwood J E and Walters H J R 2004 *Nucl. Instr. Meth. B* **221** 129
[39] McAlinden M and Walters H 1992 *Hyperfine Interactions* **73** 65
[40] Dunlop L J M and Gribakin G F 2006 *Nucl. Instr. Meth. B* **247** 61
[41] Macri P and Barrachina R 2009 *Nucl. Instr. Meth. B* **267** 366
[42] Szłuińska M, P Van Reeth and Laricchia G 2002 *J. Phys. B* **35** 4059
[43] Kövér Á, Paludan K and Laricchia G 2001 *J. Phys. B* **34** L219
[44] Fiol J, Rodriguez V D and Barrachina R O 2001 *J. Phys. B* **34** 933
[45] Fiol J and Olson R E 2002 *J. Phys. B* **35** 1173
[46] Arcidiacono C, Beale J, Pešić Z D, Kövér Á and Laricchia G 2009 *J. Phys. B* **42** 065205
[47] Kövér Á and Laricchia G 1998 *Phys. Rev. Lett.* **80** 5309
[48] Brauner M and Briggs J S 1986 *J. Phys. B* **19** L325
[49] Arcidiacono C, Kövér Á and Laricchia G 2005 *Phys. Rev. Lett.* **95** 223202
[50] Fiol J, Macri P and Barrachina R O 2009 *Nucl. Instr. Meth. B* **267** 211
[51] Kimura M, Sueoka O, Hamada A and Itikawa Y 2007 *Adv. Chem. Phys.* ed Prigogine S A R I pp 537–622
[52] Rudd M E, Goffe T V, DuBois R D and Toburen L H 1985 *Phys. Rev. A.* **31** 492
[53] Ning C, Hajgat B, Huang Y, Zhang S, Liu K, Luo Z, Knippenberg S, Deng J and Deleuze M 2008 *Chem. Phys.* **343** 19
[54] Armitage S, Leslie D E, Garner A J and Laricchia G 2002 *Phys. Rev. Lett.* **89** 173402
[55] Armitage S, Leslie D, Beale J and Laricchia G 2006 *Nucl. Instr. Meth. B* **247** 98
[56] Biswas P K and Adhikari S K 1999 *Phys. Rev. A* **59** 363
[57] Sarkadi L 2003 *Phys. Rev. A* **68** 032706
[58] Blackwood J E, Campbell C P, McAlinden M T and Walters H R J 1999 *Phys. Rev. A* **60** 4454
[59] Ray H 2002 *J. Phys. B* **35** 3365
[60] Starrett C, McAlinden M T and Walters H R J 2005 *Phys. Rev. A* **72** 012508
[61] Walters H, Starrett C and McAlinden M T 2006 *Nucl. Instr. Meth. B* **247** 111
[62] Starrett C, McAlinden M T and Walters H R J 2008 *Phys. Rev. A* **77** 042505
[63] Brawley S, Beale J, Armitage S, Leslie D E, Kövér Á and Laricchia G 2008 *Nucl. Instr. Meth. B* **266** 497
[64] Williams A I, Kövér Á, Murtagh D J and Laricchia G 2009 *Journal of Physics: Conference Series* in press

Available online at www.sciencedirect.com
ScienceDirect
Nuclear Instruments and Methods in Physics Research B 266 (2008) 466–470
NIM B
Beam Interactions with Materials & Atoms
www.elsevier.com/locate/nimb

Direct non-dissociative and dissociative ionization of CO_2 by positron impact

D.A. Cooke [a], D.J. Murtagh [a], À. Kövér [b], G. Laricchia [a,*]

[a] Department of Physics and Astronomy, University College London, Gower Street, London WC1E 6BT, United Kingdom
[b] Institute of Nuclear Research of Hungarian Academy of Sciences (ATOMKI), Debrecen, P.O. Box 51, H-4001, Hungary

Available online 15 December 2007

Abstract

Detailed measurements of the cross-section for non-dissociative ionization of CO_2 are presented and compared with available experimental and theoretical results. An excellent agreement is found with the energy dependence of another experimental determination; however, uncertainties exist over the magnitude. Also presented are the preliminary results for the combined cross-section for direct dissociative ionization of CO_2 into O^+ or C^+.

PACS: 34.80.Uv

Keywords: Positron; Ionization; Carbon dioxide; Dissociative; Non-dissociative

1. Introduction

Ionization of atoms by positron impact is dominated by three processes: direct single ionization, positronium formation and annihilation. These can be represented by the following reactions, respectively:

$$e^+ + A \rightarrow A^+ + e^+ + e^-, \quad (1)$$

$$e^+ + A \rightarrow A^+ + Ps, \quad (2)$$

$$e^+ + A \rightarrow A^+ + 2\gamma. \quad (3)$$

To a good approximation, the total ionization cross-section (Q_i^t) of a target may be considered to be the sum of the cross-sections for the first two of these processes (Q_i^+ and Q_{Ps}), that is, we can usually neglect the relatively minor contribution from annihilation [1] and higher order processes (e.g. double ionization). In molecules, the situation is complicated by the possibility of dissociation of the molecule itself.

Several measurements of Q_i^t, Q_i^+ and Q_{Ps} from various simple diatomic molecules (e.g. H_2 [2–4] and references therein; N_2 [5,6]; CO [7] and O_2 [5,8]) have been performed. To a lesser extent, measurements have been performed also on triatomic (e.g. CO_2 [9,7,10]; H_2O [10]) and some polyatomic molecules (e.g. CH_4 [7] and larger organic molecules [11]).

In this work, we present new results for $Q_i^+(CO_2^+)$ and compare with other available data, both experimental and theoretical. Additionally, preliminary results for the combined dissociative ionization cross-sections ($Q_i^+(O^+)+Q_i^+(C^+)$), representing the sum of the cross-sections for dissociation into O^+ or C^+ are presented.

2. Experimental setup

The experimental setup specific to these measurements is outlined briefly below, including a short description of the main system. This is described in more detail in [12]. Briefly, a beam of approximately 10^4 slow positrons s^{-1} is generated by moderating the fast β^+ output of a ^{22}Na radioactive source with an annealed tungsten mesh moderator. A potential V_m is applied to the moderator, which

* Corresponding author. Tel.: +44 207 679 3470.
E-mail address: g.laricchia@ucl.ac.uk (G. Laricchia).

0168-583X/$ - see front matter © 2007 Elsevier B.V. All rights reserved.
doi:10.1016/j.nimb.2007.12.026

defines the energy of the positron beam via $E_+ = eV_m + 2eV$. The beam is constrained radially by a magnetic field of $\sim 10^{-2}$ T produced by a series of coils and a solenoid. The transmission of unwanted components of the beam, such as fast particles, is substantially reduced by a bend in the solenoid and a Wien filter. Inside the solenoid is a cylinder held at −500 V to repel secondary electrons, and an additional cylinder, which can be biased to 5 V above V_m to measure the contribution from residual fast particles. After passing through the interaction region, the beam reaches the positron detector, a channel electron multiplier (CEM). This also has an electron repelling cylinder before it, biased at −500 V to prevent electrons produced by positron impact on the CEM from entering the gas cell and causing spurious ions. The interaction region consists of a hemispherical gas cell and a second chamber containing another CEM for detecting ions. These are perpendicularly extracted from the cell to the beam axis by the electric field from an electrostatic lens held at −500 V. Positrons, which scatter at backward angles after ionizing the target, are not detected at present. However, the importance of these events is expected to increase with increasing Z and good agreement has been found between Q_i^+ for Ar measured with the present system and available data in the literature [4].

Pulses from the ion detector are counted on a multichannel scaler and, in coincidence with pulses from the positron detector, on a multichannel analyzer, generating a time-of-flight (TOF) spectrum for the ions from which a coincidence yield can be obtained for each ionic species (see Fig. 1). Although the TOF resolution of the system is poor in comparison to that obtained with parallel plate extraction (e.g. [13,14]), the extraction efficiency (ϵ_{ext}) is high (∼50%) and the interaction region is long (∼9 cm). Within the present resolution, we cannot separate the C^+ from O^+, hence the cross-sections for the production of these two fragments are presented in a combined manner. At present it is not possible to clearly separate the CO^+ fragment from the surrounding peaks, so the cross-section for dissociation into this fragment is not presented.

The coincidence yield, Y_c^t, is proportional to the direct ionization cross-section Q_i^+ according to

$$Q_i^+ = CY_c^t = C\frac{N_c^{on} - N_c^{off}}{N_{e^+}^{on} - N_{e^+}^{off}}, \quad (4)$$

where N_c is the number of coincidences per second (with the slow positron beam biased on and off, as labelled), N_{e^+} is the incident positron beam intensity (also measured with the beam on and off), and C is a normalization constant.

The normalization constant is calculated from a quadratic fit (f_{e^-}) to the electron non-dissociative direct ionization cross-section ($Q_i^-(CO_2^+)$) data [15] above 500 eV such that $Q_i^+(CO_2^+) = Cf_{e^-}(E)$. This procedure assumes that at these energies the Born approximation applies and that positronium formation is negligible. More details of the normalization procedure may be found in [16,10]. The

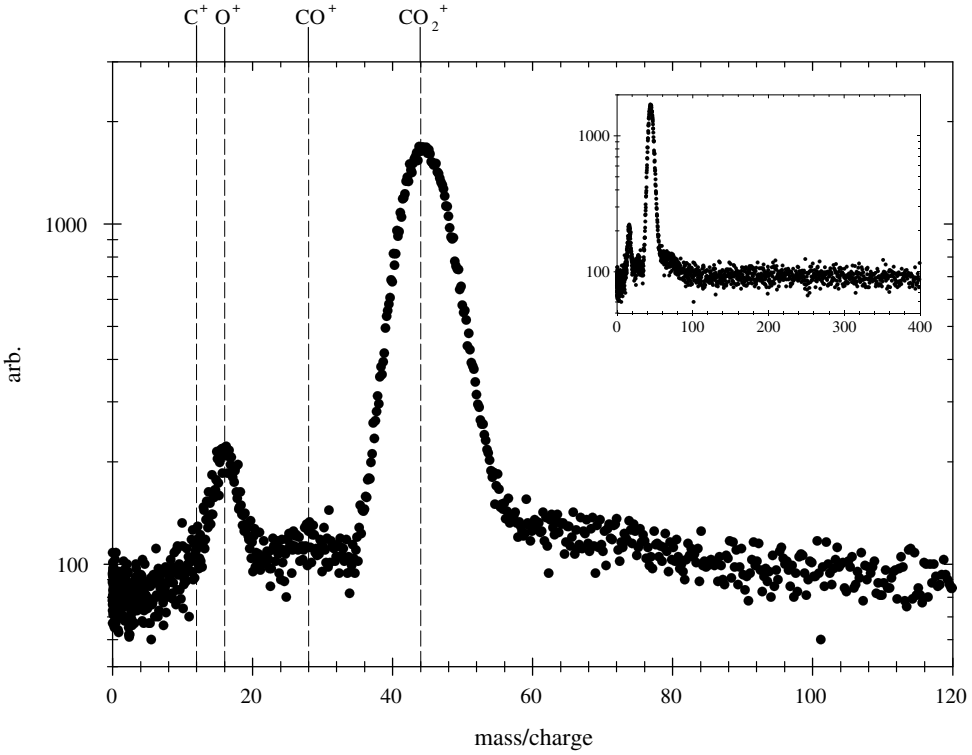

Fig. 1. Typical time-of-flight spectrum: the dashed lines indicate the expected positions for CO_2^+, O^+, C^+ and CO^+. Inset: the same spectrum over a larger range to show the background level.

dissociative ionization has been normalized using the same constant, with corrections applied for the differing extraction and detection efficiencies for each of the fragments. The relative detection efficiency $\epsilon_d^{CO_2^+}/\epsilon_d^{C^+,O^+}$ has been estimated from [17] to be 1.5 ± 0.2, at a kinetic energy of 3.4 keV (determined by the CEM cone potential). At this energy, $\epsilon_d^{C^+}$ and $\epsilon_d^{O^+}$ merge onto a single curve when plotted against $E/M^{0.5}$ (where M is the mass of the ionic fragment). The following method was used to calculate ϵ_{ext} for the fragments. The ion optics of the gas cell were simulated using SIMION and the ϵ_{ext} for each ionic species at a variety of energies was obtained. This distribution, depending only on the kinetic energy of the ions, was convoluted with the kinetic energy distributions of the various fragments [18] and integrated over the full energy range of the ejected fragments. The ratio of ϵ_{ext} to that for CO_2^+ (whose kinetic energy distribution is assumed to be thermal) yielded corrections for O^+ and C^+ of 1.92 and 1.61, respectively. To calculate a correction for the combined cross-section, the average of these two values was used. This was done as the relative yields of O^+ and C^+ are unknown. However, we note that if these are taken from [7], then the correction would differ only by ~3%.

3. Results and discussion

Fig. 2 shows the present measurement of $Q_i^+(CO_2^+)$ compared with other available positron data [7] and the electron data ($Q_i^-(CO_2^+)$) [15] to which they are normalized. The present results peak around 80 eV at a value of 2.9×10^{-16} cm^2, approximately 30% greater than for $Q_i^-(CO_2^+)$. Both experimental measurements agree on the positions of the threshold and peak; however, disagreement in the magnitude of the cross-section exists. This may be attributed to the difference in electron data used for normalization, with [7] being normalized to $Q_i^+(CO_2^+)$ of [20], and the present measurement to [15] which is ~30% lower. The relative behaviour of $Q_i^+(CO_2^+)$ and $Q_i^-(CO_2^+)$ is consistent with the trends in the direct ionization cross-sections for particle–antiparticle pairs [21,22]. The excess around the peak of $Q_i^+(CO_2^+)$ is usually ascribed to target polarization effects, whilst the decrease of Q_i^+ below Q_i^- with decreasing energy is thought to be due to the competition from positronium formation.

The theoretical calculations of [19] are also shown in Fig. 2. The previous (CPE, Coulomb plus plane waves with full energy range) approximation has been recently improved by incorporating screening potentials for calculating the wavefunction of the ejected electron (ES, electron screening) as well as including them to calculate the wavefunction for both the incoming and the outgoing particles (TS, total screening). Significant discrepancies exist at virtually all energies between experimental data and theory. However, fair agreement in energy dependence between the present results and those from the ES model may be noted from mid- to high energy by multiplying the latter by a factor of ~0.36.

Fig. 3 shows the preliminary cross-section for dissociation into O^+ or C^+, $Q_i^+(O^+) + Q_i^+(C^+)$, compared with available data. Significant discrepancies exist between the

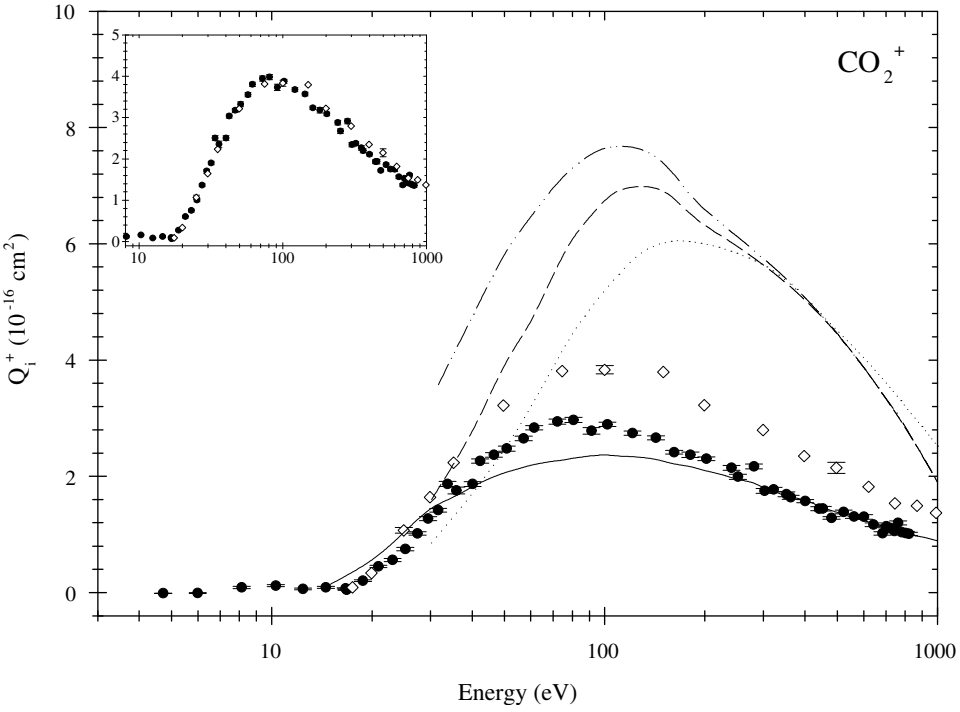

Fig. 2. Present measurements of $Q_i^+(CO_2^+)$ (●) compared with the other available data: ◇ – [7]; continuous line – [15] (e^-) and dashed/dotted lines: Coulomb plus plane wave with full energy range (CPE – dotted line), total – (dashed line) and electron screening (double-chain curve) models (TS and ES) of [19]. Inset: the present measurements renormalized to electron data of [20], demonstrating excellent agreement with [7].

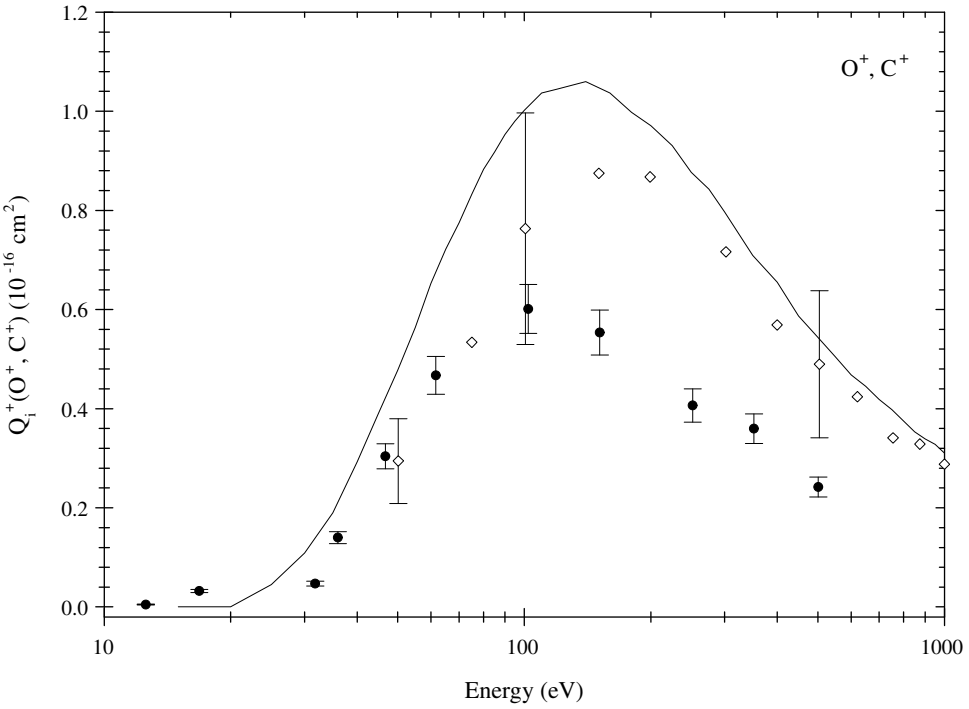

Fig. 3. Present measurements of $Q_i^+(O^+) + Q_i^+(C^+)$ (●) compared with the combined measurements of [7] (◇) and combined electron data of [15] (continuous line).

two positron data sets. Unlike with $Q_i^+(CO_2^+)$, only part of this may be attributable to the different $Q_i^-(CO_2^+)$ to which they are normalized. As also noted in [7], the positron data are lower than the corresponding electron data. Bluhme et al. [7] suggested that this might be due to dissociative ionization often resulting from ionization simultaneous to excitation of the molecule into a dissociative state. It is also noted that cross-sections for multiple and inner-shell ionization by electron impact exceed those by positron impact (e.g. [21–23]). Further work to gain understanding of the effect of charge on dissociative ionization is needed.

4. Conclusions

Measurements of $Q_i^+(CO_2^+)$ for CO_2 have been presented, demonstrating excellent agreement with the previous measurements in shape. However, uncertainty in the absolute scale remains, mainly due to discrepancies among corresponding electron data for this target. For this reason, an alternative normalization method is being developed. Furthermore, current investigations of ionization–excitation by positron impact on this target [24] might elucidate the influence of this process on dissociative ionization.

Acknowledgement

EPSRC is gratefully acknowledged for supporting this work under Grant No. GR/S16041/01 and for providing D.A. Cooke and D.J. Murtagh with research studentships.

References

[1] P. Van Reeth, G. Laricchia, J.W. Humberston, Phys. Scripta 71 (2005) C9.
[2] S. Zhou, H. Li, W.E. Kauppila, C.K. Kwan, T.S. Stein, Phys. Rev. A 55 (1997) 361.
[3] P. Ashley, J. Moxom, G. Laricchia, Phys. Rev. Lett. 77 (1996) 1250.
[4] J. Moxom, P. Ashley, G. Laricchia, Can. J. Phys. 74 (1996) 367.
[5] J.P. Marler, C.M. Surko, Phys. Rev. A 72 (2005) 06273.
[6] H. Bluhme, N.P. Frandsen, F.M. Jacobsen, H. Knudsen, J. Merrison, K. Paludan, M.R. Poulsen, J. Phys. B 31 (1998) 4631.
[7] H. Bluhme, N.P. Frandsen, F.M. Jacobsen, H. Knudsen, J.P. Merrison, R. Mitchell, K. Paludan, M.R. Poulsen, J. Phys. B 32 (1999) 5825.
[8] (a) Y. Katayama, O. Sueoka, S. Mori, J. Phys. B 20 (1987) 1645; (b) G. Laricchia, J. Moxom, M. Charlton, Phys. Rev. Lett. 70 (1993) 3223.
[9] G. Laricchia, J. Moxom, Phys. Lett. A 174 (1993) 255.
[10] D.J. Murtagh, C. Arcidiacono, Z.D. Pešić, G. Laricchia, Nucl. Instr. and Meth. B 247 (2006) 92.
[11] L.D. Hulett Jr., Jun Xu, S.A. McLuckey, T.A. Lewis, D.M. Schrader, Can. J. Phys. 74 (1996) 411.
[12] M. Szłuińska, P. Van Reeth, G. Laricchia, Nucl. Instr. and Meth. B 192 (2002) 215.
[13] À. Kövér, G. Laricchia, Measur. Sci. Technol. 12 (2001) 1875.
[14] C. Arcidiacono, À. Kövér, Z.D. Pešić, J. Beale, G. Laricchia, Radiat. Phys. Chem. 76 (2007) 431.
[15] H.C. Straub, B.G. Lindsay, K.A. Smith, R.F. Stebbings, J. Chem. Phys. 105 (1996) 4015.
[16] D.J. Murtagh, M. Szłuińska, J. Moxom, P. Van Reeth, G. Laricchia, J. Phys. B 38 (2005) 3857.

[17] M. Krems, J. Zirbel, M. Thomason, R.D. DuBois, Rev. Sci. Instrum. 76 (2005) 093305.
[18] R. Velotta, P. Di Girolamo, V. Berardi, N. Spinelli, M. Armentante, J. Phys. B 27 (1994) 2051.
[19] I. Tóth, R.I. Campeanu, V. Chiş, L. Nagy, Phys. Lett. A 360 (2006) 131.
[20] O.J. Orient, S.K. Srivistava, J. Phys. B 20 (1987) 3923.
[21] K. Paludan et al., J. Phys. B 30 (1997) L581.
[22] V. Kara, K. Paludan, J. Moxom, P. Ashley, G. Laricchia, J. Phys. B 30 (1997) 3933.
[23] R. Hippler, S. Helms, U. Brinkmann, J. Deiwiks, H. Schneider, D. Segers, Ch. Dauwe, Nucl. Instr. and Meth. B 99 (1995) 12.
[24] D.A. Cooke, D.J. Murtagh, G. Laricchia, in preparation.